New Directions for Cu^{2+} Labeling of Biomolecules to Determine Structure, Conformation, and Flexibility

by

Austin Gamble Jarvi

Bachelor of Science, Geneva College, 2015

Submitted to the Graduate Faculty of the

Dietrich School of Arts and Sciences in partial fulfillment

of the requirements for the degree of

Doctor of Philosophy

University of Pittsburgh

2020

UNIVERSITY OF PITTSBURGH

DIETRICH SCHOOL OF ARTS AND SCIENCES

This dissertation was presented

by

Austin Gamble Jarvi

It was defended on

November 19, 2020

and approved by

David Waldeck, Professor, Department of Chemistry

W. Seth Horne, Professor, Department of Chemistry

Junmei Wang, Professor, Department of Pharmaceutical Sciences

Thesis Advisor: Sunil Saxena, Professor, Department of Chemistry

Copyright © by Austin Gamble Jarvi

2020

New Directions for Cu^{2+} Labeling of Biomolecules to Determine Structure, Conformation, and Flexibility

Austin Gamble Jarvi, PhD

University of Pittsburgh, 2020

In this thesis, we showcase several key applications of Cu^{2+} labeling in proteins and nucleic acids using electron paramagnetic resonance (EPR) spectroscopy. In proteins, the double histidine (dHis) motif is employed to coordinate a Cu^{2+} complex. With EPR, it is possible to measure nanoscale distances between two such sites. The dHis method produces distance measurements with a very narrow probability distribution, enabling precise structural assessment.

First, we provide optimal conditions to label a dHis motif with a Cu^{2+} complex in proteins, and a comprehensive overview of the factors that impact labeling efficiency. We show that dHis labeling is sensitive to the buffer used, and under optimal conditions, up to 80% of proteins can be doubly labeled – a substantial improvement over previous implementations. We demonstrate the power of the dHis method in the precise location of a native metal binding site within a protein. We show that the narrow distance distributions enable a high precision localization, even with very few measured constraints. Such principles can be extrapolated to protein-protein docking, quaternary structural assembly, substrate binding, and protein-DNA interactions. Additionally, we show that the dHis motif is uniquely suited to determine protein subunit orientations by performing distance measurements at high frequencies. Such orientational information is extracted from the Cu^{2+} center, and we show that the Cu^{2+} orientation is correlated to the protein subunit on which the dHis motif is applied. Finally, we take the characteristics behind the success of the dHis motif

and apply them to peptide nucleic acids (PNA) to determine precise distance constraints between two site-specific Cu^{2+} labels. Combined with molecular dynamics simulations, we gain an atomistic insight into the structure and dynamics of the PNA duplex. Such work presents an efficient, precise method that provides detailed structural information regarding the nucleic acid, and may be applied to other systems such as DNA or RNA in the future. Overall, this body of work marks a significant advancement of Cu^{2+} labeling to determine relevant structural information in proteins and nucleic acids, while presenting clear methodologies to promote the widespread adoption of this technique within the scientific community.

Table of Contents

List of Tables

List of Figures

Preface

It is an interesting thing to see the past five years of my work compiled into a few hundred pages. While the work included in this document is certainly fine science (if I say so myself), I know that this document cannot quite capture the intangibles that this degree has instilled in me. I initially approached my PhD as a means to an end – that end being gainful employment performing high-level chemistry. To an extent, it is still that, however I have come to see that it is not merely the letters after my name that will progress me after my time at Pitt, but the habits, skills, and perspectives I have acquired through this program. I have many to thank for helping me along, as I would not have acquired such a perspective (or accomplished half of what I did) without their aid.

First, thank you to my advisor, Prof. Sunil Saxena. I understand I have not always been the easiest to advise, but the mentorship and guidance he provided to me have left me confident in myself as a scientist. Certainly, the success I experienced in grad school, and the professional successes I have yet to experience are largely due to his guidance and persistence.

Thank you to my committee members, Prof. David Waldeck, Prof. W. Seth Horne, and Prof. Junmei Wang for seeing me through this process.

Thank you to my lab mates, to Tim Cunningham and Matt Lawless for their early input, training, and guidance (and patience). To Shreya Ghosh for going through all the trials and tribulations alongside me, and to Kevin Singewald, Xiaowei Bogetti, Zikri Hasanbasri, Josh Casto, and Alysia Mandato for taking the various torches that I am passing on. The lab is in good, capable hands.

And of course, thank you to my friends and family. Thank you to my mom and dad for having my back and being constantly supportive (and having the sword and top hat on standby for this day). Thank you to Erik and Evan and Kate for the encouragement throughout this time. Thank you to Rick and Janice and all my sisters-in-law for supporting me as one of their own. Thanks to the Boys for always asking how my proteins were doing and if I was ever going to graduate. Heck, thanks to my cats Pancake and Frying Pan, because this is the section where I have creative freedom and can immortalize their names here. You two were a good comfort after stressful days. And finally, thank you to my incredibly loving, supportive, and gracious wife, Gwenyth, for always being there, for picking me up when I was down, for pushing me to be the best version of myself both inside and outside of the lab, and for making that lawyer money while I finished up this stage in my career. Here's to whatever comes next.

1.0 Introduction

This work, written in collaboration with Xiaowei Bogetti, Kevin Singewald, Shreya Ghosh, and Sunil Saxena, was submitted for publication in November 2020. The thesis author prepared the manuscript.

Scientific progress is often spurred by advances in both technology and methodology. An excellent example of this relationship is found in electron paramagnetic resonance (EPR), which over the past several decades has emerged as a powerful means of assessing biomolecular conformations and dynamics. Modern EPR spectrometers benefit from high frequencies and magnetic fields,[1] specialized and highly sensitive resonators,[2] commercially accessible pulse shaping,[3] and other advances in computational power, analysis techniques, and software development.[4-6] On the other hand, much biophysical progress achieved by EPR may also be attributed to strides in methodology. Early on, continuous wave (CW) EPR and nuclear double resonance techniques furthered EPR as an important tool for biophysical measurements.[7] The development of pulsed and two dimensional EPR methodologies expanded the applications accessible to EPR.[8-11] In particular, pulsed EPR methods that can measure nanometer-scale distances between two spin labels have had an immense impact on the use of EPR in biophysical research.[11-14]

The advent of site-directed spin labeling, which enables the site-specific placement of an EPR spin label on an otherwise diamagnetic protein, has contributed to a boom in biophysical EPR, with diverse and widespread applications.[15] The most common spin label is a nitroxide based moiety that attaches to free cysteine residues in a protein, leading to a side-chain commonly

referred to as R1. This label is responsible for some of the most impactful biophysical EPR findings, from site-specific dynamics, identification of secondary structure,[16] monitoring of quaternary structure,[17-19] biomolecular interactions,[20-23] and induced conformational changes.[24-29] However, R1 experiences high rotameric flexibility caused by five rotatable bonds that attach the nitroxide head to the protein backbone. Accordingly, fluctuations in the dihedral angles contribute significantly to the distance distribution measured by EPR, which hinders the ability to interpret R1 data in terms of protein structure and conformation.[30-31] Similarly, the propensity of R1 to engage in local interactions, especially in the β-sheet, can often limit its use as a reliable assay of site-specific protein dynamics. Additionally, the reliance of R1 on cysteine attachment can introduce some limitations. Often, this scheme relies on removing all native cysteines so that the spin labeling can be performed at the desired location. Therefore, R1 labeling may be prohibitive in systems with functional or numerous cysteine residues.

Herein, we focus on Cu^{2+} labeling techniques in proteins that can provide orthogonal labeling schemes as well as avoid many of the problems commonly associated with nitroxide spin labeling. We present this chapter as a comprehensive overview of these techniques, as well as an introduction to the works that will be discussed in detail within this thesis.

1.1 Site Directed Cu^{2+}-Labeling of Proteins

1.1.1 Labeling Scheme and Protocol

In Chapter 2, we present a detailed discussion of an optimized protocol for the implementation of the double histidine (dHis) Cu^{2+} labeling scheme. We will also emphasize the impact of buffer choice on the efficiency of loading. In brief, Figure 1A shows the scheme for site-directed Cu^{2+} labeling of proteins. The method exploits two His residues, either endogenous or site-specifically mutated into the protein, to chelate a Cu^{2+} complex. These mutations are optimally created at positions i, i+4 for α-helices, and i, i+2 for β-sheets, as illustrated in Figure 1-1A.[32-34] In order to prevent nonspecific binding of the Cu^{2+} elsewhere within the protein, labeling is achieved by simple addition of a Cu^{2+}-nitrilotriacetic acid (NTA) complex.[34] A low temperature (i.e. 4^{o} C) is advisable for optimal labeling as the binding of Cu^{2+}-NTA to dHis is exothermic.[35] Remarkably, labeling is easy and can be achieved in ~30 minutes for surface accessible sites, which is an important consideration for unstable proteins.[36] Furthermore, there is no need for post-labeling protein purification. On the other hand, the buffer can compete with dHis for the binding of the Cu^{2+}-NTA complex. Recent work has shown that the labeling is facile in many buffers such as MOPS, sodium phosphate, and NEM, whereas Tris buffer degrades loading of the label onto dHis sites.[36]

Chapter 2 also elaborates on the spectroscopic methods introduced here that can be used to assay the loading efficiency. The low temperature continuous wave (CW) EPR spectrum for dHis-bound Cu^{2+} species is characterized by four hyperfine peaks, illustrated in Figure 1-1B. The shift of these peaks from free Cu^{2+}-NTA to dHis-Cu^{2+}-NTA is often a visible indicator of proper Cu^{2+}

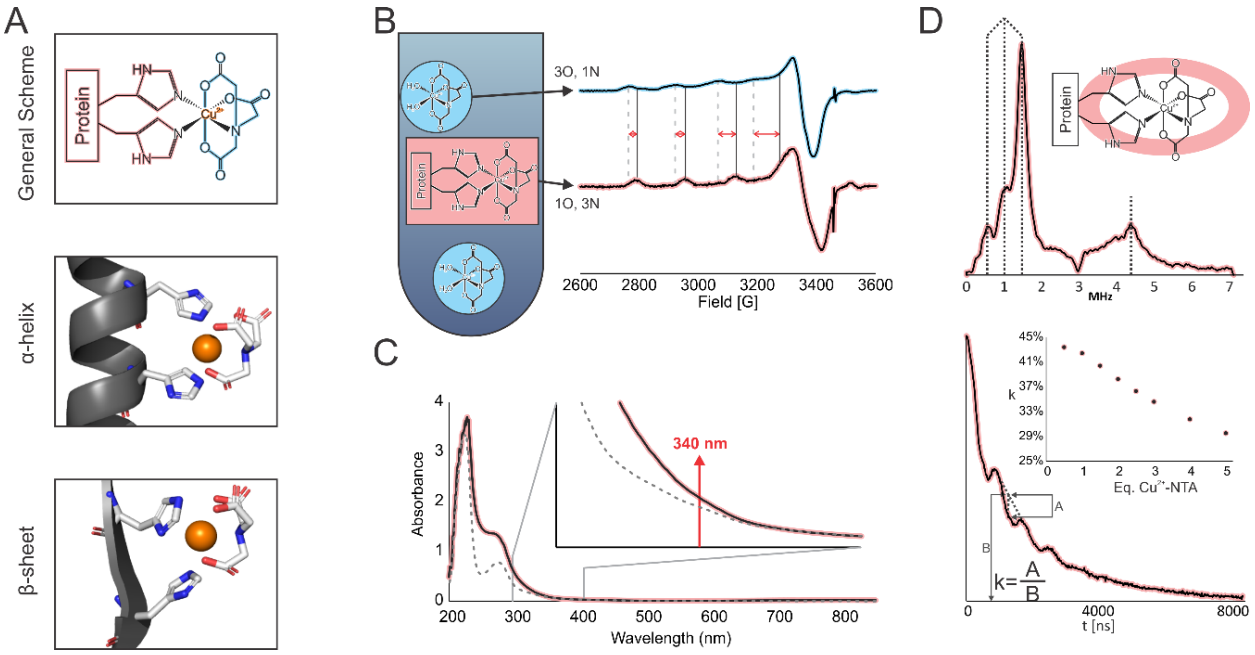

Figure 1-1 A) Chemical structure of the Cu^{2+}-NTA complex (top) Placement of the two histidines that comprise the dHis motif in an α-helix (middle) and a β-sheet (bottom). B) Chemical structures of free Cu^{2+}-NTA and dHis-bound Cu^{2+}-NTA (left) and their respective CW EPR spectra (right). The differences in spectral features are noted for easy visualization. C) UV/Vis spectra of dHis modified protein (gray dashed line) and the same protein with an excess of Cu^{2+}-NTA added (black line). D) ESEEM spectrum of dHis-Bound Cu^{2+}-NTA (top). Identifying peaks below 3 MHz and from 4-6 MHz are noted. Time domain ESEEM signal (bottom). The variation of modulation depth with varying amounts of Cu^{2+}-NTA based on a K_d=12 μM is illustrated in the inset.

coordination. The spectrum can be simulated to ascertain the component percentages and loading efficiency in samples with incomplete dHis-Cu^{2+}-NTA binding. Such data from CW EPR can be combined with double electron electron resonance (DEER) measurements to fully elucidate the amount of fully and partially loaded proteins in a sample. [33-34, 37] The coordination of the Cu^{2+}-NTA complex to a dHis site also has a recognizable UV/Vis signature in a metal to ligand charge-transfer band at 340 nm, as shown in Figure 1-1C.[38] Monitoring this transition as a function of equivalents of Cu^{2+}-NTA to dHis sites can elucidate the apparent dissociation constant, K_d, of Cu^{2+}-NTA to dHis.[36]

Finally, electron spin echo envelope modulation (ESEEM) spectroscopy provides complementary insight into the loading of Cu^{2+}-NTA to dHis.[39] The coordination of Cu^{2+} to imidazole nitrogen atoms found in histidine produces a characteristic frequency spectrum with three peaks below 3 MHz and a broad peak around 4-6 MHz, shown in Figure 1-1D (top). If necessary, the normalized integrated intensity of the ESEEM spectrum can be used to determine the number of His residues coordinated to Cu^{2+}.[40-41] Finally, the modulation depth, k, in the time domain ESEEM signal, (cf. Figure 1-1D, bottom), provides information on the relative amount of Cu^{2+}-NTA bound to dHis. [33, 40-42] In particular, the presence of free Cu^{2+}-NTA degrades the modulation depth since this species has a featureless decay under proton cancellation conditions. Figure 1-1D (bottom inset) shows this effect in a simulated titration of Cu^{2+}-NTA into a dHis site. With more equivalents of Cu^{2+}-NTA, and hence excess free Cu^{2+}-NTA, the modulation depth decreases. In practicality, a stoichiometric ratio of Cu^{2+}-NTA is typically used to maximize bound label while minimizing the amount of free label.[36]

1.2 Site Specific Protein Dynamics Measured by Cu^{2+}-Labeling

The dHis labeling scheme naturally lends itself well to several important biophysical applications. Recent work has shown that dHis-based CW EPR measurements at physiological temperature are sensitive reporters of site-specific protein dynamics within both α-helix and β-sheet sites. The bidentate nature of the Cu^{2+} binding to the proteins makes the label especially sensitive to fluctuations of the protein backbone. Accordingly, backbone motions lead to averaging of the g- and hyperfine parameters of the Cu^{2+}, which ultimately generates dramatic changes in the CW-EPR lineshapes, as illustrated in Figure 1-2. Figure 1-2 shows a simulated rigid limit spectrum (black line) of Cu^{2+}-dHis and the splittings from $A_{\|}$ are clearly highlighted. Simulated lineshapes based on the Stochastic Liouville Equation are shown in color,[43] and illustrate the dramatic changes in the spectral lineshapes at different reorientational correlation times.

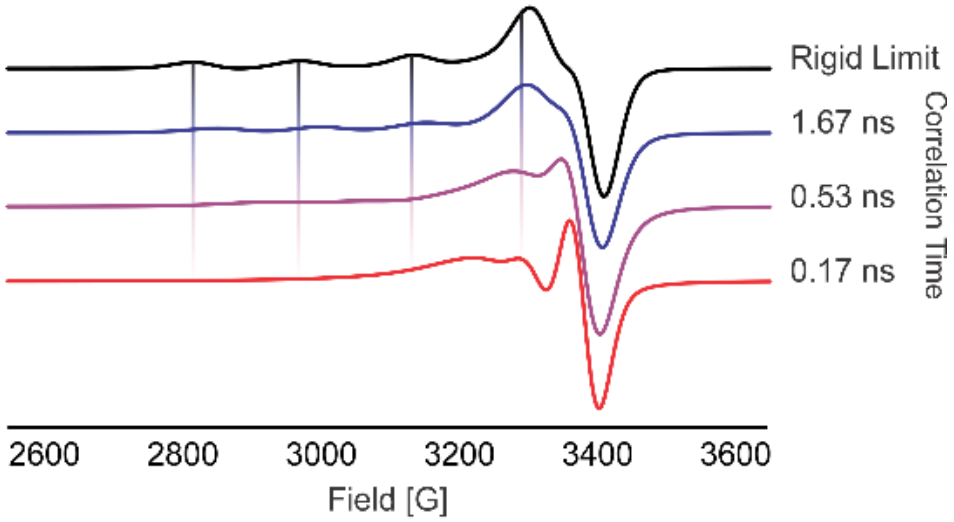

Figure 1-2 CW EPR simulations emphasizing the effect of reorientational correlation time on spectral features.

In recent work, this concept was established using three dHis mutants of the small globular protein GB1 in which the dHis site was placed on two different β-sheet locations and one α-helical location.[44] Importantly, the order parameters and reorientational correlations times were in accord with predictions from a 300 ns MD simulation as well as previous NMR findings. Furthermore, the method was applied to understand the role of helix dynamics in the function of human glutathione S-transferase A1-1 (hGSTA1-1). This protein is a detoxification enzyme that protects the cell by conjugating glutathione with a variety of xenobiotics. In this work, the dHis label was placed on the α9 helix, a subunit that is necessary for substrate recognition and catalytic function.

Despite the much larger size of hGSTA1-1 compared to GB1 (444 residues vs 56 residues) the CW EPR lineshape analysis indicated that the α9 helix fluctuates ~20 times faster than any of the GB1 sites.[44] Importantly, spectral simulations also reported two dynamical modes of the helix–one with a rotational correlation time of 68±10 ps and the other at 119±16 ps.[44] These data were significant as previous NMR studies could not quantify the dynamics of this helix in the unligated state, presumably due to exchange between the two dynamical states.[45] Additionally, in the presence of an inhibitor, the population of the less dynamic conformation increased. Together, the data provided a holistic picture of the protein function, wherein the faster dynamical mode aids in the rapid 'search' for substrates, and the helix localizes for enzymatic function upon ligand binding.[46]

1.3 Distance Measurements on Cu^{2+}-Labeled Proteins

In addition to site specific dynamics, the localization of the Cu^{2+} center within the dHis motif has dramatic ramifications for the measurement of intramolecular distances between spin labeled sites. Two such examples are detailed in Chapters 3 and 4. Figure 1-3A illustrates a protein labeled with dHis-Cu^{2+}-NTA at positions 6/8 and 28/32 (left) and labeled with R1 at positions 6 and 28 (right). The spatial distribution of the Cu^{2+} center and that of R1 were estimated using the multiscale modeling of macromolecules (MMM) program.[47] Clearly, the Cu^{2+} occupies a significantly smaller volume than the nitroxide label. The large flexibility of the nitroxide side chain leads to a broad distribution in distances. On the other hand, the bidentate dHis motif effectively 'locks' the Cu^{2+} center in place, resulting in a distribution of dHis-dHis distances that is very narrow. This effect is illustrated in Figure 1-3B. The narrow distribution of the dHis motif, with a FWHM as low as 1 Å, leads to a high distance resolution, in contrast with nitroxide labels which often produce broad distance distributions with FWHM typically greater than 5-10 Å.

To date the PDS techniques[11-12, 48-51] double electron electron resonance (DEER),[52-54] relaxation induced dipolar modulation enhancement (RIDME),[35, 55] and double quantum coherence (DQC)[56-58] have been applied to Cu^{2+}. DEER is the most commonly used of these techniques, although RIDME can offer gains in sensitivity compared to conventional DEER in cases.[35, 55] Background subtracted time domain signals representative of DEER are shown in the inset of Figure 3B.

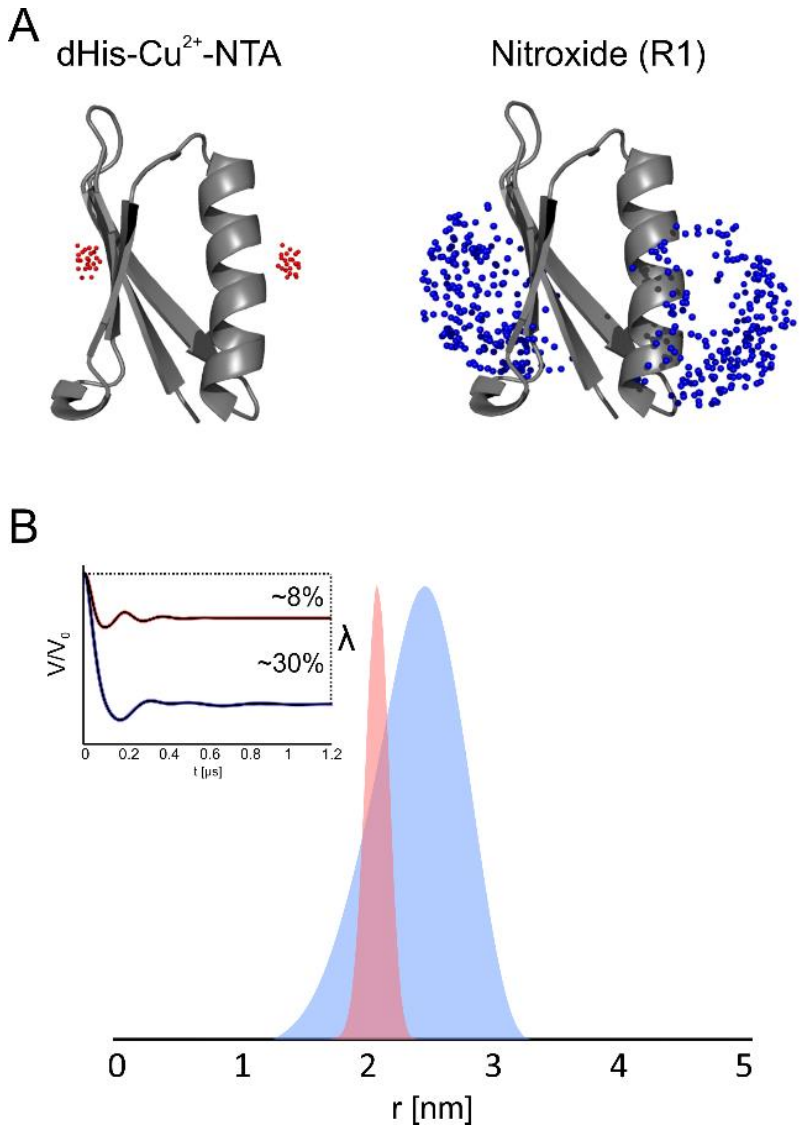

Figure 1-3 A) A double-dHis modified protein (left) and a double-R1 labeled protein (right). The spatial distribution of the Cu^{2+} and Nitroxide group are shown in red and blue spheres, respectively. B) A simulated PDS distance distribution resulting from dHis and R1 in red and blue respectively. Respective PDS time domain signals are shown in the inset.

1.4 Narrow Distributions Open New Possibilities

1.4.1 Induced Conformational Changes

The dramatic increase in resolution opens up several new possibilities, especially for many proteins where the onset of functionality involves structural transitions, such as the motion of secondary structural elements upon interaction with a substrate, lipid, another protein, or DNA. In these cases, the dHis-based distance distribution can resolve small differences in the most probable distances, down to a few angstroms.

The power of dHis for such applications is illustrated in Figure 1-4A, which shows a protein undergoing a conformational change. When labeled with dHis-Cu^{2+}-NTA, the resulting narrow distance distributions make the resolution of these two different conformations possible, even though the difference in most probable distances may be only ~3 Å. However, when using flexible nitroxide labels, the wide breadth of the distribution renders the two conformations unresolved.

The increased resolving power of dHis has been demonstrated as especially useful in monitoring the subtle conformational changes in the DNA binding helix of the Copper Efflux Regulator, CueR.[59] Here, dHis-labeled helix positions in the homodimer change by as little as 1-2 Å upon addition of a metal ion, and subsequently a DNA duplex containing the appropriate binding sequence. The resolution of such subtle conformational changes was integral in deciphering the atomic level details of the regulation mechanism.[59] Similar principles were applied in determining two conformations of the functional helix in hGSTA1-1, a detoxification enzyme.[60] These works clearly emphasize the immense advantage of the resolution of dHis-based distance distributions that would be otherwise obfuscated by the large conformational flexibility of the nitroxide label.

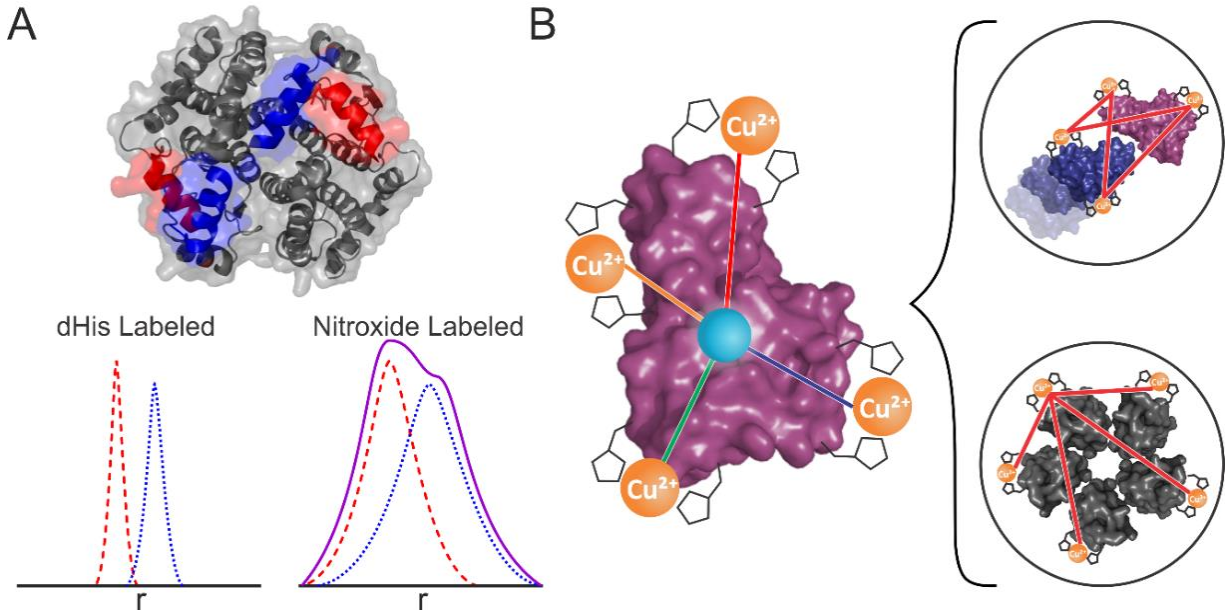

Figure 1-4 A) Illustrative example of the dHis motif's application to detecting conformations and conformational changes in proteins with high resolution inaccessible through flexible nitroxide labels. B) Illustrative examples of the principles of Cu^{2+}-based multilateration (left) to protein-protein docking (top right), and quaternary assembly (bottom right).

1.4.2 Localization of Metal Ions

In Chapter 3, we present work that showcases the power of the dHis motif's narrow distance distributions in the location of a native metal binding site within a protein. Up to 50% of known enzymes require a metal ion to function,[61] and metal cofactors can dictate catalytic activity and protein functionality. However, the location of these native metal binding sites in many proteins is not identified even when the protein structure is known. In such cases, the distance(s) between the native paramagnetic metal ion and several strategically placed dHis labeled sites can be exploited to determine the location of the native site. The strategy is illustrated in Figure 1-4B. In recent work, the location of a native metal binding site was unambiguously determined by dHis measurements, using the minimum amount (4) of necessary constraints.[62] In order to achieve a similar resolution using nitroxide labels, a substantially larger number of distance constraints (6-15) are typically needed.[63-64] A thorough discussion of these results are included in Chapter 3.

However, these principles have much broader implications than the location of metal binding sites alone. Analogous techniques may be employed to determine the spatial arrangement of proteins in conjunction with other proteins or DNA, monitor substrate binding, or to elucidate quaternary structural arrangements (cf. right panel of Figure 1-4B). The increased resolution of the dHis method can drastically lower the number of measurements needed, and can greatly increase the resolution of the structural determinations.

1.5 Orientational Selectivity at X and Q-band

In Chapter 4, we further advance the application of the dHis motif by employing high frequency EPR to determine the relative orientations between two dHis-bound Cu^{2+} centers. When performing PDS, and specifically DEER, on Cu^{2+}-based systems to elucidate narrow distance distributions with dHis, an important consideration is that the pulses employed excite only a small fraction of the total EPR spectrum. In practical terms, such finite excitation can lead to the selection of only some molecular orientations, which leads to dependence of experimental data on the magnetic field, as illustrated in Figure 1-5A. In this case, multiple experiments at different magnetic fields may need to be collected and averaged in order to measure the distance. A detailed theoretical discussion is presented in Chapter 4. A wide variety of data has shown that orientational selectivity is not observed for the Cu^{2+}-NTA dHis system at X-Band (~9.5 GHz) but is observed at Q-band (~35 GHz).[53, 65]

This result is especially intriguing given the localized nature of Cu^{2+} in the labeling scheme, and the large spectral width and high anisotropy of the metal ion. Orientational effects for this label have recently been thoroughly understood through the combination of EPR experimentation, force-field parameterized MD simulations, and quantum mechanical calculations.[66] Cu^{2+} binding to dHis is elastic and MD simulations show fluctuations in the bond lengths and bond angles between the Cu^{2+} center and its coordinating atoms, as shown in Figure 1-5B. [66] These fluctuations lead to a distribution in the orientation of the g-tensor. Figure 1-5C shows the directions of the $g_{\parallel}$ axes calculated using ORCA[67-68] from 100 frames of a 200 ns MD simulation. Consequently, there exists a large variation in the three angles that define the relative orientations of the two g-tensor

axis systems (cf. Figure 1-5C). For dHis, the standard deviations of χ, γ, and η as defined in Figure 1-5C were found to be above 10^{o} for GB1.[65-66]

This effect can be simply visualized as shown in Figure 1-5D. Here we show GB1 mutated with two dHis-Cu^{2+}-NTA sites. The $g_{\parallel}$ axis for one of the Cu^{2+}-NTA complexes was calculated and aligned across 100 individual MD frames, shown as a red sphere in the center. The positions of the second Cu^{2+} center in each frame are then shown as black spheres. From this illustration, we see that even at a single orientation of $g_{\parallel}$, there are a wide range of positions and orientations of the second Cu^{2+}, which equates to a broad range of molecular orientations that are selected in PDS. This range of orientations is sufficient to 'wash out' orientational effects at X-Band frequencies.

On the other hand, the elasticity of dHis tag is delicately poised, such that orientational selectivity can be observed for dHis-Cu^{2+}-NTA at Q-Band frequencies under certain circumstances. The increased spectral width at the higher frequency, coupled with a rigid protein structure can be enough to overcome the g-tensor distribution inherent in the dHis motif. In such cases, Q-band DEER can be exploited to expand the structural information measured by EPR.[54, 65] Chapter 4 of this thesis will show that the Q-Band DEER data acquired at many different magnetic fields along the Cu^{2+} spectrum may be simulated to yield the relative orientation between the g-tensors of the two dHis-bound Cu^{2+} ions.[65] More importantly, these g-tensor orientations are generally correlated to the orientations of the protein subunits to which the dHis motif was applied. Thus, DEER has the potential to determine the relative orientation of two secondary structural elements in a protein, which is especially important in cases in which PDS distance analysis alone is ambiguous. This aim is illustrated in Figure 1-5E, in which a potential protein undergoes an induced conformational change. Using the dHis-based EPR techniques discussed so far, the

structural differences can be resolved by both distance measurement at X-band and by measurement of change in orientational angles at Q-band.

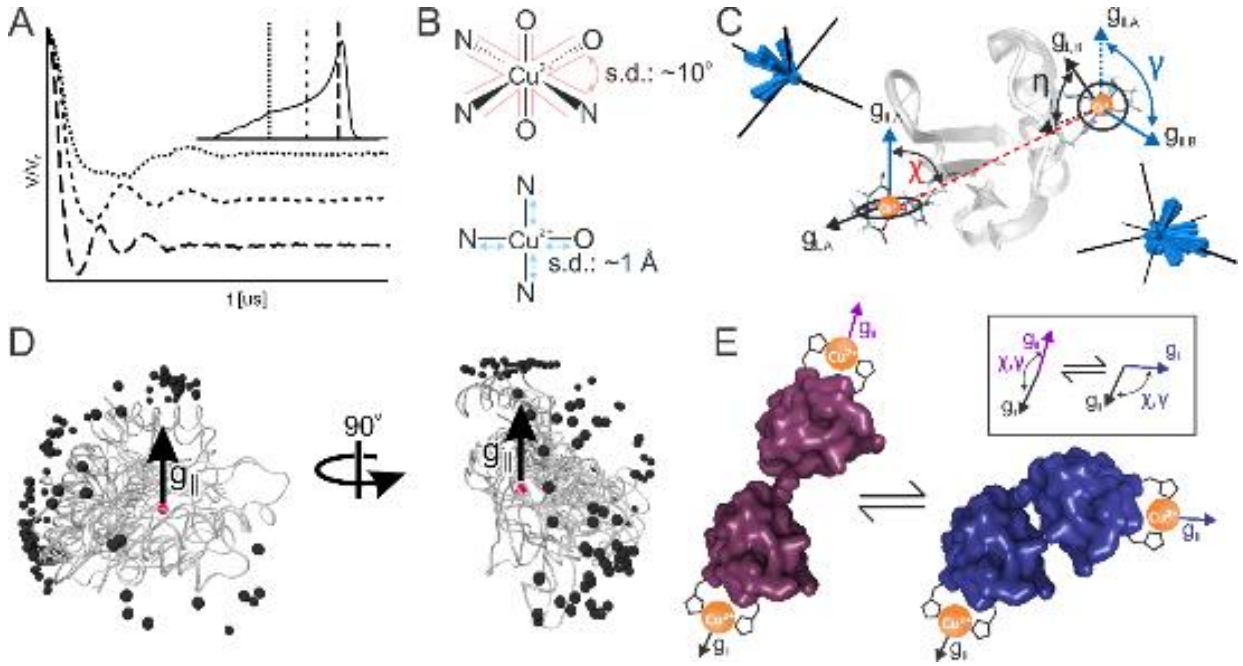

Figure 1-5 A) Illustration of orientational selectivity leading to different PDS signals when performed at different magnetic fields, indicated in the inset. B) Cu^{2+}-NTA coordination environment, with bond angles (top) and bond lengths (bottom) noted with average standard deviations. C) A distribution in g-tensor orientations resulting from the fluctuations in bond length and angles. Relative orientations of the g-tensors are illustrated, defined by χ, γ, and η. D) 100 frames of double-dHis labeled GB1 taken from MD simulations with the g_I axis of one Cu^{2+} center (shown in red, and calculated from the MD simulation via ORCA) aligned. The positions of the other Cu^{2+} center is shown in black, illustrating the wide range of molecular orientations accessible at a single g_I position. E) Illustration of the power of orientational analysis for determining structural constraints in proteins.

1.6 Combining PDS Constraints with Modeling

PDS measurements provide sparse distance constraints and therefore an especially important avenue is to combine EPR with molecular modeling approaches in order to glean information about structural fluctuations in biomolecules. As mentioned previously, bespoke force-field parameters for the dHis-Cu^{2+} labels have been developed and MD simulations have been used to extract atomistic details.[66] Additionally, a coarse-grained modeling technique has also been developed, which relies on elastic network modeling to provide insight into large scale conformational changes.

The dHis, motif has been introduced into the multiscale modeling of macromolecules (MMM) software package.[47, 69] MMM utilizes in silico protein labeling to predict PDS distances from a given protein structure as well as elastic networking modeling to generate possible protein conformations based on PDS distance constraints. The use of EPR distance constraints in combination with MMM is especially important for slow, large amplitude conformational shifts of proteins from one functional state to another, although this strategy sacrifices fine atomistic structural insight and introduces intrinsic assumptions about protein motion. Alternatively, the development of force field parameters has recently enabled the use of MD simulation to gain atomistic understanding of such fluctuations.[66]

Notably, the distributions predicted from MD are found to match the experimental data well for dHis-Cu^{2+} labeled proteins.[66] Such initial results are especially promising given the difficulty in accurately combining MD with nitroxide based restraints.[30-31] In addition to angstrom-level information regarding distances and protein conformations, these MD simulations have provided numerous other insights. For example, a detailed understanding of the fluctuations in the

Cu^{2+} coordination within the chelating NTA and the dHis motif was made is accessible. Additionally, as discussed previously, a picture of such fluctuations could be translated into an estimate of the Cu^{2+} g-tensor values and orientations using the program ORCA.[67-68] This g-tensor data has shed light on the phenomenon of orientational selectivity within the dHis system at X- and Q-band, and may be used to correlate orientational information from PDS data to the protein structure at Q-band. Finally, the MD runs can be used to estimate the reorientational correlation times and order parameters for Cu^{2+}.[44] These results were crucial for establishing the use of dHis as an assay of site-specific dynamics in proteins.

1.7 dHis-Inspired Cu^{2+} Labeling in Nucleic Acids

The principles behind the success of the dHis motif may also be applied to DNA – namely the characteristic bifunctional coordination to a Cu^{2+} ion by two separate 'arms,' and the positioning of the Cu^{2+} ion near the relevant biomolecular backbone.[70] In Chapter 5, we present such a strategy for peptide nucleic acids (PNA).[37] PNA is a synthetic nucleic acid that is notable for its strong, stable duplexation with other PNA strands, or single and double stranded DNA or RNA.[71-72] The label utilizes two 8-hydroxyquinoline groups that replace complementary bases in a PNA helix, such that they coordinate a Cu^{2+} ion, as shown in Figure 1-6.[37] This label combines the bifunctional Cu^{2+} coordination of the dHis motif and ensures that the Cu^{2+} center is inside the PNA duplex to provide relevant backbone-backbone distance measurements. In addition, the label produced remarkably narrow distance distributions with a FWHM of 2 Å. The distribution in the g-tensor orientations due to fluctuations in the bond-lengths and angles ensure that the data is not

orientational selectivity at X-band despite the label rigidity.[37] There is, therefore, much promise that such a labeling scheme may be applied to other nucleic acids such as DNA to provide a rigid, site specific label.

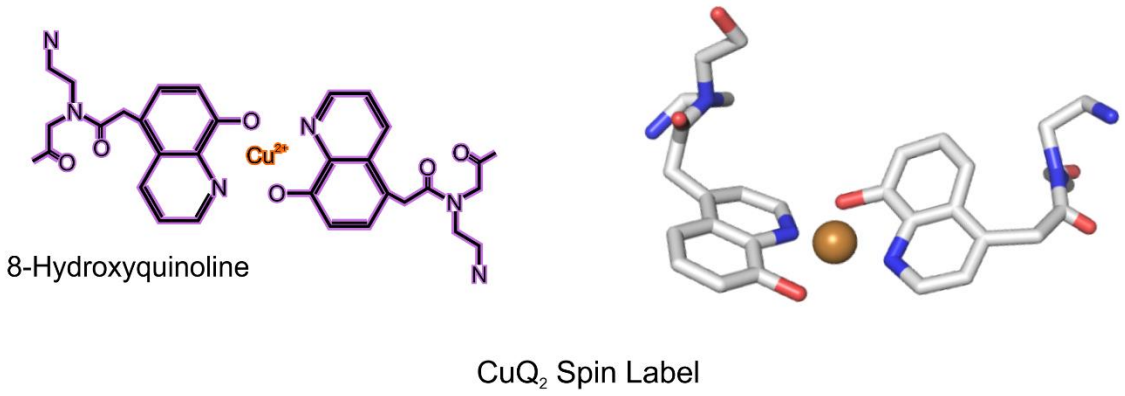

Figure 1-6 Chemical structure (left) and 3D model of the CuQ_2 spin label for PNA.

1.8 Summary and Outlook

The dHis motif has been shown as a powerful, simple, robust technique that can provide a wealth of knowledge and information regarding the structure, conformations, dynamics, and orientations of proteins. This method provides advantages over traditional nitroxide based spin labels in terms of simplicity of labeling, narrowness of PDS distance distributions, and straightforward orientational analysis.

2.0 Buffer Effects on Site Directed Cu^{2+}-Labeling Using the Double Histidine Motif

This work, in collaboration with Josh Casto and Sunil Saxena, was published in the Journal of Magnetic Resonance, 2020, Volume 320. The thesis author performed all spectroscopic experimentation, data analysis, and prepared the manuscript.

2.1 Introduction

The dHis-Cu^{2+} labeling scheme has enabled EPR distance distributions significantly narrower than common spin labels, allowing the efficient deduction of relevant biophysical information, such as distinguishing between protein conformations,[60] monitoring conformational changes,[59] assessing three-dimensional protein arrangement, which has implications for protein-protein and protein-DNA interactions, quaternary structural arrangement, and native metal binding site location,[62] as well as determining the relative orientation of protein subunits.[65] In addition, lineshape analysis of the room temperature continuous wave EPR spectrum of the Cu^{2+}-labeled protein provides a new way to directly measure site-specific backbone dynamics at both α-helical and β-sheet sites.[44]

However, Cu^{2+} forms complexes easily with many ligands, and therefore there are additional considerations in the implementation of the dHis motif that are not present with nitroxide labeling. First, Cu^{2+} may experience interactions with certain amino acid sidechains,[73] leading to non-specific coordination. This complication is mitigated by labeling with Cu^{2+}

complexed to nitrilotriacetic acid (NTA) rather than a Cu^{2+} salt .[34] The ligand, NTA, occupies four of the six coordination sites of Cu^{2+}, leaving two sites open for cis-coordination to two histidine sidechains, and has been shown to effectively prevent nonspecific binding of Cu^{2+} elsewhere in the protein. However, besides the protein, the solvent presents an additional source of competition for Cu^{2+}-NTA binding to a dHis site.[74] Many buffers commonly used with protein systems have the potential to interact with Cu^{2+} complexes, which can hinder the efficient labeling of the dHis mutated protein.

These considerations may make adoption of the dHis motif non-intuitive. To ameliorate these issues, we present herein two contributions to aid in the widespread use of dHis based labeling. We present a systematic investigation of Cu^{2+}-NTA labeling of dHis modified proteins in five commonly used buffer systems. We use EPR and UV/Vis assays to determine the efficiency of labeling in each buffer environment to highlight the considerations one must make when applying this technique to any protein. Second, we offer a step-by-step protocol of the preparation of the Cu^{2+}-NTA complex and the labeling of dHis mutated proteins, along with representative EPR and UV/Vis experimental controls to provide the expected results and ensure proper labeling. The work presented herein will enable the easier adoption of this technique and promote its widespread use throughout the broader scientific community.

2.2 Materials and Methods

2.2.1 Preparation of Cu^{2+} and NTA Stock Solutions

The preparation for the Cu^{2+}-NTA stock was adapted from prior literature,[75] and is included here for ease of referencing. To begin, we first adjusted the pH of an aliquot of standard deionized water to pH 12. Throughout this work, all pH adjustment was achieved by the addition of NaOH to increase pH or HCl to decrease pH. We then dissolved our crystalline NTA (99%, Acros Organics) into the pH 12 deionized water to achieve a concentration of 100 mM NTA. As the solvation of the NTA alters the pH of the solution, continued monitoring and adjustment of the pH may be necessary to ensure the NTA completely dissolves. Next, we prepared a separate buffer solution of 0.1 M MOPS and 0.1 M NaCl in deionized water. This buffer solution was pH adjusted to pH 7.0. We then took an aliquot of the 100 mM NTA solution and diluted it to 3 mM in the MOPS buffer solution. This solution is referred to as our NTA stock solution. We then prepared a Cu^{2+} solution. We first took a new aliquot of deionized water and adjusted its pH to 2.0. We then dissolved $CuSO_4 \cdot 5H_2O$ in that deionized water to a concentration of 3 mM $CuSO_4$. This solution is referred to as our Cu^{2+} stock solution.

2.2.2 EPR Measurements

All experiments were performed on a protein containing two dHis sites as would be usual for distance measurements. Plasmid mutagenesis and protein expression and purification for all protein mutants were performed using standard procedures.[32, 76-77] Protein samples were stored in

150 mM NaCl and 50 mM sodium phosphate buffer at pH 6.5 at 4° C for up to a week or flash frozen with 20% v/v glycerol and stored indefinitely at -80° C. The frozen protein was passed through five HiTrap 5 mL desalting columns into the above buffer before labeling to remove the glycerol.

EPR samples were prepared in 50 mM of the respective buffer, with 100 μM protein and 200 μM Cu^{2+}-NTA. 20% v/v glycerol was added as a cryoprotectant. Samples were placed in 3 mm I.D. quartz tubes and refrigerated at 4° C for 35 minutes, then transferred on ice to be immediately flash frozen in liquid MAPP gas.

Continuous wave (CW) EPR measurements were performed on a Bruker Elexsys E680 CW/FT X-band spectrometer using a Bruker ER4118X-MD5 resonator at 80 K. All CW EPR experiments were run with a center field of 3100 G and a sweep width of 2000 G, a modulation amplitude of 4 G and a modulation frequency of 100 kHz for 1024 data points using a conversion time of 20.48 ms. CW EPR simulations were performed with EasySpin.[78]

Three-pulse electron-spin echo envelope modulation (ESEEM) experiments[79] were performed on a Bruker Elexsys E680 CW/FT X-band spectrometer using a Bruker ER4118X-MD4 resonator at 20 K except where noted. A $\pi/2$ –t– $\pi/2$ – T – $\pi/2$ – echo pulse sequence was used. The $\pi/2$ pulse length was 16 ns. The first time delay, t, was set to 140 ns and the second time delay, T, was set to 280 ns and was incremented by a step size of 16 ns. All experiments were performed at the magnetic field corresponding to the greatest intensity on the echo-detected field swept spectrum. A four-step phase cycling was employed to filter out unwanted echoes.[80] Data was averaged over three scans. The resultant signal was phase corrected, baseline subtracted and Fourier-transformed using the Bruker Xepr software. The magnitude of the Fourier transformed spectrum is presented.

Four-pulse double electron electron resonance (DEER) measurements[12, 48] were performed on a Bruker Elexsys E680 CW/FT X-band spectrometer using a Bruker EN4118X-MD4 resonator at 20 K. Temperature was controlled by an Oxford ITC503 temperature controller and an Oxford CF935 dynamic continuous flow cryostat connected to an Oxford LLT 650 low-loss transfer tube. The pulse sequence used was $(\pi/2)_{v1}$-τ_1-$(\pi)_{v1}$-τ_1+t-$(\pi)_{v2}$-τ_2-t-$(\pi)_{v1}$-τ_2-echo. The observer $(\pi/2)_{v1}$ and $(\pi)_{v1}$ pulses were 16 ns and 32 ns respectively. The pump $(\pi)_{v2}$ pulse was 14 ns. t was increased by a step size of 10 ns over 128 points. The time domain data was analyzed by Tikhonov regularization. Data acquisition lasted approximately 5-8 hours. DEER data was processed using DeerAnalysis2018.[4]

2.2.3 UV/Vis Measurements

UV/Vis experiments at 8° C were performed on a Varian Cary 50 Bio spectrophotometer using a self-masking quartz spectrophotometer cuvette with a 10 mm path length from Starna Cells. UV/Vis spectra were measured from 220-600 nm except where noted. All measurements were baseline corrected using a blank of the respective buffer, and were performed in single beam mode. Data was collected with the Cary WinUV software. UV/Vis samples used 1.2 µM protein with 20% v/v glycerol. Data points in the titrations with protein were collected 15 minutes after adding an aliquot of Cu^{2+}-NTA. Each reported absorbance was corrected for dilution. For the kinetic time scan, each data point was averaged for 5 seconds, with 10 seconds in between each collection. Additional UV/Vis titrations were performed at 4° C on a Thermo Scientific Nanodrop 2000 and analyzed using the Nanodrop 2000 software package. UV/Vis spectra were monitored at 340 nm. Samples contained 3 µM protein and were blanked with their respective buffer.

2.3 Results and Discussion

2.3.1 UV/Vis Determines Optimal Cu^{2+} to NTA Ratio

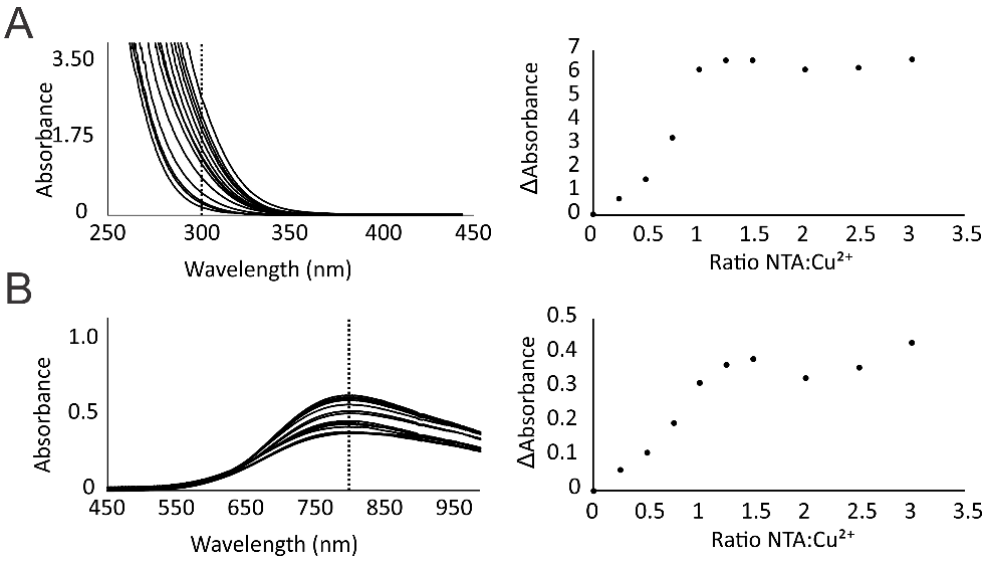

Figure 2-1 UV/Vis titration of stock NTA solution into stock $CuSO_4$ solution. This titration was monitored at two separate wavelengths, A) 300 nm and B) 800 nm. The left plots show the experimental UV/Vis spectrum in the particular range that was monitored. The right plots show the change in absorbance on increasing the amount of NTA in the sample. This UV/Vis data indicates that stoichiometric amounts of Cu^{2+} and NTA should be added for optimum chelation.

For optimal spin labeling of a protein, maximum chelation of Cu^{2+} by the NTA is desired to ensure removal of free Cu^{2+} which can potentially bind non-specifically. To determine the ideal ratio of NTA to Cu^{2+}, we performed a UV/Vis titration of our NTA stock solution into our Cu^{2+} stock solution, shown in Figure 2-1. The Cu^{2+} and NTA stock solutions were prepared as described in the Experimental section. This titration was monitored at two wavelengths, 300 nm and 800 nm, which are representative of NTA coordinating to Cu^{2+}.[81] The titration curve for 300 nm, shown in

Figure 2-1A, plateaus at 1 equivalent of NTA:Cu^{2+}, and the 800 nm curve, shown in Figure 2-1B, plateaus around 1.25 equivalents. This plateauing of the UV/Vis signal indicates a maximal chelation of NTA onto the Cu^{2+} at approximately stoichiometric ratios. Therefore, to prepare our Cu^{2+}-NTA stock solution, we mixed equal volumes of the Cu^{2+} stock with the NTA stock. This final solution was pH adjusted to the desired pH. For our experiments, this value is the physiological pH, 7.4.

We then characterized this Cu^{2+}-NTA stock solution by EPR as shown in Figure 2-2. These EPR experimental results serve as controls to verify the proper preparation of the Cu^{2+}-NTA stock solution. First, we performed continuous wave (CW) EPR on the stock solution of Cu^{2+}-NTA with 20% v/v glycerol as a cryoprotectant. The CW EPR spectrum in shown in Figure 2-2A. The spectrum was simulated to determine the characteristic EPR parameters, $g_{\parallel}$ and $A_{\parallel}$, which can serve as indicators of the Cu^{2+} coordination environment. Notably, the CW EPR spectrum shows no component that can be attributed to free Cu^{2+}, as shown in Figure 2-2A, which indicates that all the Cu^{2+} has indeed coordinated with NTA. The Cu^{2+}-NTA spectrum was fit best with two components, with their $g_{\parallel}$ and $A_{\parallel}$ values noted in Figure 2-2A.

The Cu^{2+}-NTA complexes have several possible coordination modes, which may explain the two observed components in the Cu^{2+}-NTA spectrum.[82] The first component, with $g_{\parallel}$=2.3082 and $A_{\parallel}$=144 G, is consistent with a coordination of one nitrogen and three oxygens in the equatorial plane.[83] This component comprises approximately 80% of the total spectrum. The second component displayed a higher $g_{\parallel}$ and a lower $A_{\parallel}$ ($g_{\parallel}$=2.3321 and $A_{\parallel}$=135 G), a trend that is consistent with increasing oxygen coordination.[83] This coordination environment is possible with the nitrogen of the NTA ligand coordinating axially to the Cu^{2+}, with four equatorial oxygens. These proposed coordination modes are illustrated next to their respective EPR spectra in Figure 2-2A.

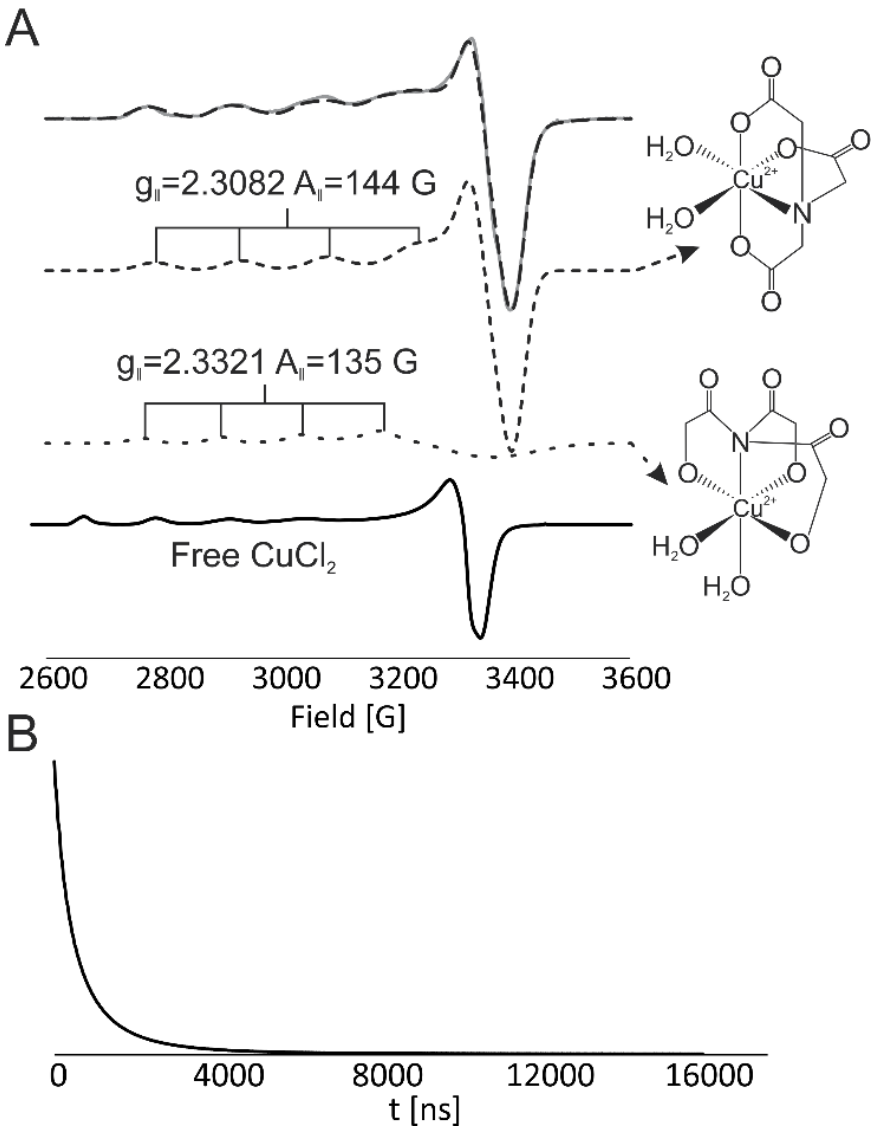

Figure 2-2 A) X-Band CW EPR spectrum of the Cu^{2+}-NTA stock. Experimental spectrum of the Cu^{2+}-NTA stock is shown in gray at the top with total simulation shown as a black dashed line. Individual simulation component spectra are shown below in dashed lines with g_I and A_I parameters noted. The corresponding chemical structures of the proposed coordination modes are shown to the right of the respective spectra. The bottom spectrum shows that of free $CuCl_2$ (in water) for comparison. B) ESEEM signal of the Cu^{2+}-NTA stock performed at 80 K. This data indicates full complexation of Cu^{2+}-NTA, and gives a simple visual assay for proper stock preparation.

It is well established that Cu^{2+} has high affinity for NTA, with a sub-picomolar apparent dissociation constant, K_d.[84] This high affinity is evident from our CW spectra in Figure 2-2A, which showed complete complexation of the Cu^{2+} with the NTA ligand. Note that the interaction of Cu^{2+} with two imidazole ligands is likewise well studied, with a K_d of 270 μM.[85] This affinity suggests a relatively weak binding of free Cu^{2+} to two histidines. However, the Cu^{2+}-NTA complex with two histidine residues shows a K_d of 100 μM, a factor of approximately 3 better than Cu^{2+} alone.[86] This data supports the implementation of NTA with the dHis motif.

We next performed electron spin echo envelope modulation (ESEEM) on the Cu^{2+}-NTA stock. ESEEM is sensitive to nuclear spins within 3-8 Å of the Cu^{2+} electron spin, which are identified by modulations in the time domain signal. This signal is shown in Figure 2-2B. Notably, there are no visible nuclear modulations. This result is expected, as the Cu^{2+}-NTA should only have directly coordinated nitrogen atoms, which are not detected due to the finite bandwidth of the pulses in the experiment. Note that we performed this and all following ESEEM experiments in such a manner to filter out nuclear modulations arising from interactions with hydrogen in the solvent.[39]

2.3.2 UV/Vis Assesses Optimal Ratio of Cu^{2+}-NTA to Protein for Distance Measurements

The dHis motif, as shown in Figure 2-3A, requires the incorporation of two histidine residues placed in strategic locations within the protein. The dHis motif has been successfully used in both α-helices and β-sheets. For β-sheets, as shown in Figure 2-3B, the histidine residues are placed in an i, i+2 arrangement. This allows both histidine residues to face the same plane of the β-sheet in order to coordinate the Cu^{2+}-NTA. For α-helices, the histidine residues should be

positioned in i, i+4 positions. In this arrangement, the two histidine residues point the same direction from the helix for Cu^{2+}-NTA coordination. In principle, the dHis motif can make use of native histidine residues, which can simplify the mutation process. As with other spin-labeling methods, it is advantageous to position the dHis site in a solvent exposed region of the protein to enable efficient loading of the Cu^{2+}-NTA into the site. Additionally, Cu^{2+}-NTA shows a higher affinity for α-helical dHis sites.[34-35]

Incorporation of non-native histidines was achieved through standard mutagenesis, protein expression and purification procedures.[32, 76-77] In this work, all results were obtained on a tetramutant of the immunoglobulin binding domain of protein G (GB1) with dHis sites at a β-sheet, 15H/17H, and an α-helical site, 28H/32H. This protein system is well characterized and has been used for much of the development of the dHis motif.[32-34, 62, 65]

We next used UV/Vis titrations to determine the optimal amount of the Cu^{2+}-NTA for labeling proteins. Such considerations are important because excess Cu^{2+}-NTA contributes to the background signal in pulsed dipolar spectroscopy which leads to a loss of sensitivity towards the intramolecular dipolar interaction. Cu^{2+}-NTA stock was titrated into a sample containing 1.2 μM GB1 in a buffer of 50 mM sodium phosphate buffer at pH 7.4 (Figure 2-4A), and a sample in 50 mM N-ethylmorpholine (NEM) at pH 7.4 (Figure 2-4B). Both samples contained 20% v/v glycerol to examine binding under conditions typically used for low-temperature EPR. Sodium phosphate was chosen as a simple representative buffer because previous work has determined the K_d of Cu^{2+}-NTA to dHis in this buffer system.[35] NEM was used as it has been the default buffer employed in most work involving the dHis motif thus far. Additionally, the temperature was

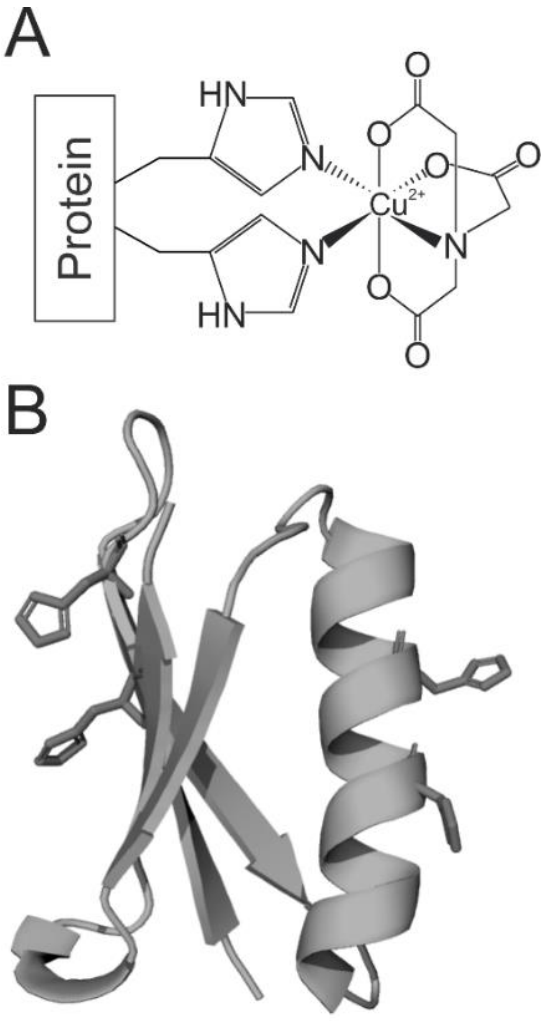

Figure 2-3 A) Chemical structure of the dHis Cu^{2+}-NTA labeling motif. B) Molecular model (PDB: 4WH4) of a model protein including a β-sheet site and an α-helical site showing the full histidine side chains for illustration.

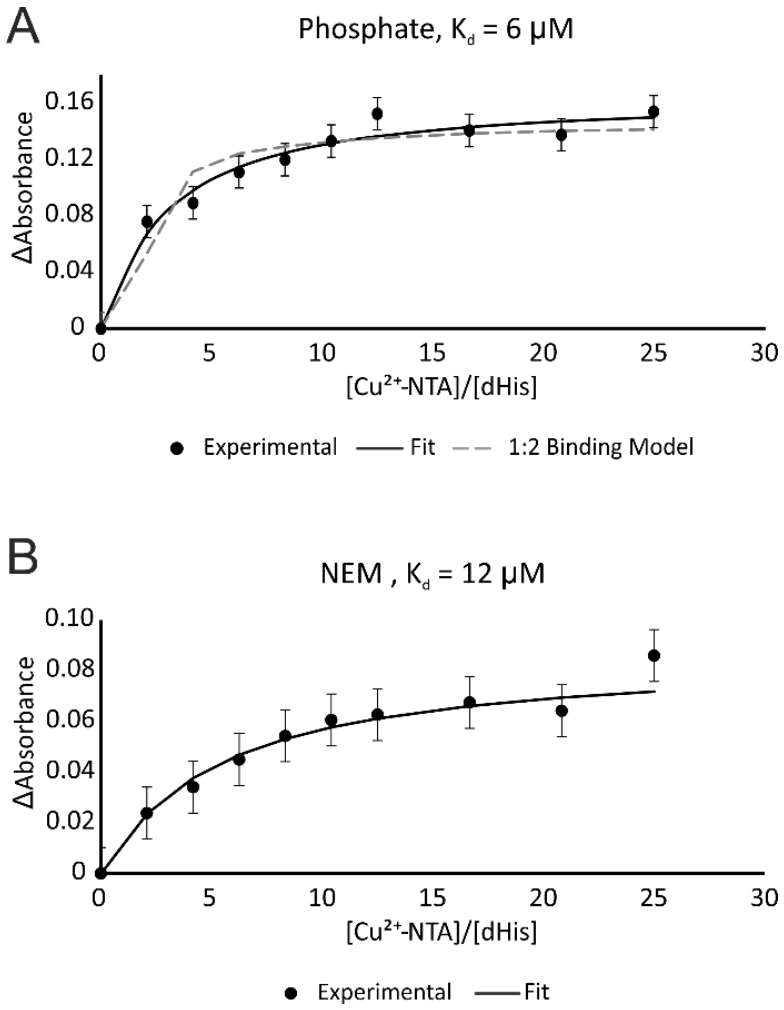

Figure 2-4 UV/Vis titrations of Cu^{2+}-NTA stock into tetramutant 15H/17H/28H/32H GB1 at 8° C. The titrations were monitored at 340 nm. A) Titration performed in 50 mM sodium phosphate buffer, pH 7.4. Black circles show experimental ΔAbsorbance values. The fit to the experimental data using a 1:1 (dHis:Cu^{2+}-NTA) binding model is shown as the solid black line. A fit to the data using a 1:2 (GB1:Cu^{2+}-NTA) with the α-helix and β-sheet Kd values previously determined by ITC is shown as the gray dashed line. B) Titration performed in 50 mM NEM buffer, pH 7.4, with a 1:1 binding model fit as above. This data shows slight effects of buffer on the apparent dissociation constant of Cu^{2+}-NTA to dHis.

maintained at 8° C for the duration of these titrations. Note that the binding of Cu^{2+}-NTA to dHis is exothermic and lower temperatures ensure higher binding.[35] The UV/Vis titrations were monitored at 340 nm, which corresponds to a metal-to-ligand charge transfer band.[38] The experimental changes in absorption, corrected for dilution, are plotted as black circles.

We then fit the data using a 1:1 (dHis:Cu^{2+}-NTA) binding model, detailed in Equation 2-1.[87-88] This model assumes that both α-helix and β-sheet sites experience identical binding affinities to the Cu^{2+}-NTA. While we know this is not the case,[34-35] such an assumption simplifies our model, and still provides an 'average' apparent dissociation constant, K_d, of the two sites with reasonable accuracy, as is discussed below.

$$\Delta Abs = \frac{Abs_{\Delta HG}}{2}\left[[H_0] + [G_0] + K_d - \sqrt{([H_0] + [G_0] + K_d)^2 + 4[H_0][G_0]}\right] \qquad (2\text{-}1)$$

In Equation 2-1, $[H_0]$ is the initial concentration of dHis sites, $[G_0]$ is the initial concentration of Cu^{2+}-NTA, K_d is the 'average' apparent dissociation constant, and $Abs_{\Delta HG}$ is the contribution to the UV/Vis absorbance resulting from the coordination of Cu^{2+}-NTA to dHis. In this equation, K_d and $Abs_{\Delta HG}$ are unknowns. The equation was fit to the data by minimizing the RMSD between the experimental ΔAbs and the calculated ΔAbs by changing the K_d and $Abs_{\Delta HG}$. Multiple starting seed values for K_d and $Abs_{\Delta HG}$ were used to avoid the RMSD minimization getting stuck in local minima. By this method, we calculate that K_d = 12 ± 5 μM in NEM and K_d = 6 ± 2 μM in sodium phosphate buffer. The uncertainty in these measurements was estimated from the error in the individual data points.

Previous work determined the K_d values of both α-helix and β-sheet dHis sites in GB1 at room temperature in 50 mM phosphate buffer by isothermal titration calorimetry (ITC).[35] This work determined the α-helix K_d = 5 μM and the β-sheet K_d = 42 μM at room temperature (25° C),

as well as their respective ΔH values. Using the Van't Hoff equation (Equation 2-2), we can extrapolate these K_d values at 8° C as used in our titrations, under the assumption that the ΔH does not change significantly in the range of temperatures used:

$$ln\left(\frac{K_2}{K_1}\right) = \frac{\Delta H^{\emptyset}}{R}\left(\frac{1}{T_2} - \frac{1}{T_1}\right) \quad (2\text{-}2)$$

This equation results in an α-helix K_d = 2 μM and a β-sheet K_d = 16 μM at 8° C. For the simplest and most direct comparison, we have averaged these two values to $K_{d,avg}$ = 9 μM. This $K_{d,avg}$ value is similar to our experimentally calculated value (K_d = 6 ± 2 μM). However, for a more accurate comparison, we then used the two separate α-helix and β-sheet K_d values to plot a curve following a 1:2 (GB1:Cu^{2+}-NTA) binding model. Such a model takes into account differences in affinity of each of the two distinct dHis sites within a single protein, and is described as:[87]

$$\Delta Abs = \frac{Abs_{\Delta HG1}[H_0]K_\alpha[G] + Abs_{\Delta HG2}[H_0]K_\alpha K_\beta[G]^2}{1 + K_\alpha[G] + K_\alpha K_\beta[G]^2} \quad (2\text{-}3)$$

Where $Abs_{\Delta HG1}$is the contribution to the UV/Vis absorbance resulting from the coordination of Cu^{2+}-NTA to and α-helix dHis site, $Abs_{\Delta HG2}$ is the contribution to the UV/Vis absorbance resulting from the coordination of Cu^{2+}-NTA to and β-sheet dHis site, K_α and K_β are the K_d values for the α-helix and β-sheet sites respectively, and [G] is the concentration of free Cu^{2+}-NTA. [G] is calculated as a function of knowns by:[87]

$$0 = [G]^3\left(K_\alpha K_\beta\right) + [G]^2\left(K_\alpha\left(2K_\beta[H_0] - K_\beta[G_0] + 1\right)\right) + [G](K_\alpha([H_0] - [G_0]) + 1) - [G_0] \quad (2\text{-}4)$$

The $Abs_{\Delta HG1}$and $Abs_{\Delta HG2}$ were determined with RMSD minimization as above, and the 1:2 binding fit is plotted as the gray dashed line in Figure 2-4A. This more complete model is

slightly deviated from our experimental values, but still provides a close fit to the data. The similarity between this fit and our experimental fit using an 'average' K_d suggests that our data is in agreement with the previous ITC data, and the treatment of this system as a 1:1 (dHis:Cu^{2+}-NTA) binding model is sufficient to qualitatively analyze binding for our purposes.

We next repeated the titration in 50 mM NEM buffer, shown in Figure 2-4B, and fit the experimental data. The NEM titration provided an average K_d of 12 ± 5 μM (compared to 6 ± 2 μM for the phosphate buffer). This result is an indication of the impact of buffer on the apparent K_d. The data suggests a slightly greater loading of Cu^{2+}-NTA to dHis sites in the sodium phosphate as compared to NEM buffer.

After determining the K_d, we used the calculated values to estimate the amount of dHis loading we could expect in our EPR samples to determine the optimal number of equivalents of Cu^{2+}-NTA to use. Figure 2-5A and B show plots for the percentage of dHis sites loaded in a sample of 100 μM protein at added Cu^{2+}-NTA equivalents from 0 to 3 (as the dHis binding is effectively saturated past this point) in phosphate buffer (Figure 2-5A) and NEM buffer (Figure 2-5B). The values plotted were calculated using:[87]

$$[HG] = \frac{1}{2}\left[[H_0] + [G_0] + K_d - \sqrt{([H_0] + [G_0] + K_d)^2 + 4[H_0][G_0]}\right] \quad (2\text{-}5)$$

where [HG] is the concentration of dHis-bound Cu^{2+}-NTA. The K_d used for these calculations was as determined by our titrations, with K_d = 6 ± 2 μM for phosphate and K_d = 12 ± 5 μM for NEM. From the plots in Figure 2-5A and B, we see that greater than 80% of the dHis sites are loaded at 1 equivalent and higher Cu^{2+}-NTA in both phosphate and NEM buffer. However, for EPR distance methods, the presence of excess free Cu^{2+}-NTA degrades the signal, and so the amount of free Cu^{2+} in the sample should be minimized. To this end, Figure 2-5C and D shows the component

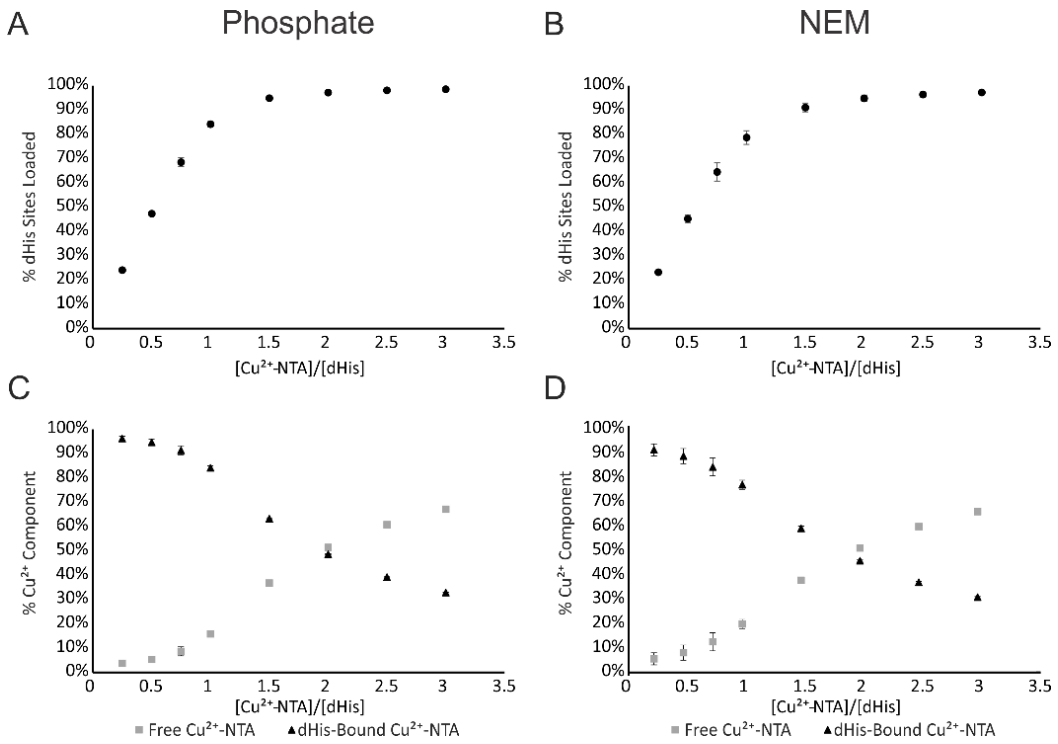

Figure 2-5 A) A plot of the expected percentage of loaded dHis sites for a 100 µM protein sample as estimated by our calculated $K_d = 6 \pm 2$ µM in phosphate buffer for 0 to 3 equivalents of added Cu^{2+}-NTA. B) A plot of the expected percentage of loaded dHis sites for a 100 µM protein sample as estimated by our calculated $K_d = 12 \pm 5$ µM in NEM buffer for 0 to 3 equivalents of added Cu^{2+}-NTA. C) A plot of the component percentages for a 100 µM protein sample as estimated by our calculated $K_d = 6 \pm 1$ µM in phosphate buffer for 0 to 3 equivalents of added Cu^{2+}-NTA. D) A plot of the component percentages for a 100 µM protein sample as estimated by our calculated $K_d = 12 \pm 5$ µM in NEM buffer for 0 to 3 equivalents of added Cu^{2+}-NTA. Free Cu^{2+}-NTA is plotted as gray squares. dHis-Bound Cu^{2+}-NTA is plotted as black triangles. These plots suggest stoichiometric addition of Cu^{2+}-NTA to dHis to compromise between 80% loading and less than 20% free Cu^{2+}-NTA.

percentages of free Cu^{2+}-NTA and dHis-bound Cu^{2+}-NTA for 0 to 3 equivalents of added Cu^{2+}-NTA for phosphate and NEM buffers using their calculated K_d values. Again, the two buffers show little difference, with both maintaining less than 20% free Cu^{2+}-NTA below 1 equivalent of added Cu^{2+}-NTA.

We also performed similar measurements at 4° C (Figure 2-6). A temperature of 4° C was chosen for incubation as it is a common temperature at which refrigerators are maintained and is therefore easily accessible. Taking all data together, we see that stoichiometric loading, or 1 equivalent of Cu^{2+}-NTA per dHis site within the protein, achieves a balance of >80% loading of the dHis sites, while keeping the total percentage of free Cu^{2+}-NTA in the sample below 20%.

We then performed a kinetic time scan to determine the details of sample incubation for optimal Cu^{2+}-NTA coordination. Two equivalents of Cu^{2+}-NTA were added to the protein sample, or 1 equivalent of Cu^{2+}-NTA per dHis site, and we monitored the UV/Vis absorbance of a protein sample at 340 nm at a temperature of 8° C. The sample was prepared in 50 mM NEM buffer, and was prepared as it would be for distance measurements, with 20% v/v glycerol. The sample was stirred for 5 seconds before loading into the cuvette and then into the spectrophotometer. The total dead time from addition of the Cu^{2+}-NTA into the protein sample to initial data collection was ~15 seconds. The results of this kinetic scan are shown in Figure 2-7. From these data, we determined that maximal loading of the dHis sites occurs after ~25 minutes sample incubation at 8° C, as the UV/Vis absorbance does not increase further after this time. These results show that for surface accessible sites, incubation for 30-40 minutes at 4-8° C should suffice to achieve maximal loading even with the slight differences in binding between buffers and temperatures. Tris buffer was also used to verify this assumption, and the data is shown in Figure 2-8. While the kinetic curves have different profiles, both buffers show maximal Cu^{2+} loading after 25-30 min.

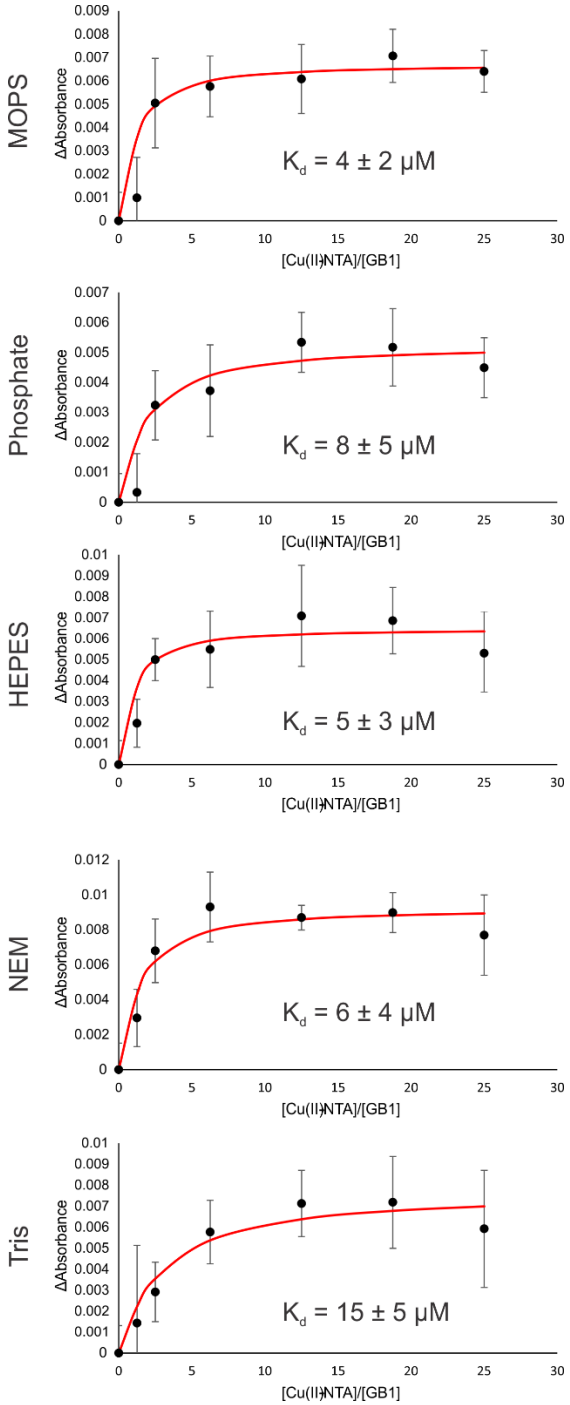

Figure 2-6 UV/Vis titrations performed at 4° C on 3 μM protein samples as prepared in the main text in each of the five buffers. Measurements were taken on a Thermo Scientific Nanodrop 2000 at 340 nm. Calculated $\mathbf{K_d}$ values are consistent with a small decrease in temperature from the 8° C titrations.

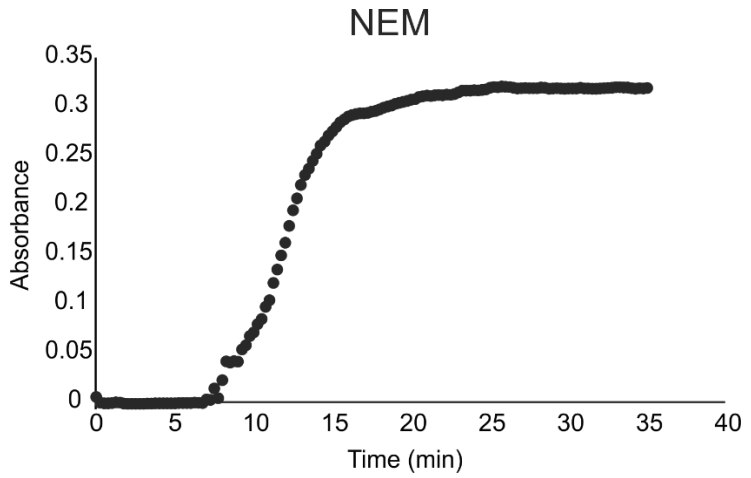

Figure 2-7 UV/Vis time scan at 340 nm to assess the amount of incubation necessary for complete coordination of the Cu^{2+}-NTA with the dHis modified protein. The system was held at 8° C for the duration. This curve shows that maximum dHis loading is achieved in less than 30 minutes at low temperature.

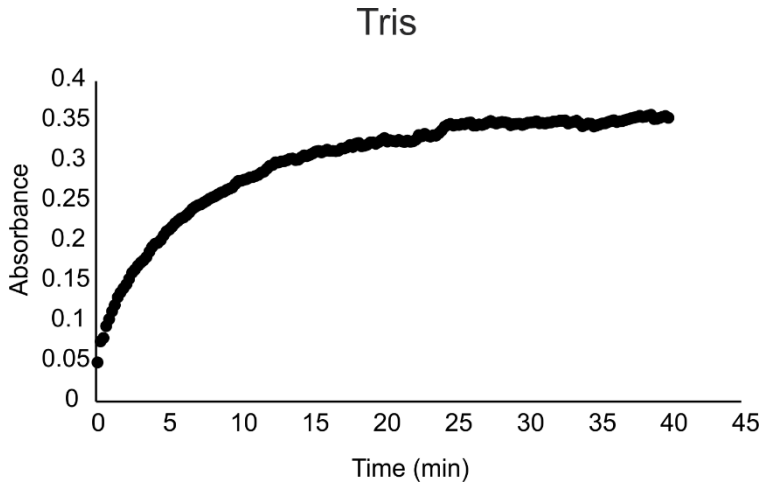

Figure 2-8 UV/Vis time scan monitored at 340 nm on a protein sample in 50 mM Tris buffer. Maximal absorbance is reached after 25-30 minutes. As tris was the least optimal buffer for use with the dHis Cu^{2+}-NTA motif, this suggests that the kinetics of Cu^{2+}-NTA binding to dHis sites is consistent across buffers.

2.3.3 Buffer Choice Affects Loading of Cu^{2+}-NTA to dHis

After determining the ideal ratio and incubation time for the Cu^{2+}-NTA dHis samples, we characterized the resulting samples by CW EPR. The data are shown in Figure 2-9. First, we performed CW EPR on samples of 100 µM Cu^{2+}-NTA stock in 50 mM of one of five commonly used buffers: MOPS (3-N-morpholinopropanesulfonic acid), Sodium Phosphate, HEPES (4-(2-hydroxyethyl)-1-piperazineethanesulfonic acid), NEM, and Tris (2-Amino-2-(hydroxymethyl)propane-1,3-diol), all pH 7.4. These free Cu^{2+}-NTA spectra are shown as the top spectra in each frame in Figure 2-9, as labeled. We then prepared samples of 100 µM protein with 2 equivalents of Cu^{2+}-NTA (1 equivalent per dHis site) in 50 mM of each buffer. Samples were incubated for 35 minutes at 4° C before being frozen.

Figure 2-9 shows the experimental CW EPR spectra of Cu^{2+}-NTA-protein compared to the spectra of the free Cu^{2+}-NTA in each buffer. Immediately apparent from these results are clear spectral shifts upon the addition of protein in all but the Tris sample, specifically in the $g_{\parallel}$ region of the spectra. The splitting due to $A_{\parallel}$ vary by as much as 40-80 G between the free Cu^{2+}-NTA sample and the sample with protein in phosphate, MOPS, and NEM buffers, and by up to 30 G in HEPES buffer. In the Tris samples however, equivalent $A_{\parallel}$ splittings varied by only up to 10 G, making the spectral shift difficult to ascertain in the broad Cu^{2+} EPR spectrum. These spectral shifts are often a clear visual indication of proper Cu^{2+}-NTA binding to dHis, and a key assay of the sample preparation. Such spectral shifts result from cis-coordination for the two histidine residues leading in an increase in the number of equatorially coordinated nitrogen atoms.[83]

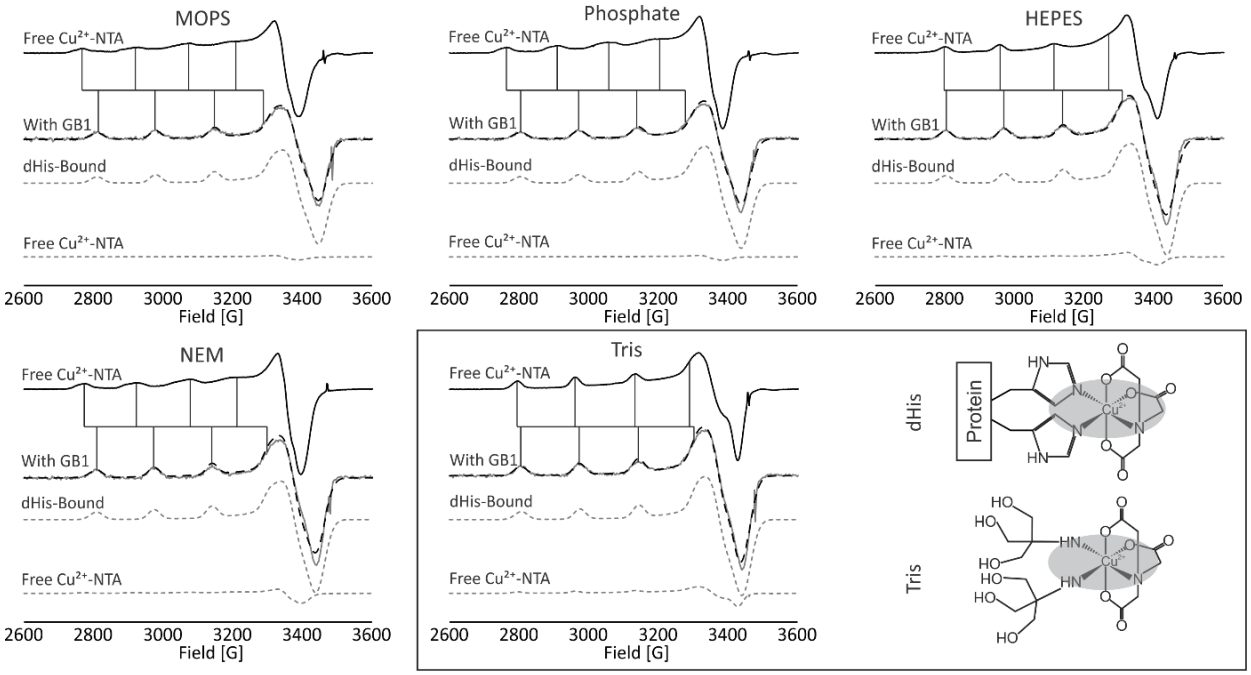

Figure 2-9 CW EPR spectra of free Cu^{2+}-NTA, and 15H/17H/28H/32H GB1 in each buffer, as labeled. The top spectrum in each frame is the free Cu^{2+}-NTA, shown as a solid black line. The middle spectrum is the GB1 sample, with the experimental spectrum in solid gray and a simulation in black dashed lines. Vertical lines are drawn tracing the A_I splitting in both spectra to emphasize the spectral shifts on addition of protein. The bottom two spectra, shown in dashed gray lines, are the dHis bound and free Cu^{2+}-NTA spectra used in the simulation. This figure emphasizes the clear visual cue that indicates Cu^{2+}-NTA to dHis binding in all but the Tris sample.

On the other hand, the sample prepared in Tris buffer shows a remarkable similarity between the spectrum without protein and the spectrum with protein. This similarity between the dHis-bound and free Cu^{2+}-NTA signal in Tris is indicative of solvent interaction with the Cu^{2+}-NTA, in which two amino nitrogens from the Tris buffer coordinate to the Cu^{2+}-NTA. Such interaction would produce a local coordination environment of the Cu^{2+} that is very similar to that of a Cu^{2+}-NTA coordinated to two histidine residues. A comparison of the coordination environments from these two cases is shown in the boxed region of Figure 2-9, with the local Cu^{2+} coordination environment highlighted. This ambiguity makes it difficult to accurately assess the extent of binding of Cu^{2+}-NTA to dHis in Tris buffer from CW EPR data alone.

To estimate the loading of the dHis sites, we performed simulations of each CW EPR spectrum. Two components were required in each case, as anticipated. The first component, labeled as dHis-Bound in Figure 2-9, represents Cu^{2+}-NTA that has coordinated to the dHis site. This component was simulated via EasySpin,[78] with variable g and A parameters, and component weight. The second component, labeled Free Cu^{2+}-NTA in Figure 2-9, is representative of Cu^{2+}-NTA that has not coordinated with a dHis site. For this component, we used the experimental spectrum of the free Cu^{2+}-NTA with a variable weight. The final simulation is a superposition of each component in ratios defined by the component weights. By fitting the g and A parameters of the dHis-Bound component, and the weights of both components, we achieve an overall simulation of the system, shown as the black dashed line overlaid on the experimental protein spectra in each frame of Figure 2-9. The results of these simulations – the g and A parameters of the dHis bound component and the percent weights of each component – are listed in Table 2-1.

Table 2-1 g and A EPR parameters for dHis-bound components in each buffer, and the percent weights for both dHis-Bound and Free Cu^{2+}-NTA components. The parameters for free Cu^{2+}-NTA for comparison are: In MOPS, Phosphate, and NEM: $g_{\parallel} = 2.308$ $A_{\parallel} = 144$ G. In HEPES: $g_{\parallel} = 2.282$ $A_{\parallel} = 158$ G. In Tris: $g_{\parallel} = 2.268$ $A_{\parallel} = 164$ G.

Buffer	$g_{\perp}$	$g_{\parallel}$	$A_{\perp}$ (G)	$A_{\parallel}$ (G)	% dHis-Bound	% free Cu^{2+}-NTA
MOPS	2.051	2.268	5	164	95 ± 5	5 ± 5
Phosphate	2.051	2.267	5	165	95 ± 5	5 ± 5
HEPES	2.051	2.268	5	164	90 ± 8	10 ± 8
NEM	2.051	2.268	5	164	89 ± 5	11 ± 5
Tris	2.051	2.272	5	165	85 ± 15	15 ± 15

From the simulation data, we observe that the choice of buffer does not have significant impact on the g and A parameters of the dHis-bound EPR spectra. The $g_{\parallel}$ and $A_{\parallel}$ values are generally consistent across every buffer, with only very slight fluctuations. This result is expected as the dHis-Cu^{2+}-NTA coordination is relatively identical in all buffers. As visualized in Figure 2-9, samples in MOPS, phosphate, and NEM buffers show distinctly different $g_{\parallel}$ and $A_{\parallel}$ values from free Cu^{2+}-NTA in the same buffers. HEPES showed slightly different parameters, although not as dramatic as the above examples. And finally, the Tris sample showed nearly indistinguishable parameters between the free Cu^{2+}-NTA sample and the sample with protein.

The component ratios show some variance of up to 10%, but these differences are difficult to quantify from CW EPR alone, due to the large errors. Additionally, the sample in Tris buffer displayed the highest uncertainty in component percentage, as the similarity of the free Cu^{2+}-NTA and dHis-bound spectra in Tris make this quantification difficult. These factors make further assays of loading necessary. On the other hand, our CW EPR results agree with our estimated loading calculated from the K_d values, in which each 100 μM EPR sample experiences upwards of 80% loading of the dHis sites.

We further assessed the binding of Cu^{2+}-NTA to the dHis sites and the impact of the buffer choice using ESEEM, shown in Figure 2-10. The ESEEM signals offer additional insight into the loading efficiency of Cu^{2+}-NTA to dHis. ESEEM is sensitive to the imidazole nitrogens found in histidine coordination (cf. Figure 2-3), resulting in the characteristic modulations exhibited in Figure 8A. However, free Cu^{2+}-NTA lacks this imidazole coordination, and as such displays no modulations, merely a featureless decay, as seen previously in Figure 2-2B. When both dHis-bound Cu^{2+}-NTA and free Cu^{2+}-NTA are present in a sample, the resulting ESEEM signal is a superposition of these modulating and featureless signals. With increasing free Cu^{2+}-NTA in a given sample, the featureless signal leads to a shallower modulation in the overall ESEEM signal. The depth or shallowness of the modulation can be quantified by the modulation depth, k, and is shown in the inset in Figure 2-10A.[42] Through this k parameter, the extent of Cu^{2+} coordination to the imidazole nitrogen of histidine can be monitored. [33, 40-41]

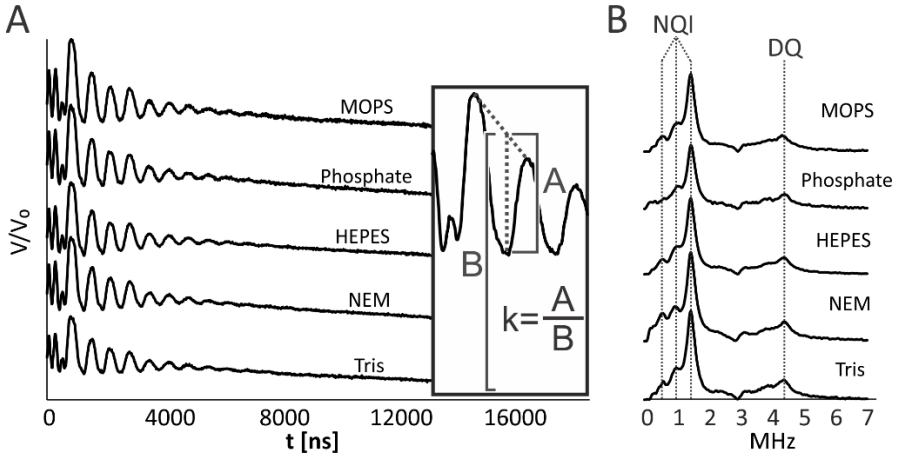

Figure 2-10 A) Time domain ESEEM signals for 2:1 Cu^{2+}-NTA:GB1 in their respective buffers. Modulation depth calculations utilized the second major modulation around 1500 ns. B) Fourier Transformed ESEEM signals for each sample in its respective buffer. These data show characteristic imidazole nitrogen coordination, indicating proper coordination of Cu^{2+}-NTA to dHis.

Notably, all samples displayed modulations of near identical frequency, but because the percentages of dHis-bound Cu^{2+}-NTA and free Cu^{2+}-NTA differ across buffers, the ESEEM modulations differ in the magnitude of these modulations. We calculated the ESEEM modulation depths for each buffer using the first major modulation that begins around 1000 ns, shown in Table 2-2. The error was estimated from the noise level of the time domain ESEEM signal. From this data, we see that using MOPS and phosphate buffers produce the deepest modulations, indicating the most efficient loading of the dHis sites with Cu^{2+}-NTA. NEM and HEPES buffers produced comparable, if slightly lower, modulation depths, while Tris buffer produced the lowest modulation depth. These results correspond well with the calculated component ratios from CW EPR, in which MOPS and phosphate buffers exhibited the highest dHis loading, with HEPES and NEM only slightly lower, and Tris buffer as the lowest.

Table 2-2 Calculated ESEEM modulation depths for the Cu^{2+}-NTA with GB1 in various buffers.

Buffer	**Modulation Depth (k)**
MOPS	27 ± 1%
Phosphate	26 ± 1%
HEPES	24 ± 1%
NEM	24 ± 1%
Tris	20 ± 1%

Figure 2-10B shows the ESEEM spectra. In all five buffer systems we see a clear and characteristic spectrum of imidazole nitrogen coordination, typified by a broad transition around 5 MHz, called the double quantum (DQ) peak, and a set of 3 transitions below 3 MHz, called the nuclear quadrupole interactions (NQI).[40-41] These transitions are all resolved in the Fourier transformed spectra, and dashed lines in Figure 2-10B trace each peak through every buffer system. This ESEEM data clearly indicates that the Cu^{2+}-NTA is coordinating to the dHis sites in all buffer systems, albeit with different loading efficiencies.

We lastly performed DEER distance measurements on each sample, as shown in Figure 2-11. The DEER distance distribution provides perhaps the most obviously useful structural data. From Figure 2-11, we see that regardless of buffer, each DEER produced a distance distribution centered on 2.3 nm, with a FWHM of 0.2 nm. This distribution is consistent with previous work.[34]

More importantly, the modulation depth, λ, of the DEER signal provides information on the amount of dHis loading in the sample. The modulation depth is the difference between the maximum signal intensity and the signal intensity at the baseline in a normalized, background subtracted DEER signal. This definition is illustrated in Figure 2-11. The modulation depth is sensitive to the number of coupled spins in the species being measured – with a higher proportion of doubly labeled proteins, the modulation depth will increase, whereas with more incomplete loading or a higher amount of free Cu^{2+}-NTA, the modulation depth will decrease. DEER modulation depth for a two-spin system is defined in simplest terms as:[33-34]

$$\lambda = 1 - [f_2(1 - p_b) + f_1] \tag{2-6}$$

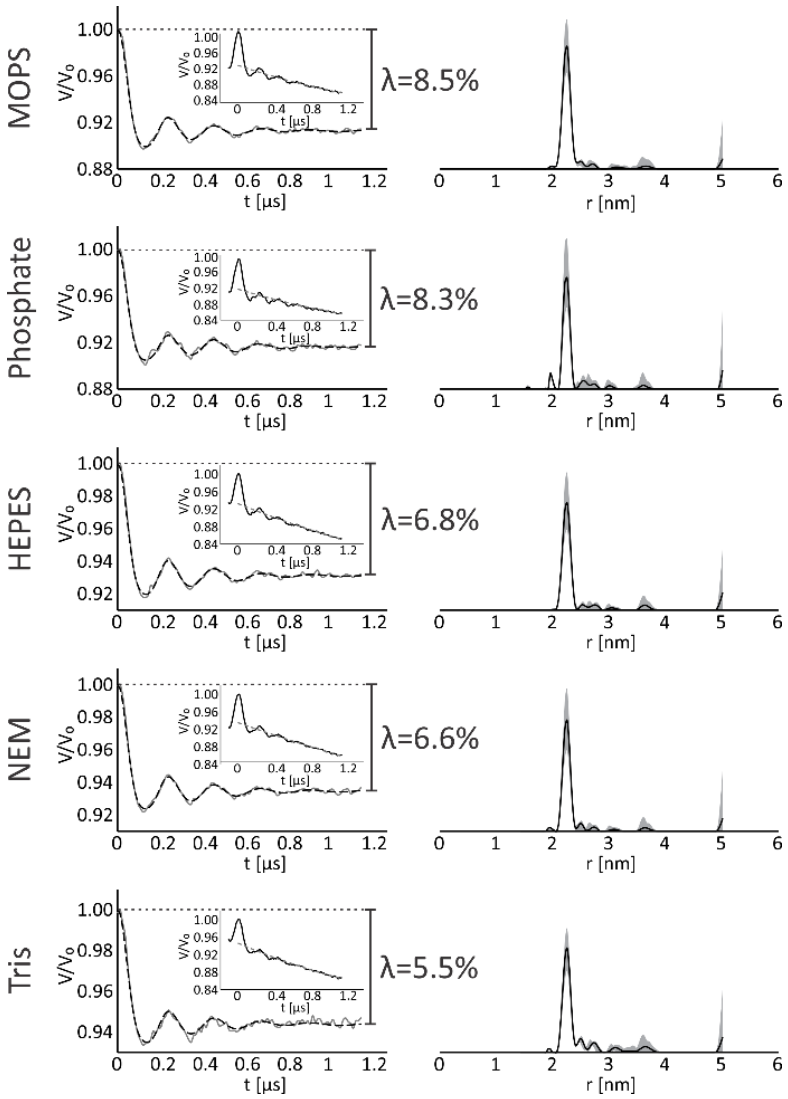

Figure 2-11 DEER data for 100 µM 15H/17H/28H/32H GB1 with 2 equivalents of Cu^{2+}-NTA, incubated at 4° C for 35 minutes in each of the five buffer systems. The left column shows the background subtracted time domain signal in gray with Tikhonov regularized fit in black dashed lines. The inset shows the raw time domain signal, with the gray dashed line indicating the background. Modulation depth parameters, λ, are noted. The right column shows the distance distributions obtained using Tikhonov regularization, with gray shading indicating the uncertainty of analysis. The data clearly show the impact of buffer on the sensitivity of the DEER technique.

Where f_2 is the fraction of doubly labeled species, and f_1 is the fraction of single Cu^{2+} species, which is comprised of both singly labeled GB1 and free Cu^{2+}-NTA. p_b is the probability of the pump pulse exciting a B spin in DEER. p_b is dependent on numerous factors such as magnetic field, microwave frequency, pump pulse shape and length, and the EPR spectrum itself, and can be calculated from the experimental echo detected field swept spectrum of the system.[89] In our analysis we estimated the error in the DEER modulation depth from the noise in the time domain signal. In order to determine the consistency and reproducibility of our modulation depth, we also performed DEER measurements on new sample preparations in phosphate buffer and Tris buffer, as representatives of most and least optimal buffers. These results are shown in Figure 2-12. From these data, the modulation depths are generally reproducible, although there are slight variations (e.g. 5.7 ± 0.1% for Tris and 7.8 ± 0.4% for phosphate (average ± s.d.)). These differences are likely due to inherent uncertainty in the measurement of concentration and volume during sample preparation.

From the DEER modulation depth and our calculated p_b, we can calculate f_2 and f_1, as:

$$f_1 = 1 - f_2 \tag{2-7}$$

Doing so for each buffer, we can holistically examine how buffer choice affects dHis loading. The results of these calculation, along with a summary of the quantitative results so far, are shown in Figure 2-13.

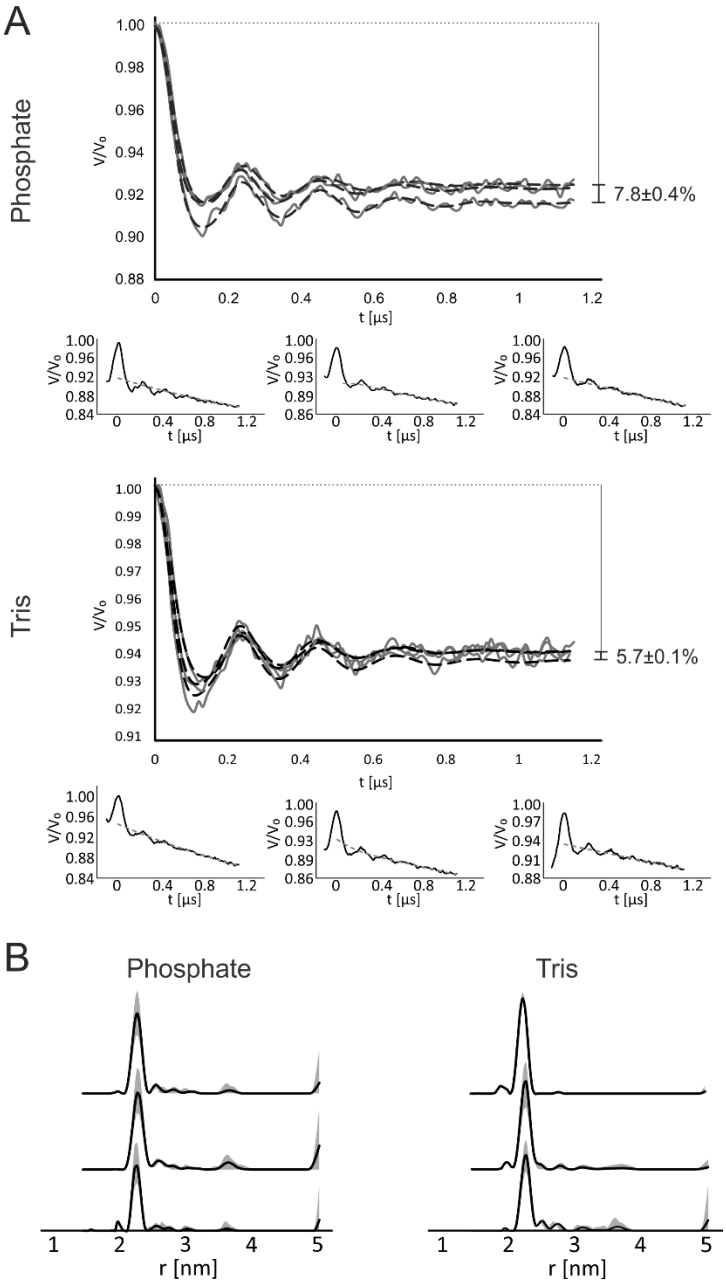

Figure 2-12 A) DEER data to test reproducibility for 15H/17H/28H/32H GB1 in 50 mM phosphate buffer as described in the main text (top) and tris buffer (bottom). Background subtracted DEER data are shown for three individual preparations of the samples, with raw time domains shown below. Average modulation depths and standard deviations are noted. B) Distance distributions for each DEER data.

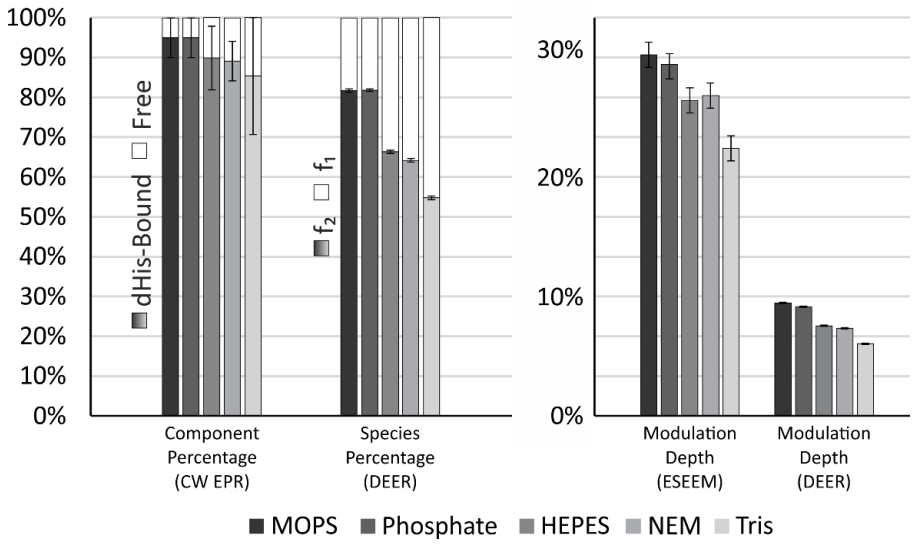

Figure 2-13 Bar graph representing the major quantifiable values derived from our CW EPR, ESEEM and DEER experiments. The trends in these values provide a consistent picture of the loading of dHis sites across buffer systems. Note that f_1 includes both free Cu^{2+}-NTA as well as Cu^{2+}-NTA bound to one dHis site.

From all the compiled results in Figure 2-13, we can see the consistent results through each experiment to fully inform our understanding of the impacts of sample preparation and buffer choice on the loading of the dHis sites. First, we can compare our DEER results with those performed previously for the Cu^{2+}-NTA system with GB1 in NEM, which reported an $f_2 = 0.50$.[34] Our NEM sample, using optimized preparation conditions, achieved an $f_2 = 0.64$, which corresponds to a 28% increase in f_2. Such an increase in f_2 can lead to significant improvements in DEER sensitivity.[90] Clearly, the optimized conditions of stoichiometric Cu^{2+}-NTA addition and low temperature incubation have major impact on the loading of the dHis sites.

Furthermore, our data indicates that buffer choice can play a role in the overall loading efficiency. If we consider both optimized preparation conditions and the optimal buffer system, our maximum f_2 across all samples is 0.82. This value is a 64% increase in loading efficiency compared to the previously published result.[34] Additionally, our EPR data is consistent across each

individual experiment, and the cumulative CW EPR component percentages, ESEEM modulation depths, and DEER species fractions indicate that MOPS and phosphate buffer promote maximal Cu^{2+}-NTA binding, with Tris buffer degrading the loading to the dHis site. It is also of note that relatively small differences in overall dHis loading, as determined from CW EPR, can have much larger impacts on the amount of doubly labeled systems for DEER. While the Tris buffer sample shows only 10% lower total dHis binding from CW EPR, this result translates to a ~33% reduction in f_2 (from 0.82 in Phosphate to 0.55 in Tris), and a ~35% reduction in modulation depth (from 0.085 in Phosphate to 0.055 in Tris).

Finally, we measured data on a different GB1 mutant to explore the generality of the observed effects of buffer. We prepared a different mutant of GB1, with dHis sites at the same α-helical site, 28H/32H, and a different β-sheet site, 6H/8H, and performed DEER on samples in phosphate buffer and in Tris, to represent the most and least optimal buffers, respectively. The DEER data is shown in Figure 2-14. The modulation depth was 5.4% in phosphate buffer and 3.3% in Tris. These data support the result that phosphate buffer promotes higher Cu^{2+}-NTA binding, whereas Tris buffer degrades it.

In general, our EPR results also align with known thermodynamic properties of these buffers and their interactions with Cu^{2+}, as specific data regarding the affinities of the buffers with Cu^{2+}-NTA is not readily available. In broad terms, Tris buffer has a higher affinity to interact with Cu^{2+} ions,[91] and likewise displayed the lowest extent of Cu^{2+}-NTA to dHis loading, whereas sodium phosphate buffer, which provided one of the greatest loadings of Cu^{2+}-NTA to dHis also exhibits a notably lower affinity to interact with Cu^{2+}.[92-93] Our EPR results and the supporting thermodynamic trends suggest that the choice of buffer is an important consideration to make when implementing the dHis motif in new systems.

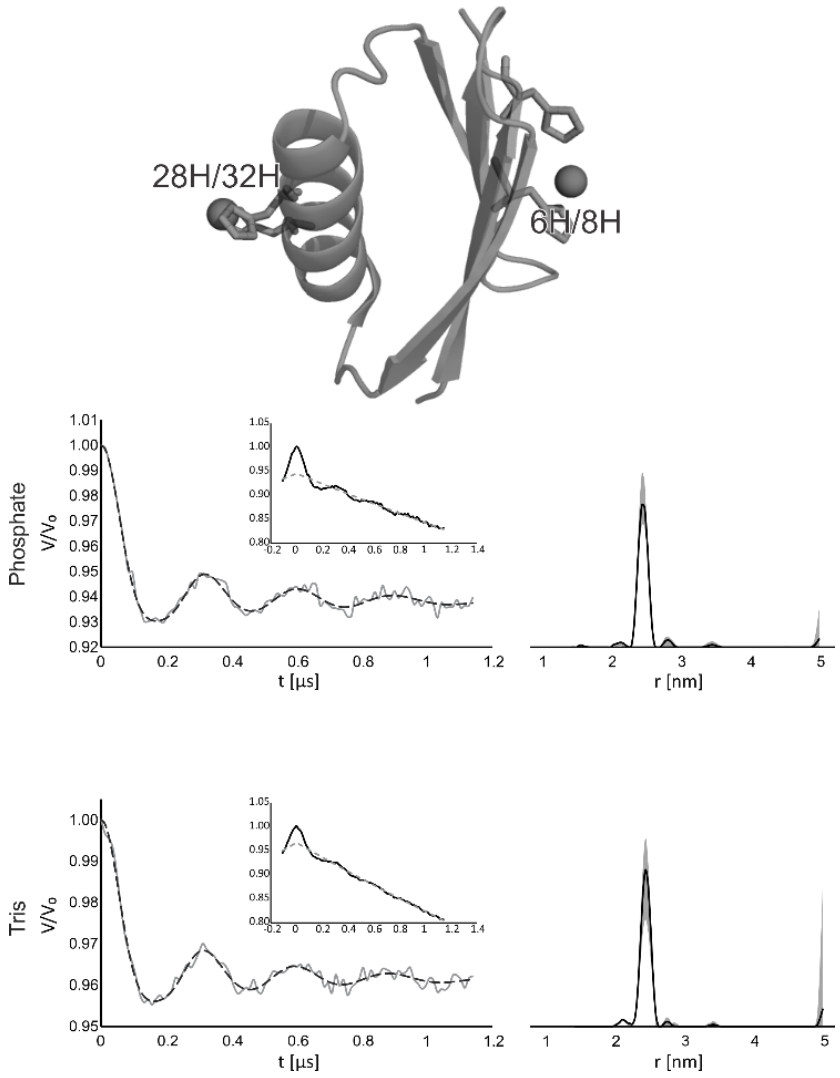

Figure 2-14 Protein Structure of 6H/8H/28H/32H GB1 with dHis sites labeled (PDB: 4WH4), Above. DEER data for 100 µM protein in 50 mM sodium phosphate and Tris buffers prepared as described previously, Below.

2.4 Conclusion

In this work, we have presented evidence that buffer conditions can affect the loading of Cu^{2+}-NTA into dHis sites for use with EPR distance methods. Our results indicate that sodium phosphate and MOPS buffers promote more efficient Cu^{2+}-NTA binding to the dHis sites, whereas Tris buffer degrades the loading efficiency. We have provided experimental control data of the expected results for each step in the labeling process used to achieve these results, most notably with regard to the incubation time and temperature of the protein and Cu^{2+}-NTA. We have demonstrated that maximal dHis loading can be achieved in less than 30 minutes at low temperature, which is an important consideration for protein research. Through this optimized labeling procedure, we show a 28% increase in doubly labeled protein compared to previously published results. When considering both the optimized loading protocol as well as ideal buffer conditions, we have achieved a fraction of doubly labeled proteins of up to ~80%. Our cumulative results provide new insights into considerations to be made when implementing the dHis Cu^{2+}-NTA system, and general optimized conditions for its use.

2.5 Acknowledgements

Funding provided by NSF MCB-2006154.

3.0 Efficient Localization of a Native Metal Ion Within a Protein by Cu^{2+}-Based EPR Distance Measurements

This work, in collaboration with Timothy Cunningham and Sunil Saxena, was published in PCCP, 2019, volume 21, issue 20, pages 10238-10243. The thesis author collected the majority of the EPR data, performed all modeling and data analysis, and prepared the manuscript. This work was featured in the 2019 PCCP Hot articles collection and on the back cover of the journal.

3.1 Introduction

The development of spin labeling techniques has enabled EPR spectroscopy to solve two broad classes of biophysical problems. In the first class, spin labeling is applied to a single biomolecular entity to determine structural features such as solvent accessibility, mobility, and secondary structure.[16] The second class of problems involves spin labeling two or more biomolecular bodies or subunits to determine relative subunit conformation,[19, 29, 94-103] protein-protein interactions,[104-109] protein-nucleic acid interactions,[57, 110-112] substrate binding,[64, 113-115] and metal coordination sites.[63, 116-117]

In order to extract such rich information from doubly spin labeled molecules, pulsed EPR distance measurements are often used.[11-12, 48-49, 51, 56, 118-120] Here, we employ a rigid Cu^{2+} labeling technique, the double histidine (dHis) motif, which has been shown to drastically increase the precision of DEER-based distance measurements.[32] Herein, we utilize the dHis motif to determine

the location of a native paramagnetic metal binding site within a protein using a multilateration technique. Because EPR requires an unpaired electron spin, this method is only applicable to bound paramagnetic species. Multilateration methods in three-dimensional space require a minimum of four distance constraints. However, such attempts using nitroxide spin labels have required 5-15 distance constraints for adequate determination.[63-64, 115] Similar nitroxide based methodologies using only four constraints have yielded general information regarding ligand binding locations[117] or subunit conformational changes.[102-103] Using the dHis motif, we show that a highly precise determination can be performed using this minimum four distance constraints.

3.2 Materials and Methods

GB1 mutants were mutated, expressed and purified according to previously published protocols[32]. Samples were prepared in 50 mM NEM buffer at pH 7.4 with 20% v/v glycerol as a cryoprotectant. For EPR experiments 120 μL of protein samples were placed in quartz tubes of I.D. 3 mm, O.D. 4 mm and flash frozen at 80 K for EPR experiments.

All EPR experiments were performed on either a Bruker ElexSys E580 X-band CW/FT Spectrometer with an ER 4118X-MD5 resonator or a Bruker ElexSys E680 X-band CW/FT Spectrometer with an ER 4118X-MD4 resonator. CW experiments were carried out at 80 K with a modulation amplitude of 4 G, a modulation frequency of 100 kHz, a conversion time of 20.48 ms, and a time constant of 10.24 ms. The center field was set at 3100 G with a sweep width of 2000 G over a total of 1024 datapoints. Simulations of the CW spectra were performed with EasySpin[78].

The four-pulse DEER experiment[12] was carried out at 20 K using the pulse sequence $(\pi/2)_{\omega A}$–τ– $(\pi)_{\omega A}$–τ+T– $(\pi)_{\omega B}$–τ_2-T– $(\pi)_{\omega A}$–τ_2–echo. A frequency offset of 150 MHz was used between ω_A and ω_B, with ω_A set to the point of highest echo intensity in the Cu^{2+} spectrum, unless otherwise noted. π/2 and π pulses at ω_A were 16 ns and 32 ns respectively. The π pulse at ω_B was 16 ns. The step size was set between 8-16 ns and incremented over 128 points. Raw DEER data was analyzed using DeerAnalysis2016[4]. The distance distributions obtained from DeerAnalysis2016 were then corrected for the proper g-factor[54].

Circular dichroism was performed using an Olis DSM17 Circular Dichroism Spectrometer. Samples were prepared with 40 μM protein in 20 mM sodium phosphate buffer at pH 7.0. Measurements were performed in 2 mm quartz cells at a temperature of 25 °C from 200 nm to 260 nm with 1 nm increments and a 2 nm bandwidth. Spectra were background corrected with buffer. Melts were collected at 220 nm from 4 °C to 98 °C in 2 °C increments with a 0.5 °C dead band and 2 min equilibration time at each temperature.

Molecular modeling of GB1 and dHis mutants was done using Pymol. Trilateration was performed using MMM[47, 121] and mtsslSuite[122].

3.3 Results and Discussion

DEER-based multilateration of a native paramagnetic metal binding site was performed on the immunoglobulin binding domain of protein G (GB1). GB1 is a stable globular protein[123] and NMR paramagnetic relaxation enhancement studies have indicated the presence of natively bound Cu^{2+} in GB1.[124] Furthermore, GB1 served as the template on which the dHis motif was developed

as a spin labeling method.[32-34] In the original work, the native Cu^{2+} binding was corroborated by EPR data.[32] Additionally, CD data and temperature melts show that the addition of Cu^{2+} to wild type (WT) GB1 does not perturb the protein folding and has a minimal effect on the thermal stability of the protein, shown in Figure 3-1. These factors make GB1 an excellent system for our applications.

We prepared a series of mutants containing single dHis sites at various locations within GB1. As shown previously, incorporation of the dHis motif does not perturb the folding of GB1.[32-34] Due to the minimum requirement of four constraints for multilateration, four dHis sites were chosen; an α-helical site, 28H/32H, and three β-sheet sites, 6H/8H, 15H/17H, and 42H/44H. These locations distribute the dHis sites across the solvent exposed face of GB1 to provide variety of constraints for multilateration. Figure 3-2A shows the relative locations of the dHis sites within the crystal structure of WT GB1 (PDB: 2LGI).[125]

We again confirmed the presence of a native Cu^{2+} binding site within the GB1 protein by performing continuous wave (CW) EPR experiments on WT GB1. Figure 3-2B shows a CW EPR spectrum of WT GB1 in the presence of 10 equivalents of Cu^{2+} (top most spectrum). In these measurements, N-ethylmorpholine (NEM) buffer was used to silence the EPR signal of any Cu^{2+} not bound to the protein.[126] Therefore, the observation of the EPR spectrum seen for WT GB1 in Figure 3-2B can be attributed to Cu^{2+} bound to the protein and confirms the presence of a native binding site. The experimental spectrum was simulated using $g_{\parallel} = 2.227$, $g_{\perp} = 2.058$, $A_{\parallel} = 127$ G, and $A_{\perp} = 10$ G, and is shown as the red line. These parameters are characteristic of Cu^{2+} in an octahedral coordination environment.[83]

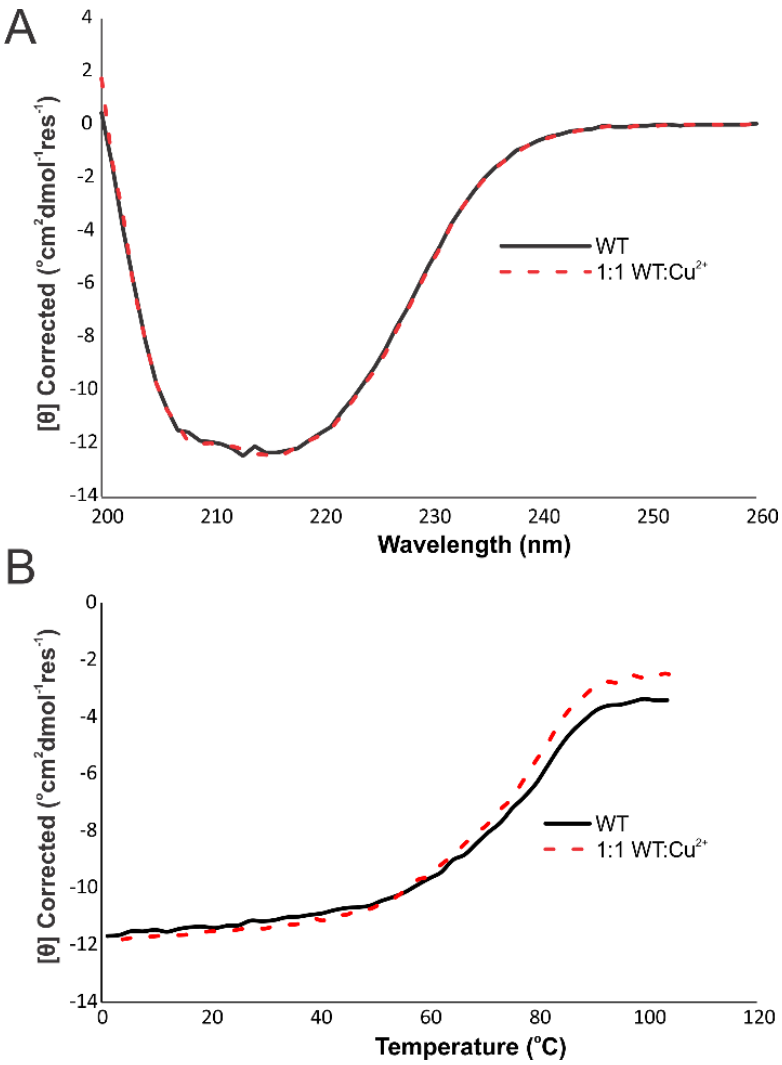

Figure 3-1 A) Circular dichroism (CD) spectra of WT GB1 with (red dashed) and without (black) 1 equivalent of Cu^{2+}. B) Temperature melts of WT GB1 with and without 1 equivalent of Cu^{2+}.

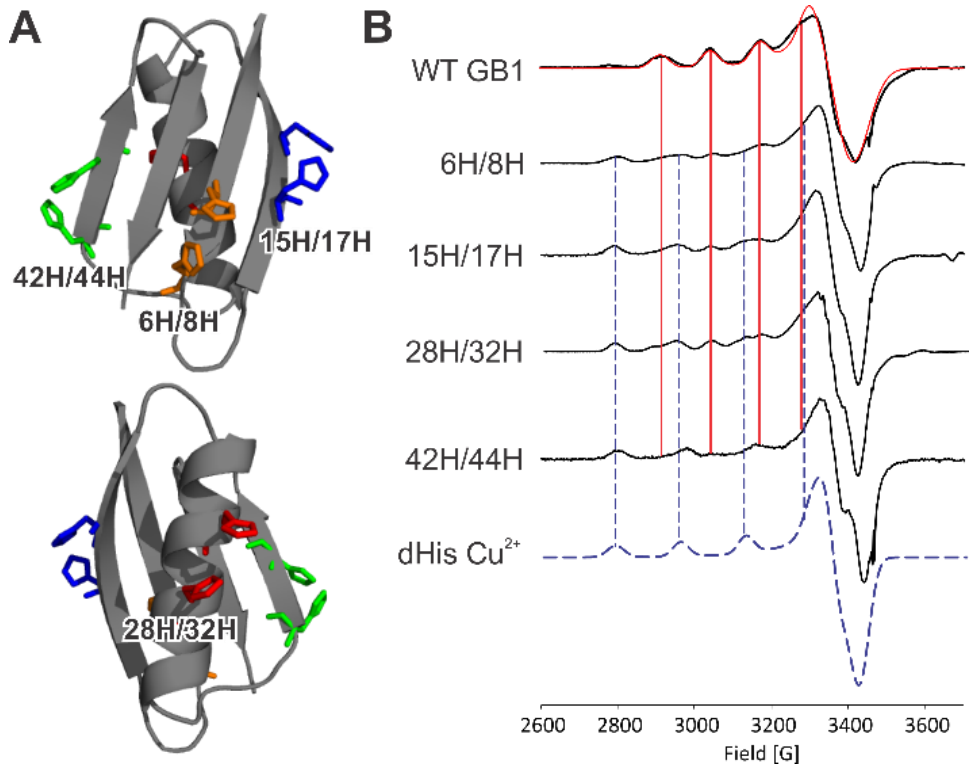

Figure 3-2 A) The crystal structure of GB1 (PDB: 2LGI)[125] with dHis mutation sites depicted as colored residues. Four sites were chosen, 6H/8H (orange), 15H/17H (blue), 28H/32H (red), and 42H/44H (green). B) CW spectra of WT GB1, four dHis GB1 mutants, and component spectra. All spectra were collected at 80 K in 50 mM NEM buffer at pH 7.4 with 10 eq of Cu^{2+}. The dHis GB1 mutants show two components, one corresponding to the native binding site shown in WT GB1 and the other attributed to dHis-bound Cu^{2+}. The $A_{\parallel}$ splittings of each component are traced vertically for reference.

We performed CW EPR experiments on each double mutant to confirm that each dHis site does not perturb metal binding at the native site. Ten equivalents of Cu^{2+} were added to each mutant to ensure that both the dHis site as well as the native binding site are populated. The CW EPR spectra are shown in Figure 3-2B. In each sample, two distinct components were observed. The first component corresponded with the $g_{\parallel}$ and $A_{\parallel}$ parameters of the WT GB1 signal. These $A_{\parallel}$ splittings are shown in Figure 3-2B by the solid red vertical lines that trace the absorbances for each GB1 mutant. The second component is consistent with Cu^{2+} bound to the dHis motif.[32] A simulation of this component is shown as the dashed blue spectrum in Figure 3-2B. The $A_{\parallel}$ splittings of this second component are traced vertically through each GB1 spectrum by a dashed blue line. Therefore, the CW EPR results indicate that the dHis mutations do not perturb native binding and that the added Cu^{2+} ions populate both the native binding site as well as the dHis sites.

We next performed DEER measurements on each dHis double mutant with excess Cu^{2+}. Figure 3-3 shows the background subtracted time domain DEER signals obtained at $g_{\perp}$ for each mutant and their corresponding distance distributions as determined via Tikhonov regularization. The most probable distances and standard deviations were found to be 1.97±0.05 nm (mean±s.d.) for 28H/32H, 1.96±0.15 nm for 6H/8H, 2.31±0.10 nm for 15H/17H, and 2.25±0.08 nm for 42H/44H. Because of the low affinity of Cu^{2+} for the WT site, poor modulation depths and signals were obtained for DEER at $g_{\parallel}$. 28H/32H GB1 provided a signal to noise ratio adequate for a general analysis, and showed dipolar modulations as well as a resultant distance distribution that agrees with the most probable distance found at $g_{\perp}$ within 0.1 nm. Additionally, past work with Cu^{2+}-based DEER[127] and

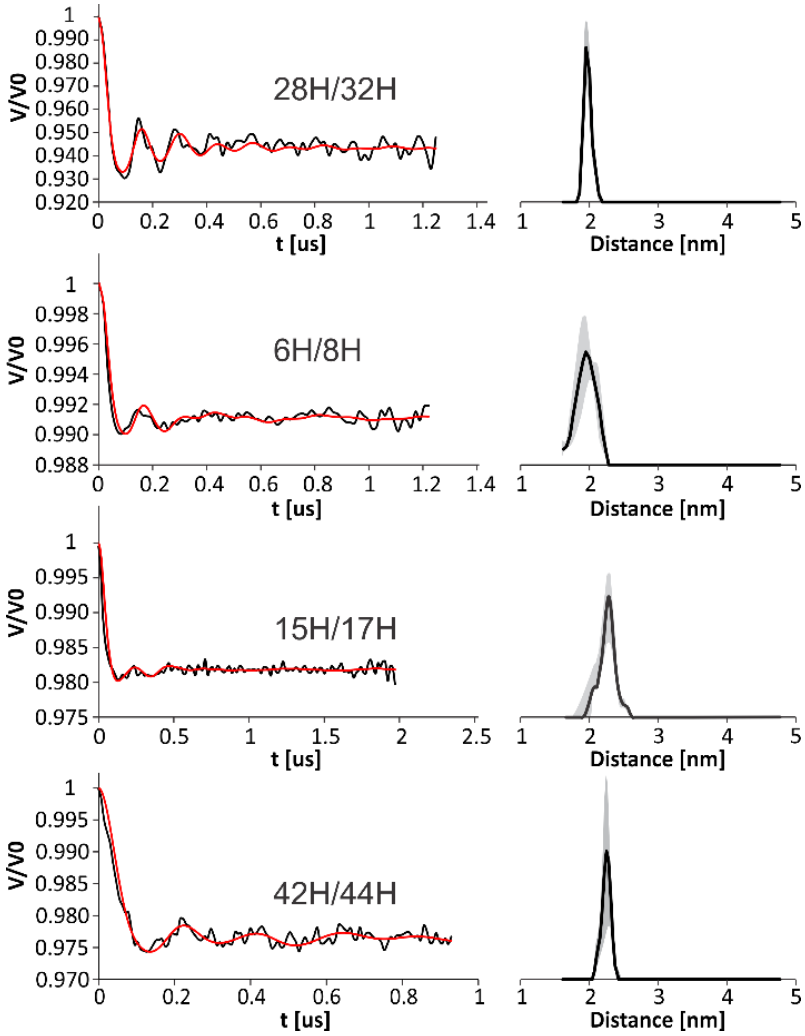

Figure 3-3 Baseline corrected DEER signal (left) and corresponding distance distributions obtained using Tikhonov regularization (right) for each of the four dHis GB1 mutants. The gray shading on the distance distributions represents the uncertainty of the distance distribution.

with rigid dHis motifs in this system[32, 65] and others[60] shows that orientational effects are not typically observed under the experimental conditions used herein. Therefore, we do not expect any orientational effects in this data.

The standard deviations of the distributions are within a range of 0.05-0.15 nm. These standard deviations are notably smaller than those of comparable studies using nitroxide spin labels. For nitroxide-based measurements performed to determine the Cu^{2+} binding center of azurin, standard deviations ranged between 0.1-0.32 nm.[63] Likewise, in using nitroxides to determine the Cu^{2+} binding in EcoRI, DEER distributions reported standard deviations between 0.2-0.3 nm.[116] It should be noted that the standard deviations are highly system dependent, taking into account the site of mutation and the spin label employed. However, as we have shown previously, the dHis motif is capable of greatly decreasing the standard deviation of DEER distance distributions within the same system at equivalent sites compared to a common nitroxide label.[32] Therefore, we believe a broad comparison of our results to similar work is apt.

The distance distributions derived from DEER were then used as constraints to establish the location of the native metal binding site. This was achieved using the Multiscale Modeling of Macromolecules (MMM).[47] MMM is capable of introducing the dHis Cu^{2+} motif to a given crystal structure *in silico.*[121] Using the WT GB1 crystal structure (PDB: 2LGI), we added the four dHis-bound Cu^{2+} ions in MMM, as shown as dark blue spheres in Figure 3-4A. The mean distances and standard deviations determined by DEER were input for each corresponding dHis site. With the appropriate constraints, MMM is able to perform a multilateration to locate the native metal binding site by calculating constraint overlap. The results of this multilateration are shown in Figure 3-6A. The calculated location of the natively bound Cu^{2+} is shown as a red ellipsoid, with

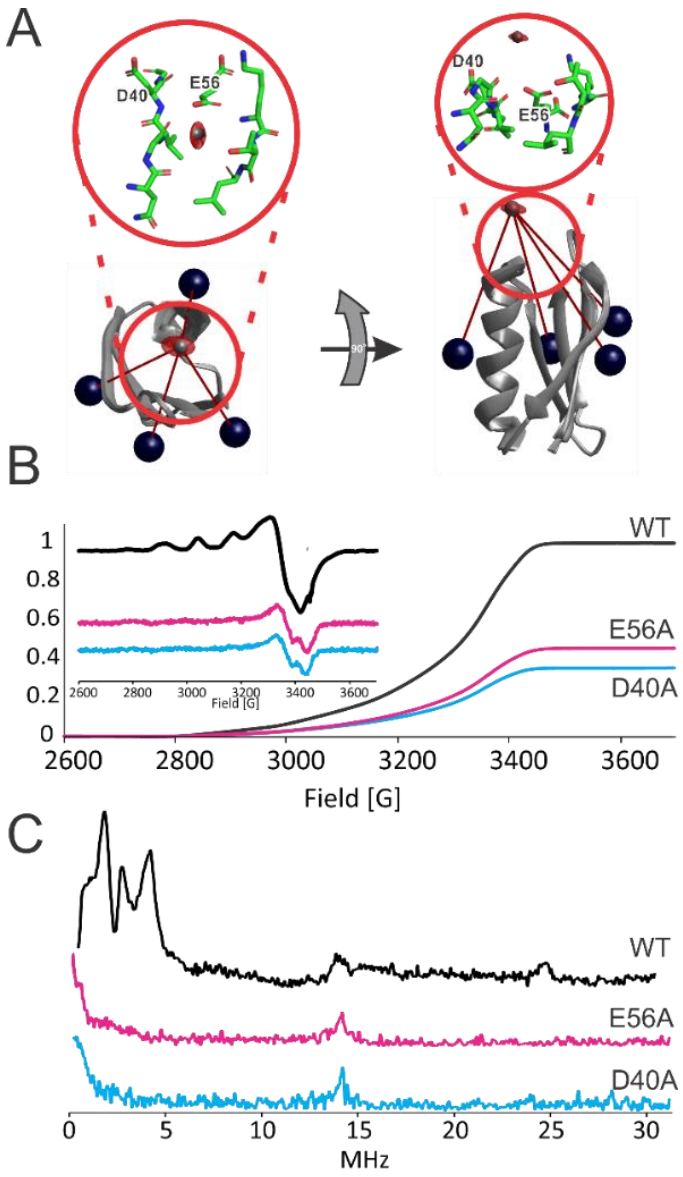

Figure 3-4 A) Multilateration results using experimental DEER constraints with MMM. The GB1 crystal structure is shown in gray, with the dark blue spheres representing the Cu^{2+} bound to the dHis sites. The circled insets show the local coordination environment of the target of the multilateration. B) Double integrated intensity of WT GB1 (black), E56A GB1 (pink), D40A GB1 (blue) with 10 equivalents Cu^{2+}. The inset shows the first derivative CW EPR spectra. The intensities were normalized to the maximum intensity of the WT sample. C) ESEEM spectra for the series of GB1 samples. All samples were in 50 mM NEM buffer.

the center of this area indicated as a grey sphere. Notably, these results were validated by performing the multilateration using mtsslTrilaterate[122] as shown in Figure 3-5. The mtsslTrilaterate results place the native Cu^{2+} in the same vicinity as that found via MMM.

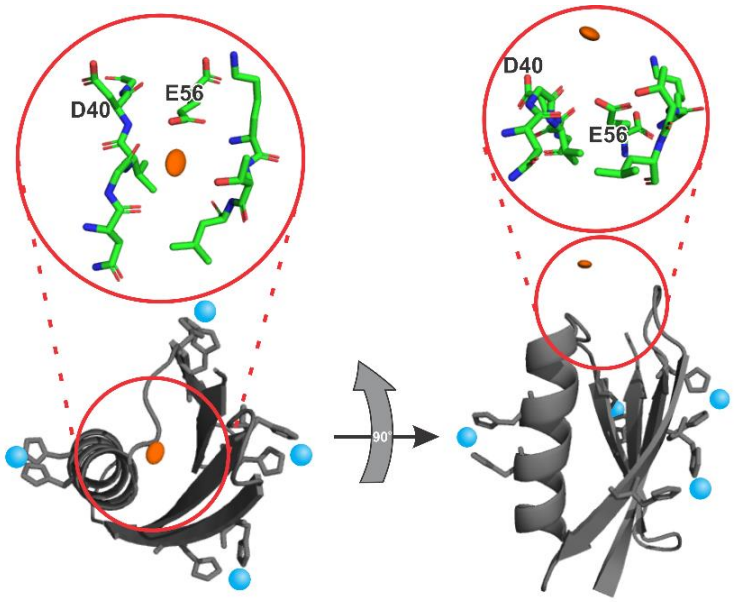

Figure 3-5 Trilateration of the WT GB1 native binding site performed using mtsslSuite[122]. The target site is located in proximity to the same residues of that found via MMM[47, 121].

The results of this multilateration are noteworthy, as an unambiguous target location was achieved using only the minimum four distance constraints. The multilateration yielded a target ellipsoid with dimensions approximately 1.4 Å x 1.8 Å x 1 Å. For previous work using nitroxide labels, six measurements were necessary to achieve an error in the measurement of 2.6 Å, and an error of 4.4 Å when using the minimum of four constraints.[63] Other comparable works include the localization of the Ruboxyl binding site in NorM using five constraints,[115] and a multilateration of bound Cu^{2+} in the octarepeat Cu^{2+}-binding domain of prion protein using four distance

constraints,[117] both of which provided a general approximation of the bound ligand. The precision of our results are more comparable with the location of a lipid within the lipoxygenase active site, which yielded a target ellipsoid of dimensions 1.2 Å x 2.3 Å x 3.0 Å using fifteen distance constraints.[64] Using the rigid dHis motif, we showed improved precision with an approximately fourfold decrease in the number of measurements. We note that a trilateration on GB1 using nitroxide labels may provide the most direct and quantitative comparison for our results. Our comparisons to similar work in the context of the general increase in precision of the dHis motif over nitroxide labels emphasizes the broad-spanning application of our presented method.

The GB1 crystal structure (PDB: 2LGI) then provides insight into the context of the native binding site. In the circled insets in Figure 3-4A, we have shown the stick representation of the amino acid residues in the general proximity of the multilateration target. Notably, within this region are the aspartic and glutamic acid residues D40 and E56, respectively. These specific amino acids contain a negatively charged carboxylate group at physiological pH which is known to participate in metal ion coordination in metalloproteins.[128] NMR relaxation enhancement studies on GB1 have indicated D40 as one of the residues involved in native binding sites.[124] Additionally, E56 is the terminal residue of GB1 and thus the carboxylate group of the C-terminus may play a role in the native binding. Based on their proximity to the multilateration target and the corroboration of NMR data, it is likely that these residues are involved in the native Cu^{2+} binding site in GB1.

The involvement of these residues was confirmed performing D40A and E56A mutations. Alanine was chosen as it does not contain groups that coordinate with Cu^{2+}. Cu^{2+} was added to each mutant and CW EPR spectra were collected and doubly integrated in order to compare the amount of bound Cu^{2+} relative to WT GB1 (shown in Figure 3-4B). These experiments were again

performed in NEM buffer to silence free Cu^{2+}. The single mutants E56A and D40A showed reduction of natively bound Cu^{2+} by 55% and 65%, respectively. Because this particular Cu^{2+} binding site involves the C-terminal residue, the remaining presence of Cu^{2+} may be due to a continuing coordination to the C-terminus carboxylate, which will be present regardless of the amino acid residue. In previous work we have shown that a Cu^{2+} chelator such as iminodiacetic acid or nitrilotriacetic acid effectively prevents nonspecific binding of Cu^{2+} to native sites.[32-34] Therefore, we do not foresee the presence of C-terminus carboxylate groups posing a problem at large regarding Cu^{2+} distance measurements. Circular dichroism results indicate that these mutations do cause some perturbation to the folding of the protein, shown in Figure 3-6. The E56A mutation shows an increase in ellipticity around 215 nm, indicative of a loss of β-sheetedness. E56 is located at the end of GB1's fourth β-sheet, and the mutation may be disordering it. As well, the D40A CD spectrum shows a decrease in the region 210-220 compared to WT, which is associated with α-helicity. D40A is positioned three residues outside of GB1's α-helix, and the mutation may be promoting some elongation of that feature. Regardless, the perturbation of the proposed binding site, through removal of carboxylate groups or potential changes in protein secondary structure, was achieved, and correlates with a decrease in native Cu^{2+} binding.

Finally, we performed electron spin echo envelope modulation (ESEEM) on WT, D40A, and E56A GB1, as shown in Figure 3-4C. ESEEM is a pulsed EPR technique that is sensitive to nuclear spins within 3-10 Å of the unpaired electron. The ESEEM spectrum for Cu^{2+} bound to WT GB1 exhibits a signal characteristic of the amide nitrogen of the peptide backbone[129-130], which is consistent with coordination of Cu^{2+} to the functional group of an amino acid. These features are noticeably absent from the GB1 alanine mutants. This absence indicates that the alanine mutations are in fact perturbing the coordination environment of the Cu^{2+} ions within the protein. The peak

around 14 MHz, which is consistent for all samples, is due to surrounding hydrogens. The ESEEM and CW data taken together support the results of our multilateration and the supposition that residues D40 and E56 are involved in the native binding of Cu^{2+}.

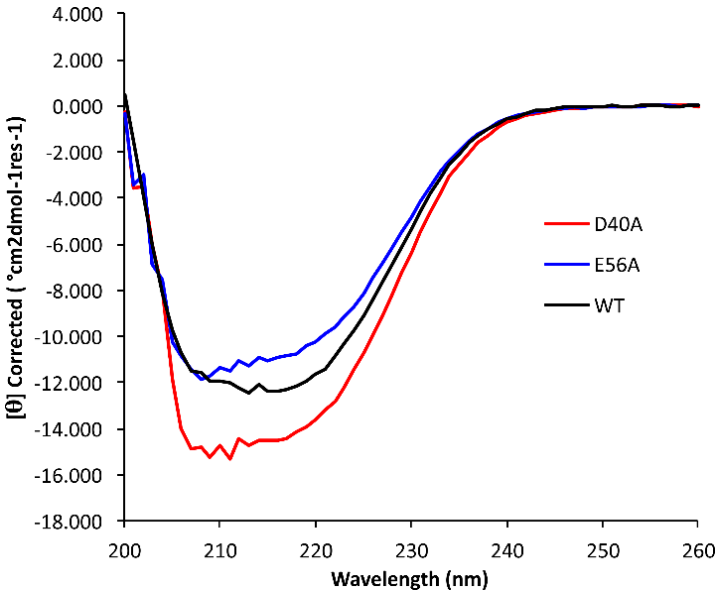

Figure 3-6 Circular Dichroism spectra of WT, D40A, and E56A GB1. The CD signature of the D40A and E56A mutants show some difference from the WT spectrum, indicating that the folding of GB1 is perturbed to a degree by the alanine mutations.

3.4 Conclusion

In summary, in this work we demonstrate the use of the dHis Cu^{2+} binding motif for the multilateration of a native paramagnetic metal binding site within a protein. Using this rigid spin labeling technique, precise multilateration results were obtained using the minimum number of distance constraints necessary for a three-dimensional system. The calculated multilateration

results were confirmed by mutating the residues D40 and E56 to alanines, effectively removing their ability to coordinate Cu^{2+} ions. These mutants showed a significant decrease in Cu^{2+} binding. This work shows a distinct advantage of the dHis Cu^{2+} motif for structural assessment over nitroxide-based spin labels. This methodology is of interest to a wide class of metalloproteins. In these proteins the metal ions can act as agonists to control protein structural and conformational shifts, regulate the catalysis of enzymes, and facilitate their movement throughout a living body via transport proteins. Therefore, the precise determination of the location of these metal binding sites is important for our understanding of the protein's mechanism and function. Such dHis based approaches expand its current purview[60, 65] into a class of problems relating to protein-protein docking, protein-nucleic acid interactions, and substrate binding.

3.5 Acknowledgements

This data was supported by the National Science Foundation (NSF MCB-1613007). The EPR spectrometer was supported by the National Science Foundation (NSF MRI-1725678).

4.0 On the Use of Q-Band DEER to Resolve the Relative Orientations of Two Double Histidine Bound Cu^{2+}-Ions in a Protein

This work, written in collaboration with Kalina Ranguelova, Shreya Ghosh, Ralph Weber, and Sunil Saxena, was published in J. Phys. Chem. B. in 2019, volume 122, issue 47, pages 10669-10677. The thesis author performed all analysis and simulation of EPR data, molecular modeling, and prepared the manuscript. This work was featured on a supplementary cover of the journal.

4.1 Introduction

Distance measurements by pulsed Electron Paramagnetic Resonance (EPR) have become important techniques for the determination of macromolecular structures and dynamics.[90, 131] These pulsed EPR techniques isolate the weak dipolar coupling between two unpaired electrons in a macromolecule and extract a distance in the range of 2-16 nm.[11-12, 48-49, 51, 56-58, 90, 120, 131-133] Such long-range distance constraints are useful to characterize the structure and flexibility of the macromolecule. Specifically, one exciting application of these EPR distance measurements is the elucidation of induced conformational changes in biomolecules.[90, 131, 134-140] Such EPR techniques are particularly advantageous for biomolecules that are difficult to crystallize or too large for NMR structural determination. Therefore, pulsed EPR can provide unprecedented insight into the structure and conformations of important biomolecules that would be inaccessible by other means, leading to a greater understanding of the mechanisms of biological processes.

The scope of pulsed EPR methodology has been greatly enhanced by site-directed spin labeling, which typically uses nitroxide based spin labels.[15-16, 141] Common nitroxide spin labels are versatile,[15-16, 141-144] but can be limited in practice by the long, flexible side chain required to attach the paramagnetic head group to the macromolecular backbone.[145-146] This inherent flexibility translates to broad distance distributions which can lead to uncertainty in the interpretation of the EPR data in terms of protein structure. Efforts to solve this problem by employing rigid nitroxide labels have met with some success, although these labels are often bulky and far-removed from the protein backbone.[142, 147-150]

The demand for alternative spin labels has led to the development of paramagnetic metal based distance methods and spin labeling approaches.[151-163] Cu^{2+} specifically has emerged as a simple, site-specific paramagnetic probe that can be incorporated into proteins and DNA to provide precise, accurate distance measurements indicative of the protein or DNA backbone.[32, 34, 164] One such Cu^{2+} labeling technique which has shown great promise is the Double Histidine (dHis) motif.[32] The dHis motif involves strategic placement of two histidine residues within a protein. For α-helical sites, an i and i+4 arrangement of two histidine residues allows for simultaneous cis-coordination of the Cu^{2+}, while in β-sheets, an i and i+2 arrangement is necessary to place the two histidine on the same face of the sheet for metal binding. This motif rigidly binds Cu^{2+} complexed with ligands and can provide distance distributions up to five times narrower than common nitroxide spin labels.[32] This drastic increase in precision is invaluable as initial results suggest that the dHis motif produces data dominated by backbone fluctuation rather than sidechain mobility. The benefits of the dHis motif were evidenced recently when both nitroxide and dHis-Cu^{2+} distance measurements were applied to the glutathione S-transferase system in order to

characterize its conformational equilibrium.[60] The dHis motif provided significantly enhanced resolution over the nitroxide spin labels in this system.[60]

However, even with the added precision that dHis-Cu^{2+} motif provides, there may be multiple possible conformational states that satisfy a given distance constraint. Therefore, additional structural information may be useful for full elucidation of a given conformation. Orientationally selective DEER is one such technique that provides complementary data on the relative orientation of the two spin labels. Orientational selectivity can occur because pulse lengths typically applied in pulsed EPR can only excite a small portion of the total spectrum. In systems containing large g-anisotropies and resolved hyperfine anisotropy, excitation of a small portion of the total spectrum can select only a small subset of all possible molecular orientations. At X-band frequencies (9.5 GHz), the nitroxide and Cu^{2+} EPR spectra have large hyperfine splittings relative to the features due to g-anisotropy. In this case, the large hyperfine contribution will overlap and mix different features of the spectra, allowing the excitation of multiple orientations within a small spectral region. Orientational selectivity can be further mitigated by using flexible spin labels such that the excited orientations are effectively randomized. This effect is facilitated in nitroxides by their flexible tether to the molecule. In Cu^{2+} based systems, orientational flexibility of the Cu^{2+} coordination environment achieves the same effect.[127] Therefore, orientational selectivity is uncommon in nitroxide and Cu^{2+} based systems at X-band.

Despite these factors, certain systems exhibit orientational selectivity at X-band. DEER has been performed on several of these specific nitroxide radical pairs[165-169] and Cu^{2+}-nitroxide systems[170-171] to determine the relative orientations of the spin labels. Such an analysis was also applied to two Cu^{2+} centers within a protein in endogenous binding sites.[54] These methods benefit from higher frequency EPR, such as Q-band (35 GHz) and W-band (95 GHz), becoming more

accessible. Their increased resolution can enhance orientational selectivity and lead to easier disentanglement of spin label orientations.[172-179] Recently, Q-band EPR was used to assess the general orientations of Cu^{2+} centers in DNA G-quadruplexes.[180] Additionally, rigid spin labels have been employed for similar studies.[169, 181] Despite such efforts, the current state of orientational selectivity analysis using rigid Cu^{2+} labels at Q-band is limited, and it is therefore of interest to refine this method and demonstrate its applicability to a wider variety of biomolecules.

Herein we show that Q-band orientationally selective DEER using the dHis motif provides a simple, reliable method of determining Cu^{2+} label orientation within a macromolecule. We demonstrate that Q-band DEER is sensitive to the relative orientations of the Cu^{2+} within the dHis motif. Additionally, we show that the relative orientations can be determined through simulation of the orientationally selective DEER data. Lastly, we show that the relative orientations determined via simulation agree with an intuitive visual analysis of the protein crystal structure.

4.2 Materials and Methods

For our experiments we used a 6H/8H/28H/32H mutant of the immunoglobulin binding domain of protein G, called GB1. The protein expression and purification of the GB1 tetramutant were performed as described elsewhere.[32, 34] Cu^{2+} was complexed with nitrilotriacetic acid (NTA) prior to its introduction to the protein. All EPR samples were prepared in 50 mM N-ethylmorpholine (NEM) buffer at pH 7.4 with 20% glycerol as a cryoprotectant with a ratio of GB1:Cu^{2+}:NTA of 1:1.5:1.5.

DEER data was acquired with a Bruker E680 spectrometer equipped with a 150 W amplifier and an ER5106 QT2 resonator. The sample temperature of 20 K was maintained using a Bruker B8692690 cryogen free cryostat. The resonator was overcoupled to a bandwidth of 250 MHz. The pump microwave frequency was set to the center of the resonator dip to optimize modulation depth and the observer frequency was set 100 MHz higher in frequency. π pulse lengths of 28 and 50 ns were attained for pump and observer frequencies respectively. To increase the modulation depth an 80 ns chirp pulse with frequency range -150 to -50 MHz relative to the observer frequency was used. A four pulse DEER with a 16 step phase cycle was performed with the sequence $(\pi/2)_{\omega A}$–τ– $(\pi)_{\omega A}$–τ+T– $(\pi)_{\omega B}$–τ_2-T– $(\pi)_{\omega A}$–τ_2–echo.[182] τ was set to 200 ns and data was collected over a time interval of 1.3 μs with a step size of 10 ns resulting in a 128 point data set. The shot repetition was 61.2 μs. Including the 16 step phase cycle, 409,600 averages were acquired. In order to acquire the orientation selection data, a pulse program was written to acquire DEER spectra from 11020 to 11774 G at 17 magnetic field values. To determine the distance distribution these signals were summed and analyzed using the DeerAnalysis software package.[4]

Simulations of the individual time domain DEER signal were performed using methodology developed previously by the group, as detailed elsewhere.[127]

Briefly, The DEER signal can be expressed as[127, 183-184]

$$V(t) = 1 - \iint P(r)\left(\lambda - \lambda\cos\left[\frac{k}{r^3}(1 - 3\cos^2\theta)t\right]\right)\xi(\theta)d\theta dr \qquad (4\text{-}1)$$

where P(r) is the distance distribution, θ is the angle between the interspin vector and the applied magnetic field, k is a constant containing the product of the two spins' g values, r is the distance between the two spins, and λ is the modulation depth. ξ(θ) is the geometrical factor, given by[127, 184]

$$\xi(\theta) = \frac{1}{2}\sum_{m_{I1}m_{I2}}\langle {k_{xa}}^3 {k_{xb}}^2 \sin\varphi_{1a}(1-\cos\varphi_{2a})(1-\cos\varphi_{3b}) +$$

$${k_{xb}}^3 {k_{xa}}^2 \sin\varphi_{1b}(1-\cos\varphi_{2b})(1-\cos\varphi_{3a})\rangle_{\phi,\delta\omega1,\delta\omega2} \quad (4\text{-}2)$$

where m_{Ii} is the nuclear quantum number of spin *I*, φ_{ia} is the flip angle of the first spin by the *i*th pulse, φ_{ib} is the flip angle of the second spin by the *i*th pulse, $\delta\omega1$ is the inhomogeneous broadening of the observer or pump pulses, k_{xa} is the ratio of the resonance frequency of the spins excited by the observer pulses to the observer frequency, and k_{xb} is the ratio of the resonance frequency of the spins excited by the pump pulse to the pump frequency.

The geometrical factor depends implicitly on the relative orientations of two principal axis systems of the g-tensors of the two Cu^{2+} spins. The relative orientations are described by the angles χ, γ, and η[127] (cf. Figure 1A). χ is the angle between spin A's $g_{\parallel}$ axis and the interspin vector, r. γ is the angle between the $g_{\parallel}$ axes of spin A and B. η is the angle between the $g_{\perp}$ axes of spin A and B. Each of these angles has an associated standard deviation, σ. To limit the number of variables, a single σ was used for all three angles. All other variables were set in accordance with the above experimental parameters.

Simulated DEER signals were normalized and adjusted to match the modulation depth of the experimental signal. Molecular modeling was done using Pymol. Visualization of the Cu^{2+} spin label was achieved using Multiscale Modeling of Macromolecules (MMM).[47, 121]

4.3 Results and Discussion

In this work we examine the potential of Q-band to resolve the relative orientation between two units on a protein. We have shown previously that, in theory, orientational selectivity for

Cu^{2+}-Cu^{2+} DEER measurements is a possibility, however in practice, it is not commonly observed at X-band.[32, 53, 116, 133] Orientational selectivity can be reduced in Cu^{2+}-DEER because of a distribution in relative orientations of the g-tensor[116, 127, 133] and due to specific relative orientations of the g-tensors.[53, 185] Similarly, at X-band orientational effects on dHis based distances have not been observed within signal to noise considerations so far.[32-34, 60]

Q-band orientationally selective DEER can be a powerful probe of spin label orientation and molecular conformation. The relative orientations of two coupled spins are shown in Figure 4-1A, along with the angles used to relate the orientations as described previously. Figure 4-1B shows two conformations of the same macromolecule, with a dHis Cu^{2+}-NTA site on each subunit. We assume that both conformations have the same distance between Cu^{2+} centers, r, and standard deviation, δr. However, the relative orientations of the Cu^{2+} centers are different, where $g_{\perp}$ is perpendicular to the interspin vector, r, for conformation A and $g_{\parallel}$ is parallel to r for conformation B. At the magnetic field corresponding to $g_{\perp}$, different θ will be probed, where θ is the angle between r and the applied magnetic field, B_0 as shown in Figure 4-1B. The excitation probability at this magnetic field for both X and Q-band is shown in Figure 4-1C. These probabilities were calculated as the geometrical factor, $\xi(\theta)$[127, 184] (cf. Equation 4-2). The difference in θ excited can be shown by the probability curves in Figure 4-1C. These curves depict the probability distribution of θ, P_θ, that is excited by a typical pump pulse used in DEER. The black lines in Figure 4-1C show the probability curve when all molecular orientations are excited, or the ideal case for DEER. The left and right frames show the probability curves at Q-band and X-band, respectively, for conformations A and B. For the parameters given, $\chi=90^o$, $\gamma=0^o$, and $\eta=0^o$ and $\sigma=10^o$ for conformation A, and $\chi=0^o$, $\gamma=0^o$, and $\eta=0^o$ and $\sigma=10^o$ for conformation B. With $\sigma=10^o$ orientational effects are washed out at X-band.[127] The $\xi(\theta)$ are different at Q versus X-band. At Q-band, we can

see that the θ probed varies greatly between conformations A and B, whereas at X-band, orientational selectivity is washed out and the difference between the two excitations is negligible. Figure 4-1D shows the DEER signals that result from each excitation. Again, the DEER signals produced at Q-band are distinctly different from each other, whereas the X-band data shows identical modulations. Under such conditions of a large orientational flexibility (i.e. $\sigma=10^{o}$) at X-band the two conformations cannot be distinguished by DEER. However, using Q-band, orientational selectivity is easily manifested in DEER, allowing the relative orientations of the spin labels to be determined. Therefore, determination of spin label orientation may enable new avenues of structural and conformational characterization of proteins and macromolecules. It should be noted that Figure 4-1 presents the simplest case, with colinear $g_{\parallel}$ axes. The principles shown in Figure 4-1 are also applicable to systems with orthogonal g-tensors, and both modulation frequency and modulation depth may be indicators of orientational selectivity.

To explore this potential, we chose the B1 immunoglobulin binding domain of protein G (GB1) modified with two dHis motifs at sites 6H/8H and 28H/32H for our orientational selectivity analysis.[32] GB1 is a simple model system that is thermally stable,[123, 186] has been extensively characterized by EPR and other methods,[187-195] and served as the template on which the dHis motif was designed,[32-34] making it ideal for our purposes. The rigidity of the dHis motif provides well defined, unambiguous dipolar modulations in the DEER experiment[32] that aid in clarifying the orientational effects. The Cu^{2+} used in this work is chelated with the NTA ligand, which has been shown to prevent non-specific binding of Cu^{2+} and increases binding affinity to α-helical sites compared to similar ligands.[34]

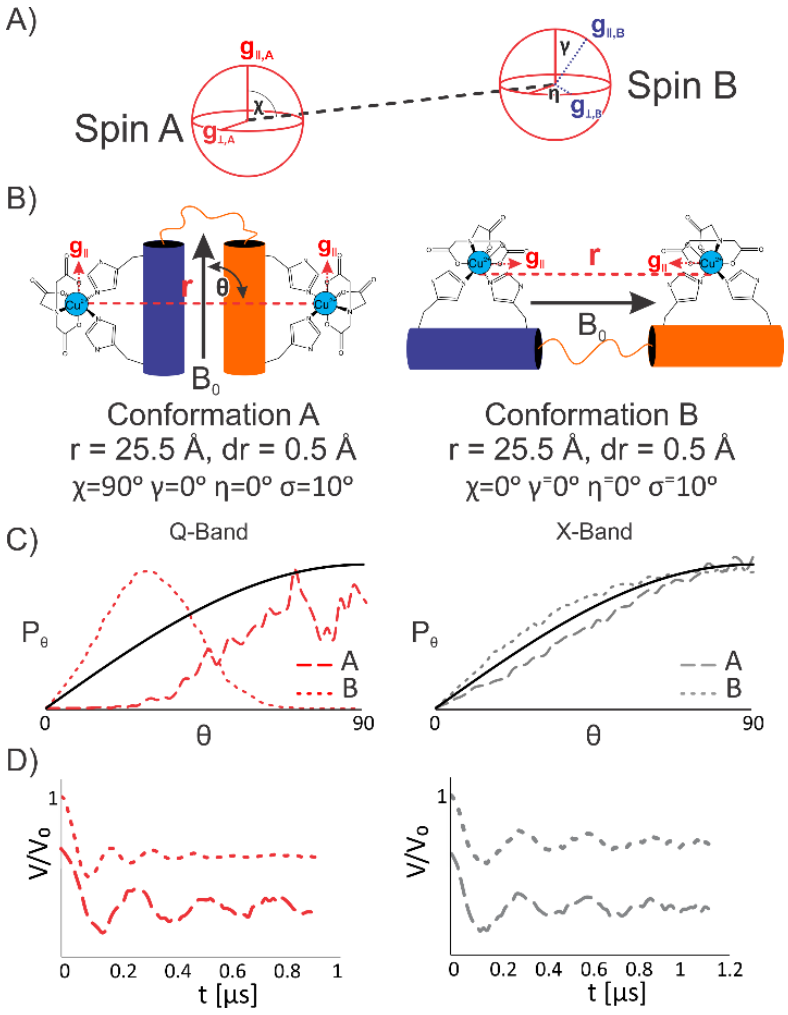

Figure 4-1 An overview of orientational selectivity and its applications in determining protein structure and conformation. A) A brief definition of the angles used to relate two coupled spins in a macromolecule. B) Two conformations of the same protein, with two dHis mutations. The distances and distributions remain identical, but the orientation of the spin labels is changed. C) The curves indicate the probability of exciting a certain θ in the DEER experiment. This curve and simulations were performed with a sufficient orientational distribution such that orientation effects are washed out at X-band, consistent with many dHis based distances observed so far (see text). The curves are indicative of an excitation at $g_{\parallel}$. The black line shows the equal excitation of all orientations. Dashed lines indicate Conformation A, and dotted lines indicate Conformation B at Q-band and X-band from left to right. D) The DEER signals obtained at each magnetic field following the same line conventions as 2B.

The orientation of such a Cu^{2+} in the dHis motif is defined by the coordinating ligands. Cu^{2+} most commonly exhibits an octahedral coordination geometry, with four equatorial ligands defining its $g_{\perp}$ plane and two axial ligands defining the $g_{\parallel}$ axis. For Cu^{2+}-NTA in the dHis motif, the coordination geometry is shown in Figure 4-2A. The imidazole nitrogens of the histidine residues coordinate to the Cu^{2+} in two equatorial positions. Therefore, we can estimate the $g_{\perp}$ plane as containing the Cu^{2+} and the coordinating nitrogens. $g_{\parallel}$ is along the axially coordinated oxygen atoms from the NTA chelator and points perpendicular to the $g_{\perp}$ plane. In this way, we can define the orientations of the Cu^{2+} spin labels within the overall molecular frame. By determining the orientation of both spin labels with respect to each other, we can gain insight on the overall structure and conformation of the molecule.

Figure 4-2B shows a crystal structure of 6H/8H/28H/32H GB1 (PDB: 4WH4).[32] This crystal structure was determined without Cu^{2+}, therefore Cu^{2+} ions were placed in the structure *in silico* according to previous methods[32]. Using the definitions above, we have superimposed the proposed $g_{\parallel}$ and $g_{\perp}$ axes over each Cu^{2+} ion. To reiterate, we can then define a set of angles to relate the two axis systems; χ, γ, and η.[127] χ is the angle between spin A's $g_{\parallel}$ axis and the interspin vector, r. γ is the angle between the $g_{\parallel}$ axes of spin A and B. η is the angle between the $g_{\perp}$ axes of spin A and B. Another angle, θ, is the angle between the applied magnetic field vector and the interspin vector, r. θ is not necessary to define the relative orientations of the spin labels, but describes the overall molecular orientation. With the molecular model defined, pulsed EPR can then be used to extract the relative orientations of the Cu^{2+} labels.

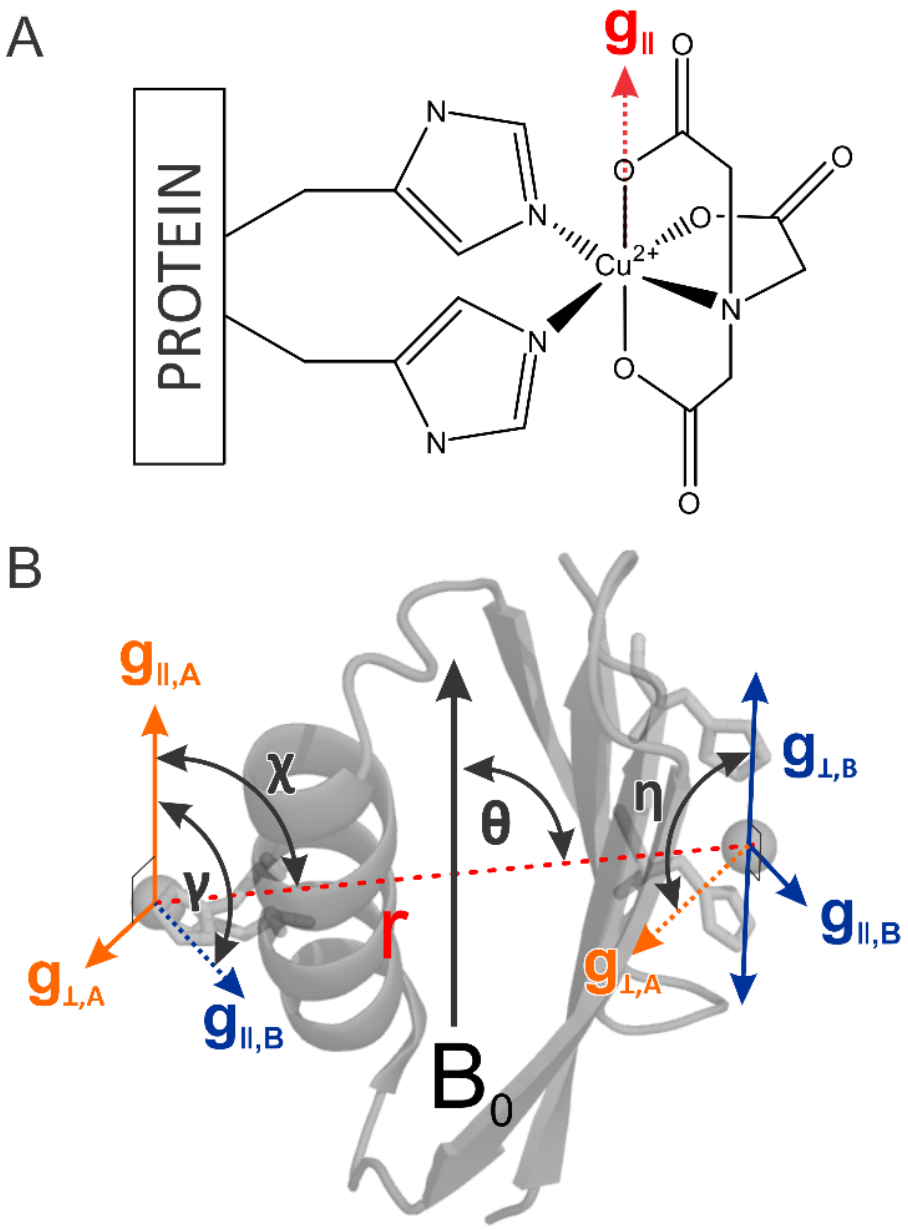

Figure 4-2 A) The proposed coordination environment of Cu^{2+} chelated with NTA within the dHis motif. The imidazole nitrogens are expected to bind in two equatorial positions, allowing for simple determination of the Cu^{2+} orientation based on the dHis position. B) The molecular model used in the DEER simulations. The principal axis systems for the g-tensors of spin A (orange) and B (blue) are shown overlaid on the crystal structure of 6H/8H/28H/32H GB1 (PDB: 4WH4). The relative orientations of these principal axis systems are defined relative to each other based on three angles: χ, γ, and η.

To this end we first collected DEER data at multiple magnetic fields between $g_{\parallel}$ and $g_{\perp}$ at Q-band frequencies to probe the extent of orientational selectivity in the system. Figure 4-3A shows the field swept spectrum and the magnetic fields at which DEER was performed as indicated on the spectrum. A total of 17 DEER signals were collected, ranging from 11774 G to 11020 G to obtain a sufficiently robust set of data. The corresponding DEER signals are shown in Figure 4-3B. Interestingly, the modulation frequency decreases as the magnetic field decreases, clearly demonstrating the orientational selectivity effect at Q-band. The modulation depth of the DEER signal decreases at lower magnetic fields. This effect is due in part to the intensity of the absorption spectrum decreasing along with the magnetic field, and also due to orientational selectivity.

We then summed the raw Q-band DEER signals to compare with previously collected X-band data. In previously published work, the system did not exhibit orientational selectivity at X-band and therefore one DEER signal collected at the $g_{\perp}$ field position sufficed.[32, 34] This supposition was confirmed experimentally, in which DEER was performed on the sample at X-band at $g_{\perp}$ and $g_{\parallel}$ which produced identical distance distributions, shown in Figure 4-4. Figure 4-3C shows DEER signals collected at X-band and the summed Q-band. Clearly, the modulation frequency is similar between the two runs. The resultant distance distributions as analyzed by Tikhonov Regularization[196] are shown in Figure 4-3D. The most probable distances of each distribution are 2.44 nm for X-band and 2.40 nm for Q-band, which agree well within the uncertainty of the measurement as shown by the validation in Figure 4-3D. Furthermore, the distance distributions inform us of the distance and the standard deviation to be used for simulation.

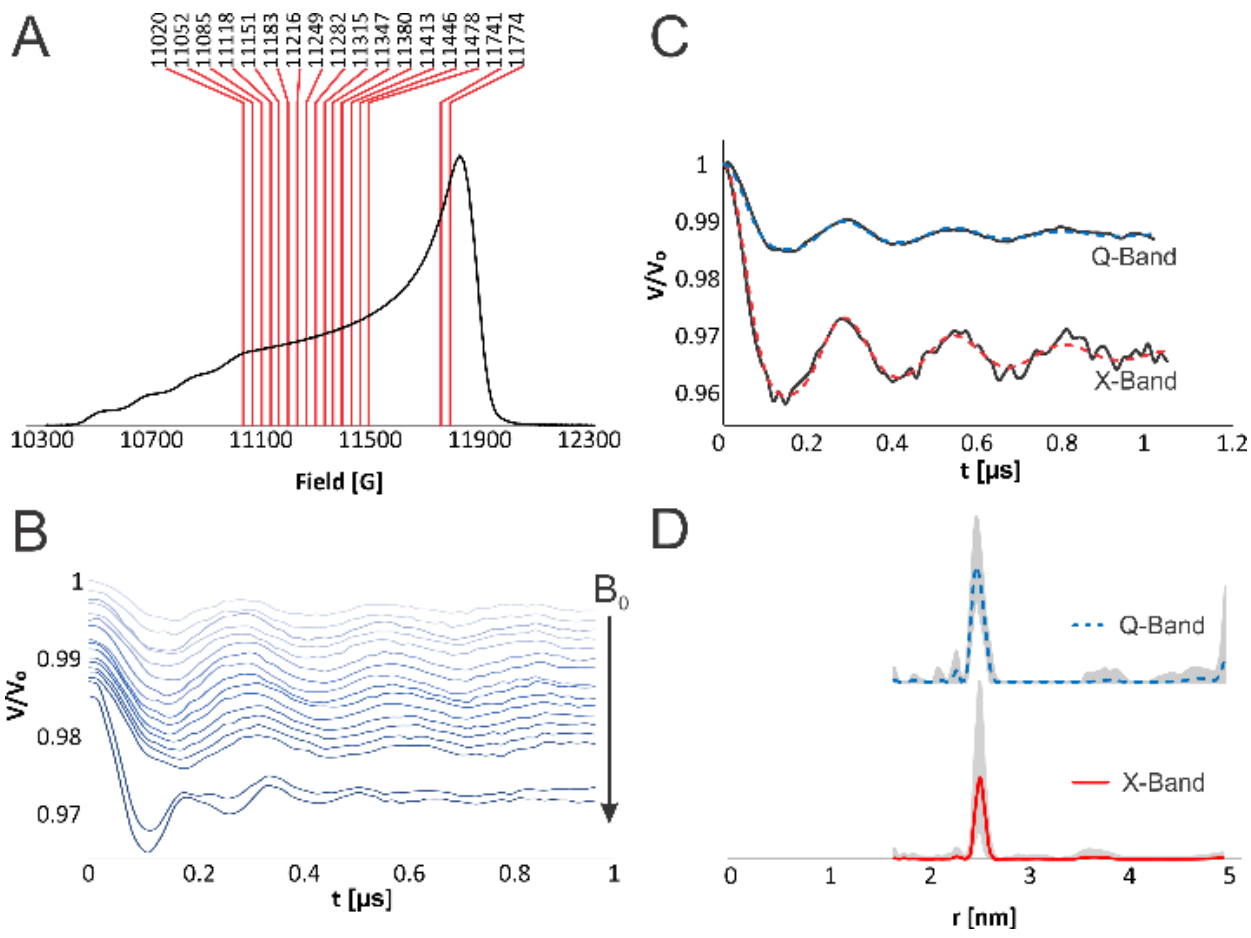

Figure 4-3 A) Field swept Cu^{2+} spectrum. The red lines indicate field positions at which DEER was performed. B) Experimental DEER data as a function of magnetic field to demonstrate the effects of orientational selectivity. C) The summation of the Q-band DEER signals as compared with the X-band DEER, which serves as a validation of the Q-band data. D) Distance distributions via Tikhonov Regularization of the summed Q-band data compared to the X-band data. The gray shading indicates the uncertainty in the distance analysis.

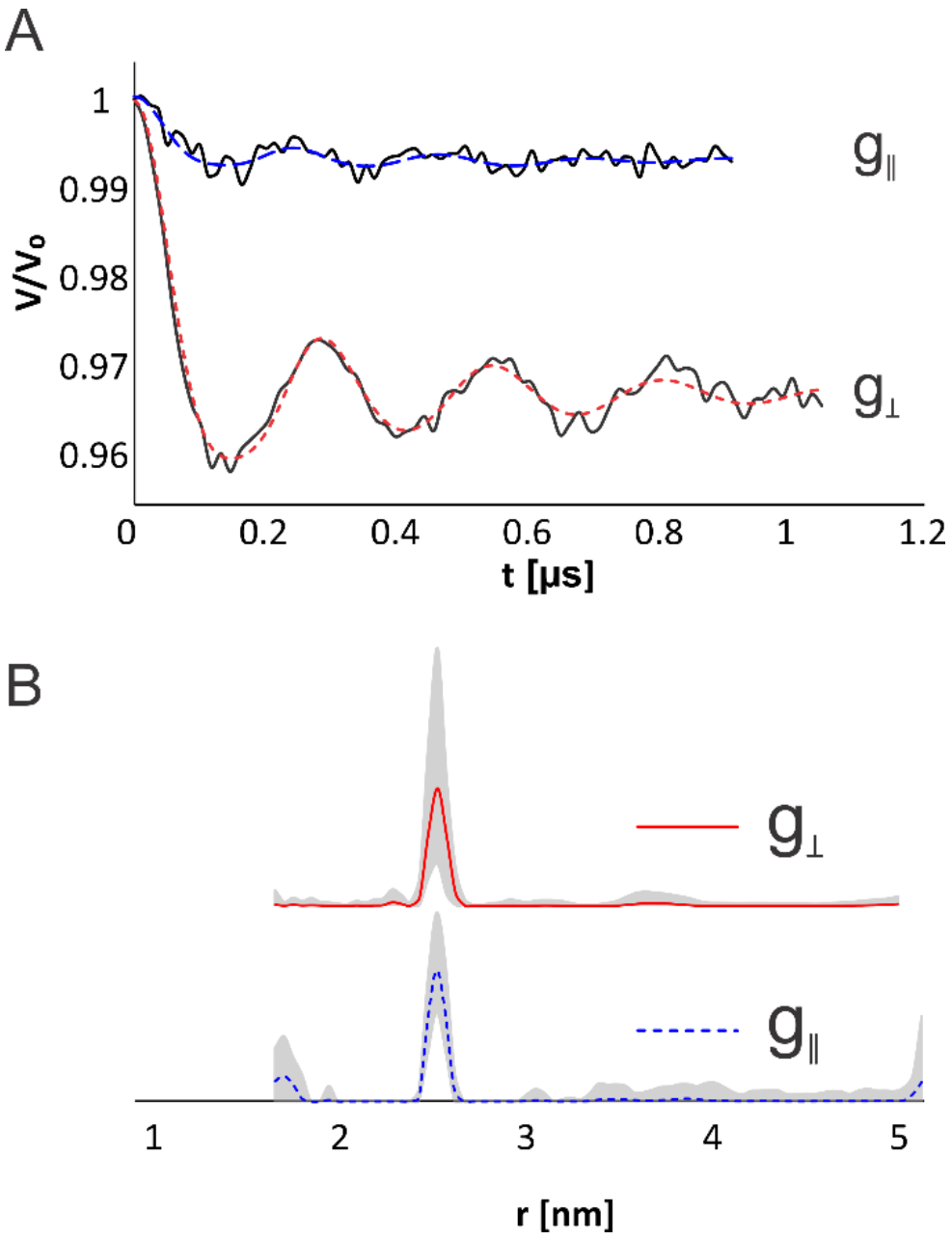

Figure 4-4 DEER data on 6H/8H/28H/32H GB1 with 1.5 eq. Cu2+-NTA complex at pH 7.4 in N-ethylmorpholine buffer at X-band. A) DEER signals (black) and corresponding Tikhonov regularization fits (dashed) at magnetic fields corresponding to g∥ and g⊥. B) Distance distributions obtained from DeerAnalysis2018[4]. Gray shading represents the uncertainty analysis. Both distributions agree with each other within >0.1 nm, indicating that orientational selectivity is not observed in this system at X-band frequencies.

Next, we simulated the data in order to determine the angle parameters using methodology previously developed by our group.[127] Figure 4-5 shows the results of these simulations, where the black lines show the experimental DEER signals and the colored lines show the simulated DEER signals for the respective magnetic fields. This methodology simulates a DEER signal based on user provided experimental parameters. These parameters include the three angles, χ, γ, and η, with an associated standard deviation, σ_χ, σ_γ, and σ_η for a given gaussian distance distribution with distance r and standard deviation dr. Thus, by specifying the magnetic field used in each DEER trace and holding all other variables constant, we can generate a series of simulated DEER signals to compare with the experimental results.

The g and hf values have been determined for the dHis Cu^{2+} site previously, where r=25.5 Å, dr=0.5 Å, $g_\perp$=2.064, $g_\parallel$=2.277, $A_\perp$=25 G and $A_\parallel$=175 G.[34] Thus, we focused on fitting the three main angles χ, γ, and η and σ_χ, σ_γ, and σ_η. In order to reduce the number of variables, we set $\sigma_\chi = \sigma_\gamma = \sigma_\eta \equiv \sigma$. From the analysis of $g_\parallel$ and $g_\perp$ field positions above, we set χ to 90^0 initially and varied γ and η systematically from 0^o to 90^o at 10^o intervals until a reasonable fit was reached. Each angle was then varied about this reasonable set by smaller intervals until the best fit was reached. This was found to be at χ=80°, γ=75°, and η=22.5° and $\sigma_\chi = \sigma_\gamma = \sigma_\eta$ = 10°. Figure 4-5 shows that the simulations provide a good fit to the experimental data across the range of magnetic fields sampled.

Because the orientational term of the DEER signal is dependent on $\cos^2(\theta)$ (Equation 4-1), one must consider the issue of symmetric solutions.[179] To understand this issue, we performed additional simulations using the best fit parameters ascertained above, and then incrementing each angle by 90°. Based on these simulations, we found that the angles χ and γ exhibited a 180°

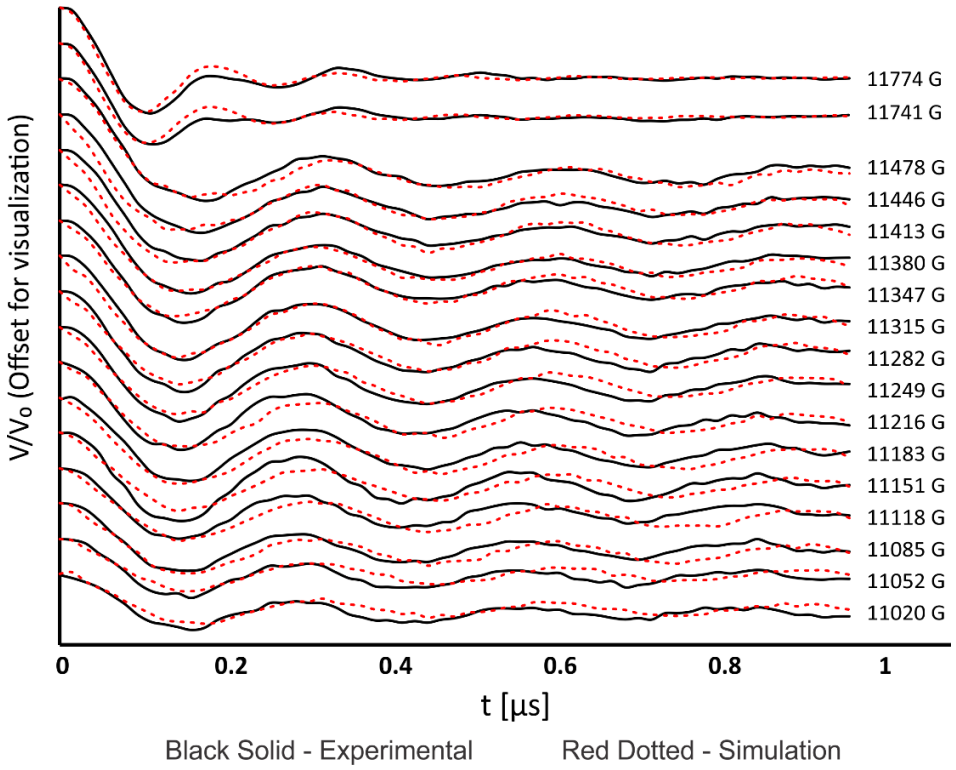

Figure 4-5 Experimental DEER signals (black) and their corresponding simulations (red dashed) offset on the y-axis for ease of visualization. The simulated DEER signals used the best set of angle parameters with r=25.5 Å, δr =0.5 Å, χ = 80°, γ = 75°, and η = 22.5° and $\sigma_\chi = \sigma_\gamma = \sigma_\eta$ = 10°

symmetry such that for either angle α, α and α+180° produced identical dipolar traces. To confirm this point, we performed an identical analysis using a different set of angles to remove any bias toward our results: χ=30°, γ=60°, and η=90°. This new set of parameters matched the previous results in which we observed a 180° symmetry for χ and γ. Because χ and γ are doubly degenerate there are 2^2 possible sets of angles that will adequately satisfy the simulations, shown in Figure 4-6. Due to the axial symmetry of Cu^{2+}, the direction of the $g_\parallel$ axis cannot be absolutely defined, and therefore there is some ambiguity in this set of solutions.[54]

Importantly, the angular results determined from simulations are in agreement with a basic visual analysis of the 6H/8H/28H/32H modified GB1 crystal structure (PDB: 4WH4).[32] This tetramutant was crystallized in the absence of Cu^{2+}. We placed Cu^{2+} ions in the structure *in silico* and positioned them with respect to the histidines based on the structure of a Cu^{2+} ion coordinated to two imidazole ligands[197] as was done previously.[32] Figure 4-7 shows this structure. To perform a visual analysis, we superimposed the proposed g-tensor axes on the crystal structure. Based on previous work, it is assumed that the imidazole nitrogens coordinate to the Cu^{2+} in the dHis motif along two of the equatorial sites.[32, 34] Therefore, from the crystal structure, we can estimate that the $g_{\perp}$ plane is formed by the Cu^{2+} ion and the two coordinating nitrogens. As well, the $g_{\parallel}$ axis can be estimated as perpendicular to the $g_{\perp}$ plane. From these axes, the angles are easily calculated, as shown. Figure 2-12 shows these axes from various perspectives such that all three angles χ, γ, and η can be easily visualized and determined. Based on the above model shown in Figure 4-7, we can measure the angles χ, γ, and η directly from the given crystal structure. From the crystal structure; $\chi \sim 77\text{-}84^{o}$, $\gamma \sim 74^{o}$, and $\eta \sim 19^{o}$. These values agree well with the best fit simulation parameters; $\chi = 80^{o}$, $\gamma = 75^{o}$, and $\eta = 22.5^{o}$. Additional work on this system utilized molecular dynamics (MD) simulations to further assess these results. Notably, MD simulations provided reasonable agreement with the values of χ and γ derived from the DEER simulation and visual analysis results in this work.[66] This finding supports our assessment of the methodology and angular values presented herein.

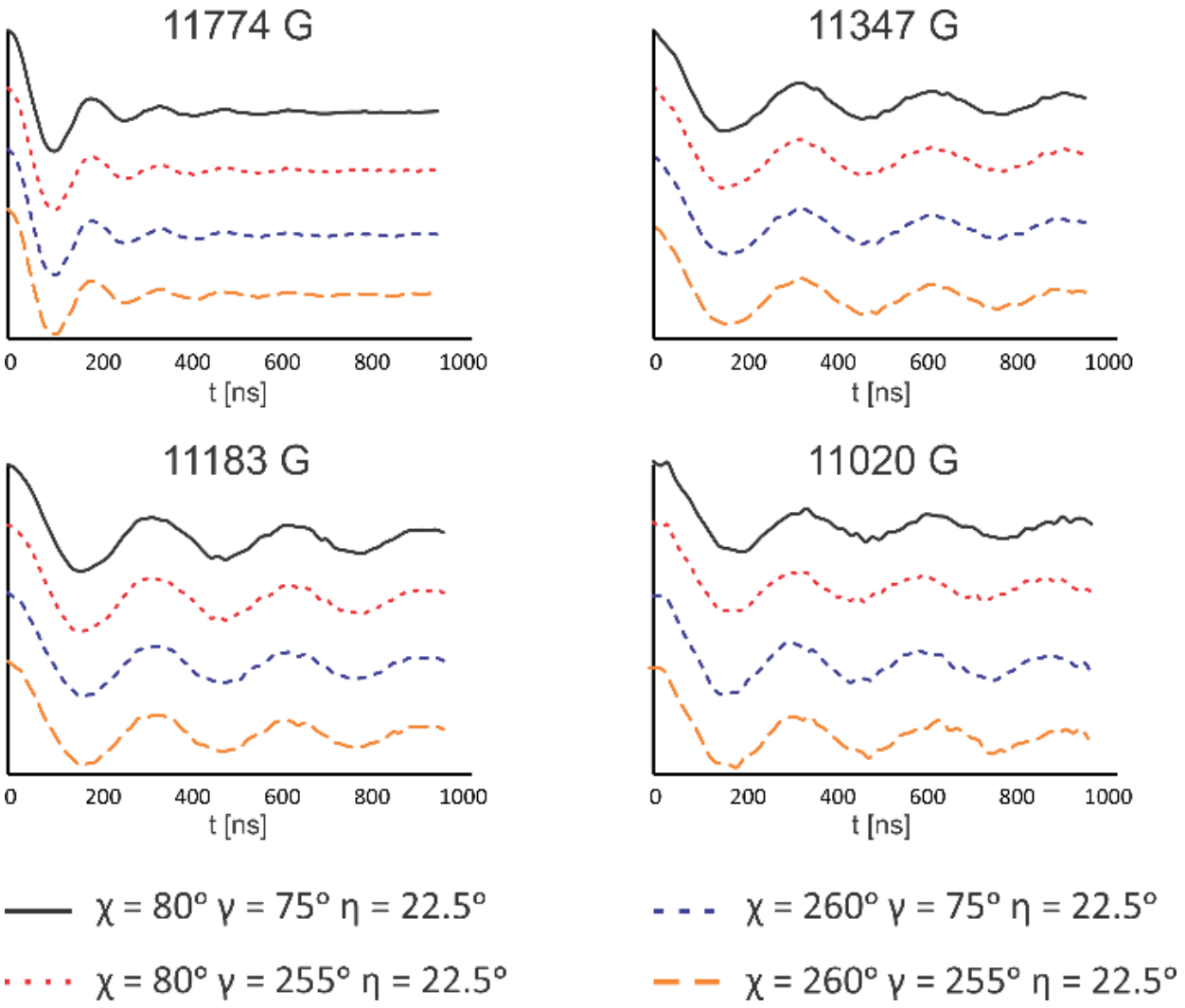

Figure 4-6 The alternative angular parameters for the best fit relative orientations according to symmetric solutions above for each magnetic field.

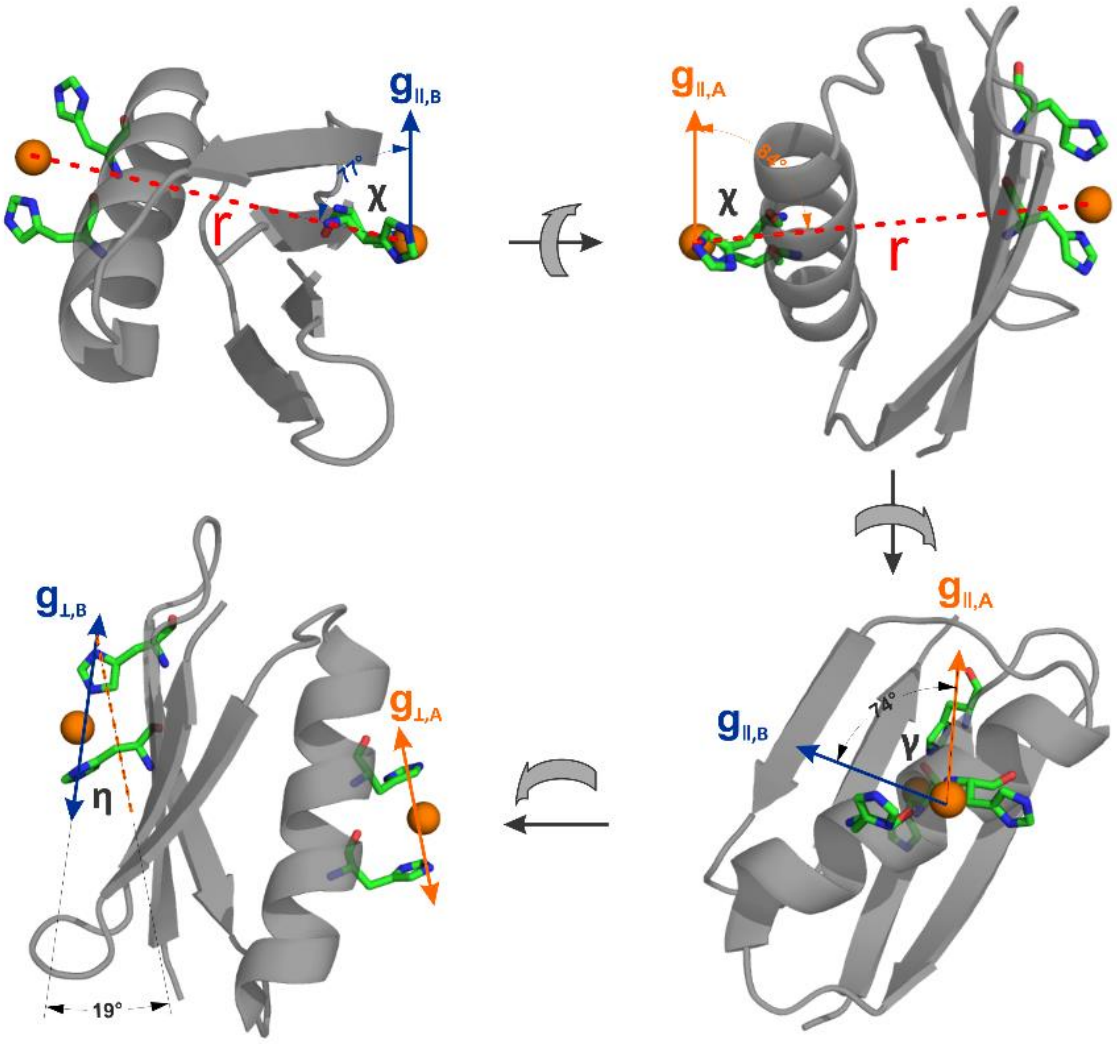

Figure 4-7 Visualization and basic analysis of the expected χ, γ, and η values determined from crystal structure. Each pane shows an estimate of the direction of an element of the Cu^{2+} g-tensor overlaid on the dHis modified GB1 crystal structure (PDB: 4WH4). The three angles can then be determined from simple graphical analysis. The angles determined in this way agree well with those determined by simulation.

Furthermore, the crystal structure analysis supports the Q-band DEER data. Figure 4-8A shows a molecular orientation found at $g_{\parallel}$, based on our visual analysis. Figure 4-8B show the Q-band DEER signal collected near $g_{\parallel}$ (red dashed) compared to the orientationally averaged X-band signal (gray). From the θ probability curves shown in Figure 4-1C, it is clear that the orientation averaged ω_{Dip} is dominated by the θ=90° orientation. The agreement between the Q-band and X-band modulation frequencies in Figure 4-8B indicate that the orientations selected at $g_{\parallel}$ are likewise dominated by θ=90°. In Figure 4-8A, the interspin vector is approximately perpendicular to B_0, such that this condition is true. Likewise, Figure 4-8C and D show corresponding data at $g_{\perp}$. From Figure 4-8C, the θ at $g_{\perp}$ selected is not close to 90°. Accordingly, Figure 4-8D shows that the modulation frequency at $g_{\perp}$ (blue dashed) does not agree with the X-band data (gray). This analysis further illustrates the sensitivity of Q-Band DEER to the relative orientations of the Cu^{2+} labels.

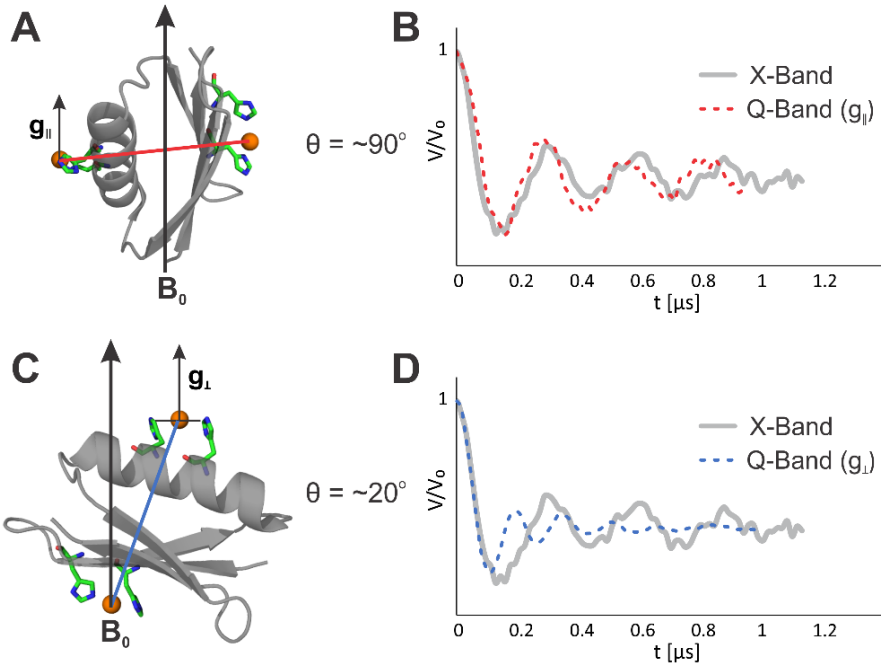

Figure 4-8 A,C) Molecular orientations of GB1 corresponding to the $g_{\parallel}$ and $g_{\perp}$ regions respectively. B, D) Resulting DEER signals dictated by the *θ* orientations selected by the orientations in A and C respectively.

We further applied our simple visual analysis to the standard deviations of χ, γ, and η. MMM is a software that labels a given protein with the dHis Cu^{2+}-NTA motif, and calculates a spatial distribution of the Cu^{2+} location.[47, 121] The positions of the Cu^{2+} centers can then be visualized. Figure 4-9 shows the dHis modified GB1 crystal structure labelled with the Cu^{2+}-NTA complex via MMM. The locations of the Cu^{2+} centers are shown in red and blue. The 6H/8H Cu^{2+} (blue) position is largely globular which leads to an ambiguous visual analysis, however the 28H/32H Cu^{2+} (red) provides some insight into the appropriate σ. The histidine residues are shown in Figure 4-9. We note that the 28H/32H Cu^{2+} positions fluctuate primarily in an arc that rotates about the C_α of the His residues. The arc in question was measured to span 60°. This angle can be easily related to η, as it is directly linked to flexibility in the $g_\perp$ plane formed by the Cu^{2+} and the His nitrogens. However, because $g_\parallel$ is perpendicular to this plane, it will also experience a 60° variance. Therefore, this range is extended to χ as well. If we assume a gaussian distribution about the mean position, a σ of 10° produces a distribution with a total range of 60°. This distribution is shown in Figure 4-9. Additionally, a σ of 10° agrees with previous findings regarding the Cu^{2+} g-tensor, in which a 10° standard deviation washed out orientational selectivity at X-band.[127] which is consistent for this system.

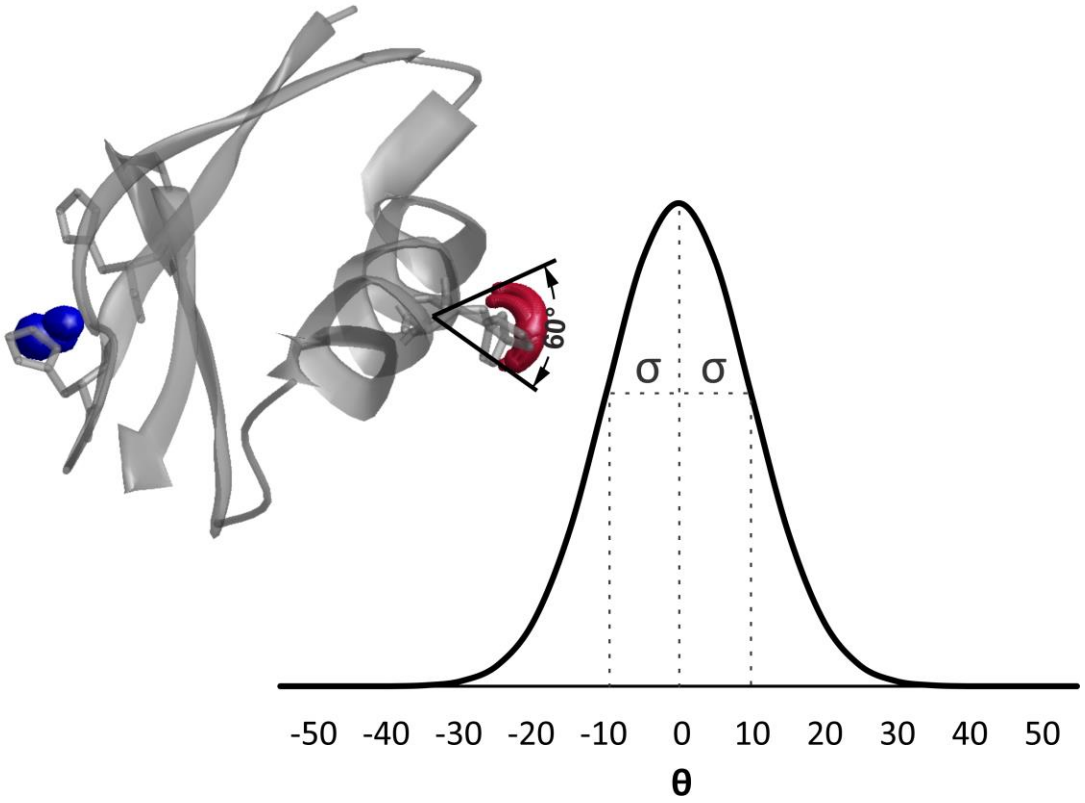

Figure 4-9 Visual analysis of the standard deviations of the angles derived from simulation. Inset shows GB1 crystal structure with Cu^{2+} positions shown in red and blue. The angular range of Cu^{2+} positions was estimated graphically as a total of 60°. A gaussian distribution with standard deviation of 10° is shown, where the total range is also approximately 60°.

4.4 Conclusion

In conclusion, we have shown the potential of Q-Band orientationally selective DEER in conjunction with the rigid Cu^{2+} binding dHis motif to provide constraints on the relative orientations of the Cu^{2+} g-tensors. We have simulated a full set of orientationally selective Q-band DEER to extract the relative orientations of the Cu^{2+} g-tensors. These results agreed well with relative orientations determined from a simple visual analysis of the protein crystal structure. The agreement demonstrates that the Q-band orientationally selective DEER can be used to determine physically meaningful spin label orientations. Likewise, the orientations of the Cu^{2+} centers in the dHis motif can be determined directly from the crystal structure. Therefore, Q-band DEER using the dHis Cu^{2+} motif can easily provide additional insight into protein structure and conformational determination.

4.5 Acknowledgements

This data was supported by the National Science Foundation (NSF MCB-1613007). The EPR spectrometer was supported by the National Science Foundation (NSF MRI-1725678). We thank Prof. Zhongyu Yang (North Dakota State University) for his advice and guidance regarding the simulations. This chapter adapted with permission from reference 64. Copyright 2018 American Chemical Society.

5.0 Development of Cu^{2+}-Based Distance Methods and Force Field Parameters for the Determination of PNA Conformations and Dynamics by EPR and MD Simulations

This work, in collaboration with Artur Sargun, Xiaowei Bogetti, Junmei Wang, Catalina Achim, and Sunil Saxena, was published in J. Phys. Chem. B, 2020, volume 124, issue 35, pages 7544-7556. The thesis author performed all EPR experimentation, all simulations and molecular modeling, analyzed all data and prepared the manuscript. This work was featured on a supplementary cover for the journal.

5.1 Introduction

Nucleic acids are an incredibly versatile category of macromolecules that have wide-ranging applications. These molecules have been used to create nano-structures and -architectures,[198-200] molecular machines,[201-203] biological sensors,[204-206] drug delivery systems,[207-209] and in the design of therapeutic methods.[210-211] Much of this field is dominated by DNA, but in recent years synthetic nucleic acids with favorable properties have also gained prominence.[212-213]

One of these synthetic nucleic acids is Peptide Nucleic Acid (PNA).[214] The PNA backbone is based on aminoethylglycine (aeg) instead of the sugar-diphosphate found in DNA/RNA. Complementary strands of PNA engage in Watson-Crick base pairing to form double helix structures.[215-216] PNA has several properties distinct from DNA and RNA that can be exploited in fundamental and practical applications. The pseudopeptide backbone of PNA lacks the negatively-

charged diphosphate group found in traditional nucleic acids. Consequently, there are no repulsive electrostatic forces between complementary PNA strands in a duplex and a PNA duplex is more stable than a DNA duplex with the same sequence of nucleobases.[71-72] Additionally, the aeg backbone is not recognized by enzymes, which makes PNA resistant to enzymatic degradation, a useful trait for biological applications.[217] Modification of the PNA monomers with various substituent groups to tailor the functionality of a PNA duplex is also relatively simple compared to the modification of DNA or RNA.[218]

These characteristics make PNA a promising material for nanotechnological applications.[219-220] In particular, PNA has potential as a tool for nanoassemblies and as a material for nanoelectronics.[221-222] In both applications, it is important to understand the structure and dynamics of the material to gain greater control over the desired architecture of the nanostructures.[223] Such control increases the chances that complex nanostructures can be built and enhances the ability to tailor the nanostructures to specific applications. In the context of nanoelectronics, it has been shown that the structure and dynamics of the PNA duplex have significant impact on its charge transfer properties. [224-226] Clearly, a thorough understanding of the structure and dynamics of PNA is paramount to expanding its application. While methods such as NMR and X-Ray crystallography enable the determination of a PNA structure, these methods can suffer from complications such as the requirement for crystallization or from size limitations.[227-229] To this end, we show that electron paramagnetic resonance (EPR) combined with molecular dynamics (MD) is a robust technique to assess PNA structure.

EPR, and particularly EPR-based nanoscale distance measurements, is a powerful technique to measure the structure and conformational dynamics of a wide variety of macromolecules.[11-12, 48-51, 118, 230-231] Because EPR detects species with unpaired electrons, it is

necessary to site selectively incorporate EPR-active species within the macromolecule.[232] These species are often organic radicals[15, 233] or paramagnetic metal ions.[32-34, 53, 56, 151-154, 156-163, 234-237] To date, much work has been performed to develop EPR-active labels for DNA and RNA in order to measure their structure and dynamics.[144, 164, 238] Some nitroxide spin labels have been developed for use with PNA, but these are limited to peptide-conjugates of PNA[239] or are restricted to attachment at the N-terminus.[240-241] In this work we present a spin label for use with EPR distance measurements that uses two 8-hydroxyquinoline moieties positioned complementarily within the PNA duplex that rigidly coordinate a Cu^{2+} ion. This spin labeling scheme is advantageous in that the rigidity allows for precise conformational determination of the PNA, as well as the fact that this label can be positioned anywhere inside the PNA duplex.

We also have developed MD force field parameters for the spin label to be used in conjunction with EPR distance measurements. Because the EPR method provides sparse constraints, additional techniques are often used for the interpretation of the measured distances in terms of structure and dynamics. In particular, MD simulations have achieved great success in interpreting EPR distance constraints with regard to molecular conformations.[30-31, 100, 242-245] MD on PNA systems using CHARMM-,[246-247] GROMACS-,[248] and AMBER-based[249-250] force fields have yielded useful insights.[250] However, the current PNA force fields do not include parameters for EPR spin labels that can provide further structural and dynamical insight and context. Herein, we developed such force field parameters to enable maximally accurate MD simulations.

Using EPR methods and MD simulations together, we examine a standard PNA duplex, i.e. a PNA whose backbone is aeg, and a PNA duplex that has a hydroxymethyl group in the γ position of aeg. Through both methods, we analyze the conformation of the PNA duplexes, and gain physical insight into the experimental EPR methodology used to measure distances.

5.2 Materials and Methods

5.2.1 EPR Measurements

Continuous wave (CW) EPR measurements were performed on a Bruker Elexsys E580 CW/FT X-band spectrometer using a Bruker ER4118X-MD5 resonator at 80 K. The CW EPR experiments were run with a center field of 3100 G and a sweep width of 2000 G, a modulation amplitude of 4 G and a modulation frequency of 100 kHz for 1024 data points using a conversion time of 20.48 ms. CW EPR was performed at multiple microwave powers to exclude saturation effects. CW EPR simulations were performed with EasySpin.[78]

The Cu^{2+} concentration was measured using a calibration curve of EPR samples of $CuSO_4$ in water with 25% v/v glycerol at Cu^{2+} concentrations of 50, 75, 100, 150, 200, 400, 600, 800, 1000, 1500, and 2000 μM. CW EPR spectra were obtained using the same experimental parameters listed above. Double integrated intensities for the standard calibration samples and the Cu^{2+}-containing PNA samples were calculated using Xepr.

Four-Pulse DEER measurements were performed on a Bruker Elexsys E680 CW/FT X-band spectrometer using a Bruker EN4118X-MD4 resonator at 20 K. Temperature was controlled by an Oxford ITC503 temperature controller and an Oxford CF935 dynamic continuous flow cryostat connected to an Oxford LLT 650 low-loss transfer tube. The pulse sequence was $(\pi/2)_{v1}$-τ_1-$(\pi)_{v1}$-τ_1+t-$(\pi)_{v2}$-τ_2-t-$(\pi)_{v1}$-τ_2-echo. The observer $(\pi/2)_{v1}$ and $(\pi)_{v1}$ pulses were 16 ns and 32 ns respectively. The pump $(\pi)_{v2}$ pulse was 16 ns. The time t was increased by a step size of 12 ns over 128 points. The time-domain data was analyzed by Tikhonov regularization.[196] Data acquisition lasted approximately 12 to 24 hours. DEER data was processed using DeerAnalysis2018.[4]

5.2.2 EPR Sample Preparation

50-100 μM solutions of the PNA duplexes in pH 7.0 10 mM sodium phosphate buffer were annealed in the presence of 2 eq of Cu^{2+} by slow cooling from 95°C to room temperature over 2-3 h. 25% glycerol (v/v) was added as glassing agent after annealing.

5.2.3 Force Field Parameterization

We performed force field parameterization for 10 PNA residues following the standard AMBER force field development procedure. We parameterized ten total PNA residues: adenine, cytosine, guanine and thymine on the standard aeg backbone (APN, CPN, GPN, and TPN, respectively), and also the same residues with a backbone modified by a hydroxymethyl group attached to the methylene group next to the N-terminus (γ-modification) (APR, CPR, GPR, and TPR, respectively), as well as two 8-hydroxyquinoline PNA residues (QPC and QPN), and the Cu^{2+} ion, (Cu). Two designations were used for HQ residues (QPC/QPN) in the pair of complementary ligands because the equilibrium bond angles between Cu^{2+} and the coordinating oxygens and nitrogens are slightly asymmetric between the two HQ ligands. This asymmetry is likely because one of the HQ groups is closer to the N-end of its strand while the other ligand is closer to the C-end of its strand. Therefore, within the QPN residue, the coordinating oxygen and nitrogen atoms required atom type designations different from those in QPC in order to ensure proper geometry. The chemical structures of these residues are shown in Figure 5-1. For each residue, we constructed a model compound by adding an acetyl (ACE) group to N-terminus and an N-methyl amide (NME) group to C-terminus. These additions make the PNA monomers for

which the force field development is performed more similar to that of the PNA monomers in the PNA oligomer.

We conducted *ab initio* calculations for the model compounds using the Gaussian 16 software package.[251] We used B3LYP/6-311++G(d,p) optimization followed by single point electrostatic potential (ESP) calculation at the HF/6-31G* level. The *ab initio* ESP was used to derive point charges with the RESP program.[252] For the QPC/QPN model compound, the solvent effect was taken into account in the optimization step by using the polarizable continuum model (PCM) implemented in Gaussian 16. Frequency analysis was also conducted for the model compound to derive force field parameters for bonds involving Cu^{2+}. We used the Residuegen program in the Antechamber module[253] to generate the topology of the A, G, C and T PNA monomers; the program removes the capping atoms and adds a charge group constraint (the net charge of capping groups is zero) during the RESP charge fittings. For the CuQ_2 complex within the PNA, QPC-Cu-QPN, we first derived charges with all four capping residues removed using the Residuegen program. We found that partial charge of Cu atom is 1.015. For the sake of simplicity, we made the point charge of Cu^{2+} 1.0 so that QPC and QPN residues each bore a -0.5 net charge. We then derived the partial charges of the QPC/QPN residues using the Residuegen program, keeping only one residue (either QPC or QPN), as partial charges of the corresponding atoms between the two residues are the same. This treatment is reasonable as the ESP relative RRMS value, which measures the charge fitting performance, is essentially same for the Residuegen runs of the QPC-Cu-QPN complex and the individual QPC/QPN residues. Note that RRMS is the square root of the ratio between the residual sum of ESP squares after fitting and the initial sum of ESP squares.

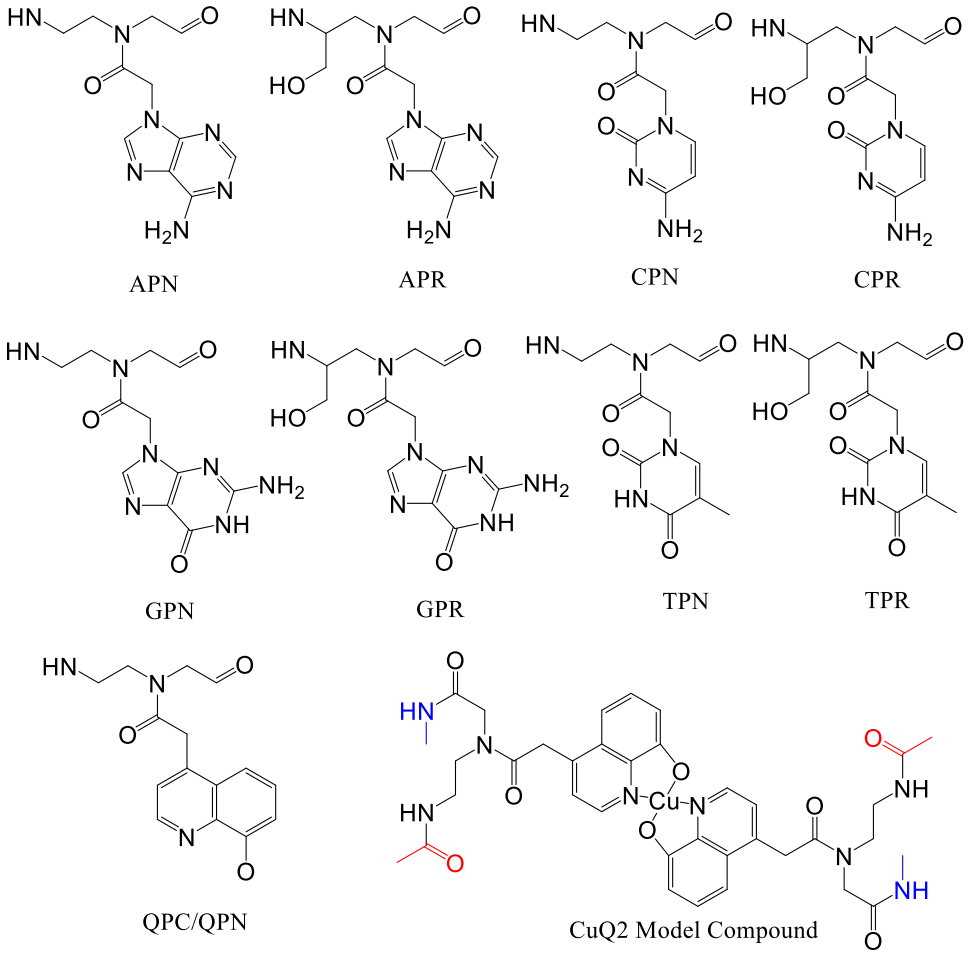

Figure 5-1 Chemical structures of PNA residues and the model compound of CuQ_2. For the CuQ_2 model compound (QPC/QPN), the N-termini are capped with acetyl group (red) and the C-termini are capped with N-methyl amide group (blue). It is noted that the QPC and QPN residues have the same chemical structures and we used different atom types for the pyridine nitrogen and phenol oxygen in QPC and QPN so that we can more accurately describe the CuQ_2 structure.

We assigned atom types using the definition table for AMBER biomolecular force fields, Parm10.[254] The missing force field parameters came from either Parm10 or the general AMBER force field (GAFF),[255] in the case that the force field parameter substitutions using Parm10 were not successful. For the force field parameters involving Cu^{2+}, the van der Waals parameters were calculated using the ionization potential and atomic polarizability of Cu^{2+} as detailed in our previous publication.[66] The bond length and bond angle parameters were obtained by analyzing the B3LYP/6-311++G(d,p) optimized geometry of the model compound. The bond stretching and bond angle bending force constants were calculated using empirical equations with parameters derived to reproduce the *ab initio* vibrational frequencies.[66] Finally, the torsional angle force constant was set to 0.0 when Cu^{2+} was not an ending atom, whereas it adopted a value of the corresponding generic torsional angle in Parm10 or GAFF.

5.2.4 Molecular Dynamics Simulations

All systems were simulated using AMBER 16.[256] The ff14SB AMBER force field was used for the Lysine residues. Solvent waters were treated with the TIP3P water model.[257] The PNA duplexes were solvated in a water box with dimensions 1.5 nm greater than the outermost dimensions of the PNA in the X, Y, and Z directions. Twenty Na^+ and Cl^- ions each were added to the water box to neutralize the system and maintain the ionic strength of the simulation system. All simulations were performed using the pmemd program in the AMBER16 software package. The ionized and solvated systems were energy minimized with a harmonic restraint force constant that was gradually reduced from 20, 10, 5, 1, to 0 kcal/mol/Å^2. Each system was then gradually heated from 0 to 298.15 K. The temperature was maintained at 298.15 K for the full simulation.

Periodic boundary conditions along with particle mesh Ewald (PME) were applied to accurately account for long-range electrostatic interactions. The temperature was controlled with the Langevin thermostat using a collision frequency of 5.0 ps^{-1}. The targeted pressure was set to 1 atm with a relaxation time of 1.0 ps. The integration time step was set to 2 ps for the equilibrium and sample phases. After the system reached equilibrium around 1 nanosecond, MD snapshots were collected every 10 ps for 100 nanoseconds. The post-analysis and g-tensor calculations with ORCA were conducted on the MD snapshots.[67-68] All molecular visualization was done using VMD.[258]

5.2.5 Solid-Phase PNA Synthesis

PNA oligomers were prepared by solid-phase peptide synthesis on an MBHA resin downloaded with L-Lys to an 0.1 meq./g NH_2 content.[259] Boc/Z-protected PNA monomers were purchased from PolyOrg Inc. and used without further purification. 8-hydroxyquinoline-modified PNA monomers were synthesized as previously described.[260] The PNA oligomers were cleaved from the solid support using a mixture of *m*-cresol/thioanisole/TFMSA/TFA (1:1:2:6) for 1 h. Cleaved PNA was precipitated using diethyl ether and purified by reversed-phase HPLC using a C18 silica column on a Waters 600 controller and pump. Absorbance was measured with a Waters 2996 photodiode array detector. Characterization of the oligomers was done by MALDI-ToF mass spectrometry on an α-cyano-4-hydroxycinnamic acid matrix (10 mg/mL in 1:1 water/acetonitrile, 0.1% TFA). The experimental molecular weights of the synthesized PNA oligomers are reported in Table 5-1.

Table 5-1 Molecular weights and MALDI-ToF MS data for the PNA oligomers.

PNA Name	PNA Sequence	Calculated	Exp.
U-PNA	H_2N-^{L}*Lys*-GTQCATCQAG-H H-CAQGTAGQTC-^{L}*Lys*-NH_2	2905.6 ($M+Na^+$)	2906.35 2907.18
γ-PNA	H_2N-^{L}*Lys*-GTQC$^{\gamma}$AT$^{\gamma}$CQAG-H H-CAQG$^{\gamma}$TA$^{\gamma}$GQTC-^{L}*Lys*-NH_2	2965.7 ($M+Na^+$)	2961.2 2964.5

^{L}Lys = L-lysine, Q = 8-hydoxyquinoline PNA monomer, γ = hydroxymethyl backbone modification

5.2.6 Circular Dichroism Spectroscopy

Circular dichroism (CD) spectra were measured for 5 μM PNA solutions in pH 7.0 10 mM sodium phosphate buffer on a JASCO J-715 spectropolarimeter equipped with a thermoelectrically-controlled, single cell holder. CD spectra were collected at 20° C, using 1 nm bandwidth, 1 s response time, 50 nm/min speed, 20 mdeg sensitivity, and 10 scan accumulation.

5.2.7 UV−Vis Spectroscopy

UV-Vis experiments were performed on a Varian Cary 3 spectrophotometer equipped with a programmable temperature block, in quartz cells of 10-mm optical path. PNA stock solutions were prepared in nanopure water (18.2 MΩ·cm). PNA concentrations were determined by UV-Vis spectrophotometry, assuming ε(260 nm) = 8600, 6600, 13700, and 11700 $cm^{-1}\cdot M^{-1}$ for the T, C, A, and G monomers, and ε(260 nm) = 2574 $cm^{-1}\cdot M^{-1}$ for the Q monomer.[260-261] PNA solutions for melting curves and titration had concentrations in the 5-10 μM range and were prepared in pH 7.0 10 mM sodium phosphate buffer.

UV melting curves were recorded in the 5-90° C temperature range at the rate of 1° C/min. The melting curves were measured at the maximum absorbance of PNA, which is 260 nm. Prior to the measurement of the melting profiles, the solutions were kept at 95° C for 10 min. T_m is the maximum of the first derivative of the melting curve.

UV-Vis titrations were carried out by addition of aliquots of standard 1000 μM $CuCl_2$ aqueous solutions to 10 μM PNA duplex solutions in pH 7.0 10 mM sodium phosphate buffer. The absorbance, A, was corrected (A_{corr}) for dilution.

5.3 Results and Discussion

In order to assess the EPR distance methods, we studied two PNA duplexes with 10 base pairs whose sequences are shown in Figure 5-2B and C. The duplex U-PNA had a backbone based on aeg (Figure 5-2A and B); the γ-PNA duplex had two monomers with a γ-modified backbone at positions 4 and 6 (Figure 5-2C). In previous work, similar γ modifications showed a rigidifying effect on the PNA.[226, 229, 262-263] An L-lysine amino acid was included at the C-terminus of each PNA strand to increase the solubility of the PNA duplex. This terminal amino acid also induces a preferred handedness in the duplex.[264] Two pairs of 8-hydroxyquinoline (HQ)-modified PNA monomers were incorporated in the 10-base pair PNA duplex at positions 3 and 8 (Figure 5-2B and C). The two HQ groups in each pair of ligands coordinate a Cu^{2+} ion to form a bis-ligand CuQ_2 complex (Figure 5-2A) that acts as spin label. The distance distribution between the two spin labels in each duplex may be measured by EPR. The analysis of these distances by MD simulations can provide information on the accessible conformations of the PNA duplexes.

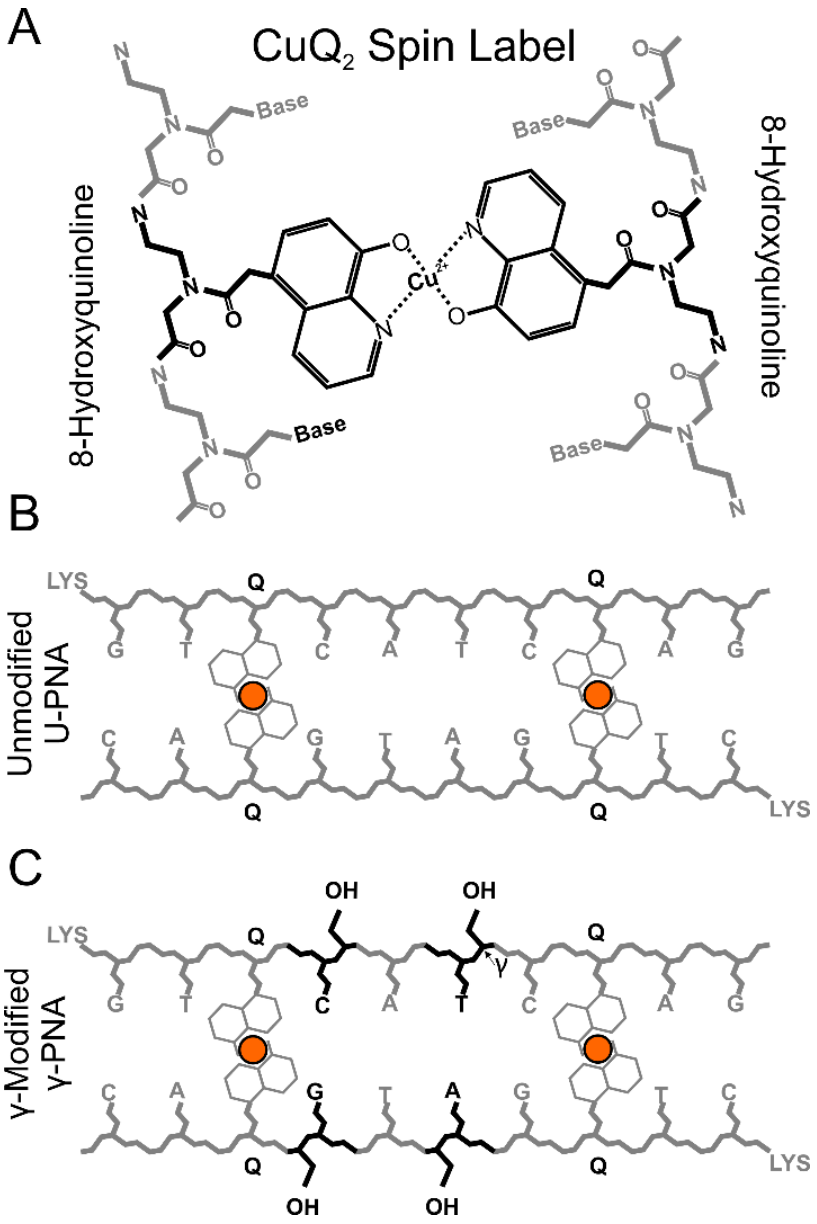

Figure 5-2 A) Schematic structure of the CuQ_2 sites in the Unmodified, aeg PNA (U-PNA). B) Schematic representation of the Unmodified PNA duplex; C) Schematic representation of the γ-hydroxymethyl-modified PNA duplex (γ-PNA).

5.3.1 Characterization of Cu^{2+} Binding in the CuQ_2 Complex

We characterized the U-PNA to ensure that the Cu^{2+} was binding to form the CuQ_2 motif and that the loading efficiency of these sites was sufficient to perform EPR distance measurements on the U-PNA system. We performed continuous wave (CW) EPR (Figure 5-3A) at X-band (ca. 9.5 GHz). The CW EPR spectrum is sensitive to the coordination of the Cu^{2+} ion and informs us on the amount of Cu^{2+} bound to the HQ sites. Figure 5-3A shows the CW EPR spectrum obtained using a 2:1 ratio of Cu^{2+} to PNA. The spectrum (black line in Figure 5-3A) was simulated as superposition (red line) of two spectral components shown as blue dashed and pink dotted lines below the measured spectrum. These two components are attributed to Cu^{2+} in two distinct coordination environments. The concentration of Cu^{2+} was determined from the double-integrated intensity of the CW EPR spectrum, and agreed with the expected amount of Cu^{2+} based on sample preparation to within 5%. We therefore assume that the CW EPR spectrum represents all Cu^{2+} added to the system. The majority component, shown in blue dashed lines, exhibited EPR parameters of $g_\perp$ = 2.0418, $g_\parallel$ = 2.2190, $A_\perp$ = 25 G (71 MHz), $A_\parallel$ = 197 G (563 MHz). These parameters agree with literature values for the CuQ_2 groups within the PNA[260] and are indicative of a square planar coordination environment of two oxygen and two nitrogen atoms.[83] The sharp features around ~3400 G in the CW spectrum are due to superhyperfine interactions from the two coordinating nitrogen nuclei. The simulations indicate that the fraction of spins in a CuQ_2 site, F_{CuQ2}, is 86±5%.

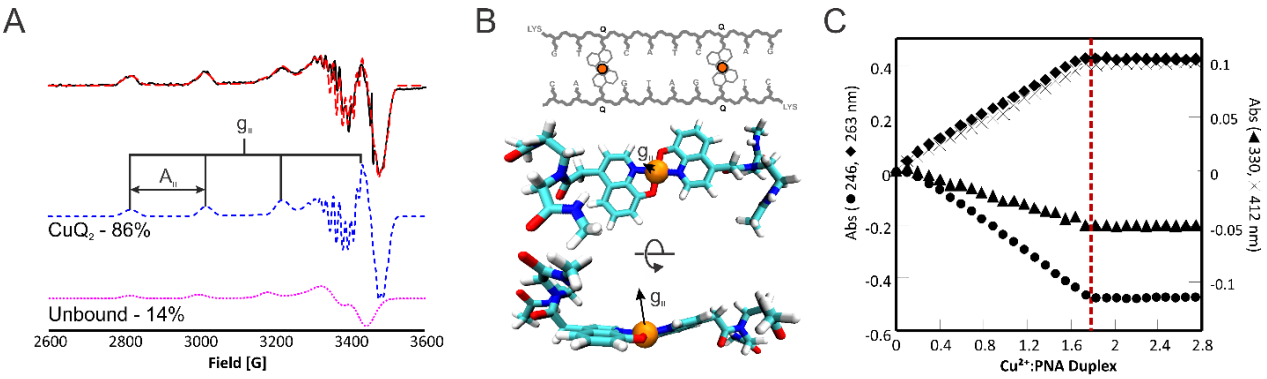

Figure 5-3 A) The X-Band CW EPR spectrum of U-PNA (black line). The simulations of spectral components attributed to CuQ_2 sites and to non-specifically bound Cu^{2+} are shown in blue dashed and pink dotted lines, respectively, below the experimental spectrum. The $g_{\parallel}$ (2.2190) and $A_{\parallel}$ (197 G, 563 MHz) parameters are marked in the CuQ_2 spectrum. The sum of the two components is shown as red dashed line overlaid with the experimental data. B) Geometry-optimized structure of the CuQ_2 binding motif using the B3LYP/6-311++G(d,p) model. The Cu^{2+} center is shown as an orange sphere, and the direction of the $g_{\parallel}$ axis is shown. C) UV-Vis titration curves for the U-PNA duplex with Cu^{2+}. The absorbance was measured at four wavelengths: 246 (circles), 263 (rhombus), 330 (triangles) and 412 nm (crosses).

The EPR parameters for the second component, shown in pink dotted lines, are $g_{\perp} = 2.0603$, $g_{\parallel} = 2.2404$, $A_{\perp} = 10$ G (29 MHz), $A_{\parallel} = 174$ G (546 MHz). These parameters are different from those of Cu^{2+} complexes in the same buffer used to dissolve the PNA duplexes (Figure 5-4), indicating that this component is not due to free Cu^{2+} in solution. The $g_{\parallel}$ of the second component is larger and the $A_{\parallel}$ is smaller compared to the values of the main CuQ_2 component, but are still indicative of a square planar or axial coordination geometry. This component could be due to coordination of one HQ ligand and adjacent nucleobases, backbone amide, water or buffer molecules.[265]

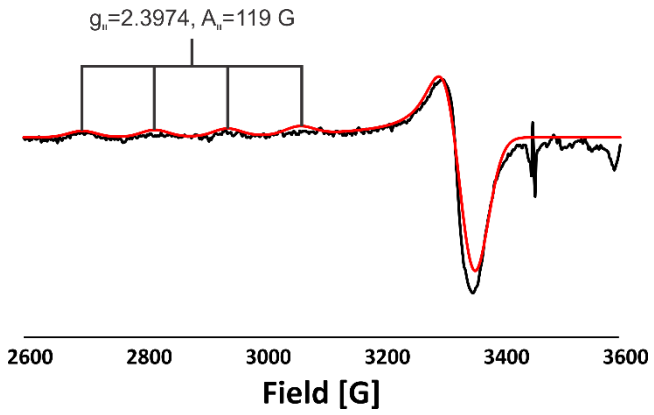

Figure 5-4 CW EPR spectrum of 150 µM $CuCl_2$ in 10 mM sodium phosphate buffer at pH 7.0 (black line), as used in all PNA samples. The simulated spectrum (red line) displayed $g_{\parallel}$ and $A_{\parallel}$ parameters are listed above to emphasize their distinct difference from those of the bound PNA CuQ_2 parameters.

We also characterized the geometry of the CuQ_2 complex *in silico* in order to ensure that the CuQ_2 in the context of the PNA residue is comparable to established crystal structures, and to inform our interpretation of our experimental results. The geometry of the CuQ_2 complex was optimized via quantum mechanical calculations (see Materials and Methods Section). The optimized geometry of the CuQ_2 complex is shown in Figure 5-3B in a top-down and profile view. This optimized structure is generally consistent with crystal structures of CuQ_2 groups, with the Cu^{2+} coordinated by two oxygen and two nitrogen atoms.[266-267] However, the angle between the normal of the planes of each HQ moiety is ~25°. In crystal structures of the CuQ_2 complex, the HQ rings are coplanar.[266-267] The difference in geometry between the optimized structure and the crystal structure may be due to the lack of constraining crystal lattice, the steric effect exerted by the PNA backbone on the complex, or due to limitations of the basis sets used in quantum mechanical calculations.

5.3.2 UV-Vis Spectroscopy Results Support CW EPR Results

The Cu^{2+} binding to the ligands in the PNA duplexes was also measured by UV-Vis titrations (Figure 5-3C). The absorbance at 246 nm, 263 nm, and 330 nm corresponds to π- π* transitions of the HQ ligand; the absorbance at 412 nm is due to a metal-to-ligand charge transfer band.[260] These transitions are sensitive to the binding of Cu^{2+} to the HQ ligands (Figure 5-5). Figure 5-3C shows the titration curves, i.e. the changes in absorbance at the four wavelengths mentioned above as a function of Cu^{2+}:U-PNA-duplex ratio. These curves show an inflection point at a ratio of Cu^{2+}:U-PNA duplex of 1.8:1, which corresponds to 90% Cu^{2+} being bound to the Q ligands in the U-PNA duplexes and agrees well with the CW EPR result.

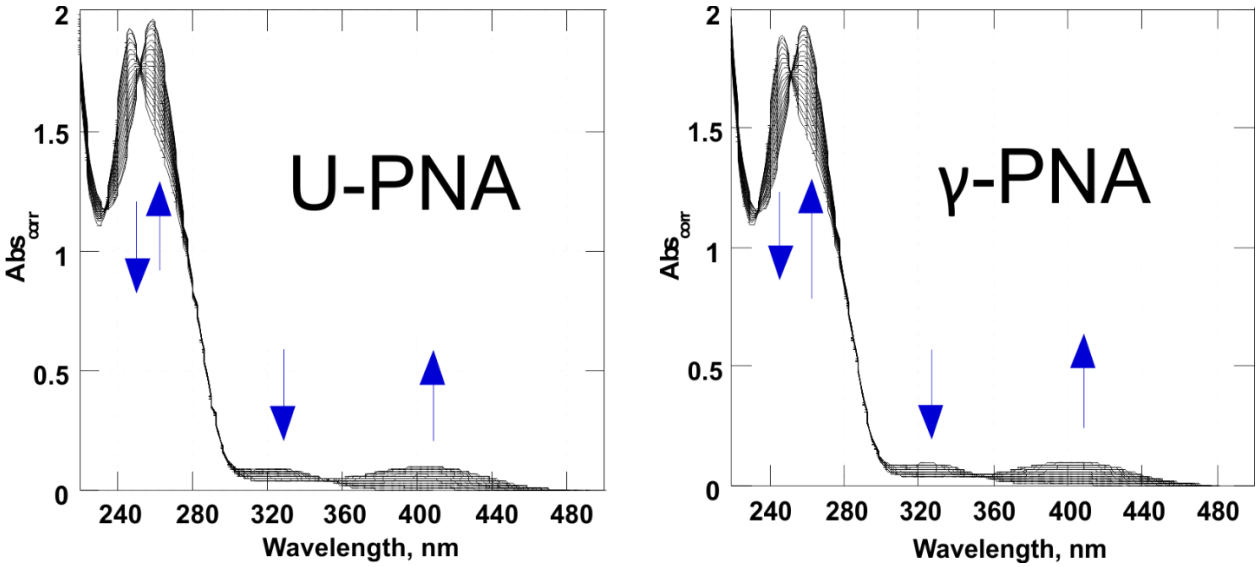

Figure 5-5 UV/Vis spectra for the titrations of $CuCl_2$ into U-PNA (top) and γ-PNA (bottom). Arrows indicate the four monitored wavelengths and their trend (increasing or decreasing) with the addition of $CuCl_2$.

5.3.3 DEER Measurements

We performed double electron electron resonance (DEER) distance measurements on the U-PNA at X-band frequencies (ca. 9.5 GHz) (Figure 5-6).[12, 48] The analysis of DEER data provides information on the probability distribution of distances between Cu^{2+} sites as well as the Cu^{2+} loading. DEER data was collected at two magnetic fields corresponding to $g_{\perp}$ (Figure 5-6A and B) and at $g_{\parallel}$ (Figure 5-6C and D) to probe this system for orientational selectivity. Orientational selectivity is a phenomenon in which DEER measurements at different magnetic fields result in different experimental signals. Such effects can occur when only a small fraction of the total EPR spectrum is excited during DEER, which may lead to only a small fraction of molecular orientations being selected.[54, 65, 127, 165-170, 174-175, 179-180] For our system, the DEER measurements at the two different fields produced a similar dipolar modulation frequency and distance distribution. The agreement between the two magnetic fields indicates that this system is not orientationally selective at X-band. This observation is discussed in detail later.

We observed a single narrow distance distribution centered at 2.0 nm (Figure 5-6B and D). The standard deviation of the distribution (FWHM) is ~0.2 nm, which indicates a small range of accessible conformations. This distribution width is similar in magnitude to that observed for comparable DNA duplexes labeled with rigid nitroxide.[268]

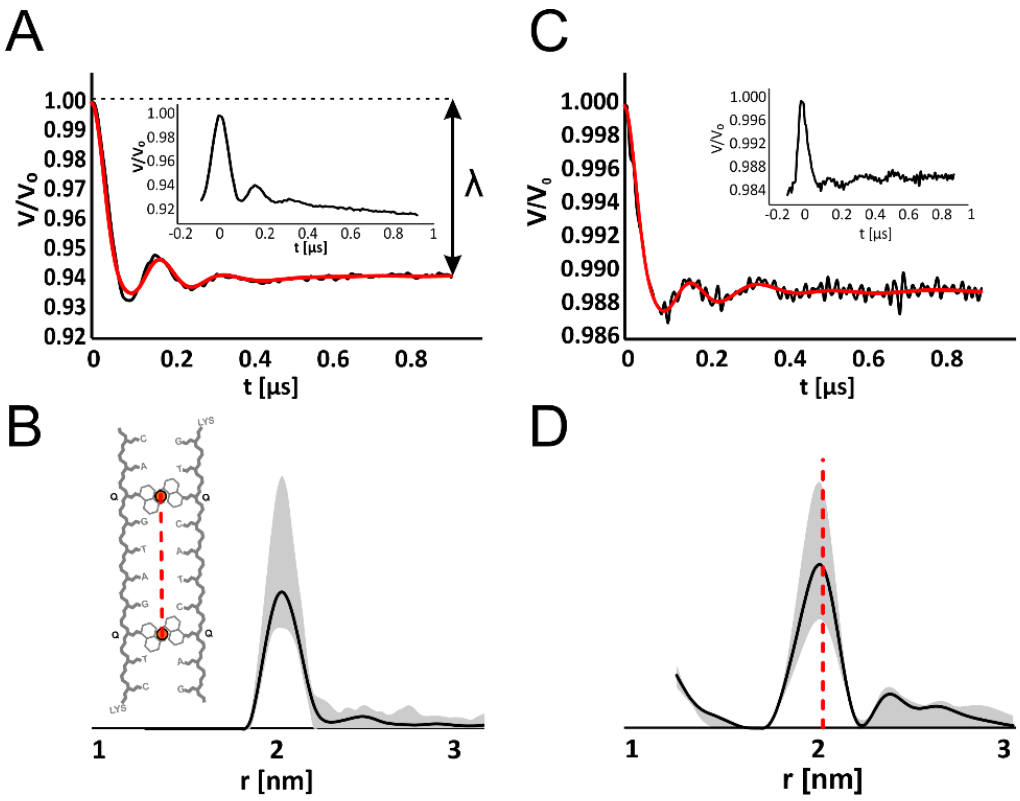

Figure 5-6 A) The background subtracted DEER signal (black line) with Tikhonov-regularized fit (red line) and raw time domain (inset) measured at $g_{\perp}$. λ is the modulation depth parameter. B) Tikhonov-regularized DEER distance distribution at $g_{\perp}$ of U-PNA (the duplex is shown in inset). The gray shading indicates the uncertainty of the distance measurement. C) Background subtracted DEER signal (black line) with Tikhonov-regularized fit (red line) and raw time domain (inset) measured at $g_{\parallel}$. D) Tikhonov-regularized DEER distance distribution at $g_{\parallel}$. The red dashed line indicates the most probable distance from the $g_{\perp}$ distance distribution from Fig. 3B.

5.3.4 Estimates of Loading Efficiency from DEER

In addition to distance constraints, DEER can provide insight into the loading efficiency of the CuQ_2 sites. While our CW data provides the fraction of Cu^{2+} spins in the bound and unbound state, analysis of DEER can inform us on the fraction of PNA duplexes that have two loaded CuQ_2 sites and those which have only one loaded CuQ_2. Such information is determined through the analysis of the modulation depth parameter, λ (Figure 5-6A), which depends in part on the number of coupled spins in the various species present in solution. The value of λ is easily read-off from our experimental DEER data (λ=0.059±0.003).

The U-PNA system has a maximum of two coupled spins – one Cu^{2+} in each CuQ_2 binding site in the PNA duplex. In a two-spin system, the modulation depth is defined as:[33-34]

$$\lambda = 1 - [f_2(1 - p_b) + f_1 + f_N], \quad (5\text{-}1)$$

where f_2 is the fraction of species attributed to PNA duplexes that contain two loaded CuQ_2 sites, f_1 is the fraction of species attributed to PNA duplexes that have only one loaded CuQ_2, and f_N is the fraction of species containing only one Cu^{2+} (but not bound to HQ in the PNA duplex). For simplicity, we assume that nonspecifically bound Cu^{2+} ions are not interacting with PNA duplexes that contain loaded CuQ_2 groups. Additionally:

$$f_2 + f_1 + f_N = 1 \quad (5\text{-}2)$$

In Equation 5-1, p_b is the probability that a 'B' spin will be excited in DEER and its value can be calculated from the echo-detected, field-swept EPR spectrum.[89] The probability, p_b, is calculated as the percentage of the area of the EPR spectrum that is excited by the pump pulse. The value of p_b is dependent on both the experimental parameters that dictate the pump pulse

characteristics and the experimental EPR spectrum for a given sample, and therefore p_b is unique for every system and experiment.

The DEER species fractions from Equation 5-1 may be related to the component ratio observed in the CW EPR data (cf. Figure 5-3):

$$F_{CuQ2} = \frac{2f_2+f_1}{2f_2+f_1+f_N} \tag{5-3}$$

$$F_{Nonspecific} = \frac{f_N}{2f_2+f_1+f_N} \tag{5-4}$$

Where F_{CuQ2} is the fraction of spins in a CuQ_2 site and $F_{Nonspecific}$ is the fraction of nonspecifically bound spins. Both F_{CuQ2} and $F_{Nonspecific}$ are readily available from the CW EPR simulations (Fig. 5-3). Specifically, F_{CuQ2}=0.86 and $F_{Nonspecific}$=0.14. It is important to note that the fractions, F_{CuQ2} and $F_{Nonspecific}$ are proportional to the concentrations of the CuQ_2 and nonspecifically bound species, respectively. The DEER modulation depth, on the other hand, does not directly reflect the species concentration, but is instead sensitive to the number of coupled spin species and uncoupled spin species, as per Equation 5-1. Therefore, every doubly labeled PNA that contributes one unit to f_2 will contribute two units to F_{CuQ2}, because a single coupled spin species contains two Cu^{2+} centers. This important distinction means that $F_{CuQ2} \neq f_2 + f_1$ and $F_{Nonspecific} \neq f_N$.

Using the constraints of Equations 5-1 – 5-4, we can calculate a species distribution for samples of U-PNA that contain Cu^{2+}. Doing so, we arrive at f_2=0.78±0.03, f_1=0.03±0.03, and f_N=0.19±0.04. The errors in the fractions were calculated by taking into account the experimental error inherent in the DEER modulation depth (0.003) and our CW EPR simulations (0.05). This information shows a relatively efficient loading of the Cu^{2+} into the CuQ_2 sites that is adequate for

DEER distance measurements. DEER distance measurements themselves produce clean, narrow distance distributions that will aid in the unambiguous analysis of the data.

5.3.5 Molecular Dynamics Simulations

We utilized molecular dynamics (MD) simulations to understand the EPR results in an atomistic context. We constructed our initial PNA model for MD simulations in silico using PDB 2K4G as a starting template.[229] The geometry of each nucleobase and of the CuQ_2 groups were optimized using quantum mechanical calculations, and then force field parameters for the each group were generated for use with the AMBER molecular simulation software.[256] The details are provided in the Methods section. Explicit bonds were formed between the Cu^{2+} atom and the coordinating oxygen and nitrogen atoms from both HQ groups.

With the PNA systems parameterized, we performed MD simulations of U-PNA for 100 ns. The distance between the two Cu^{2+} ions in the duplex was measured from frames of the simulation obtained every 10 ps. The distribution of these distances is shown as a red dashed line in Figure 5-7A, overlaid on the experimental DEER distance distribution. The MD distance distribution agrees well with both the most probable DEER distance as well as the total distribution width. This agreement indicates that the MD simulations accurately reproduced the overall structure and range of accessible conformations of the U-PNA duplex.

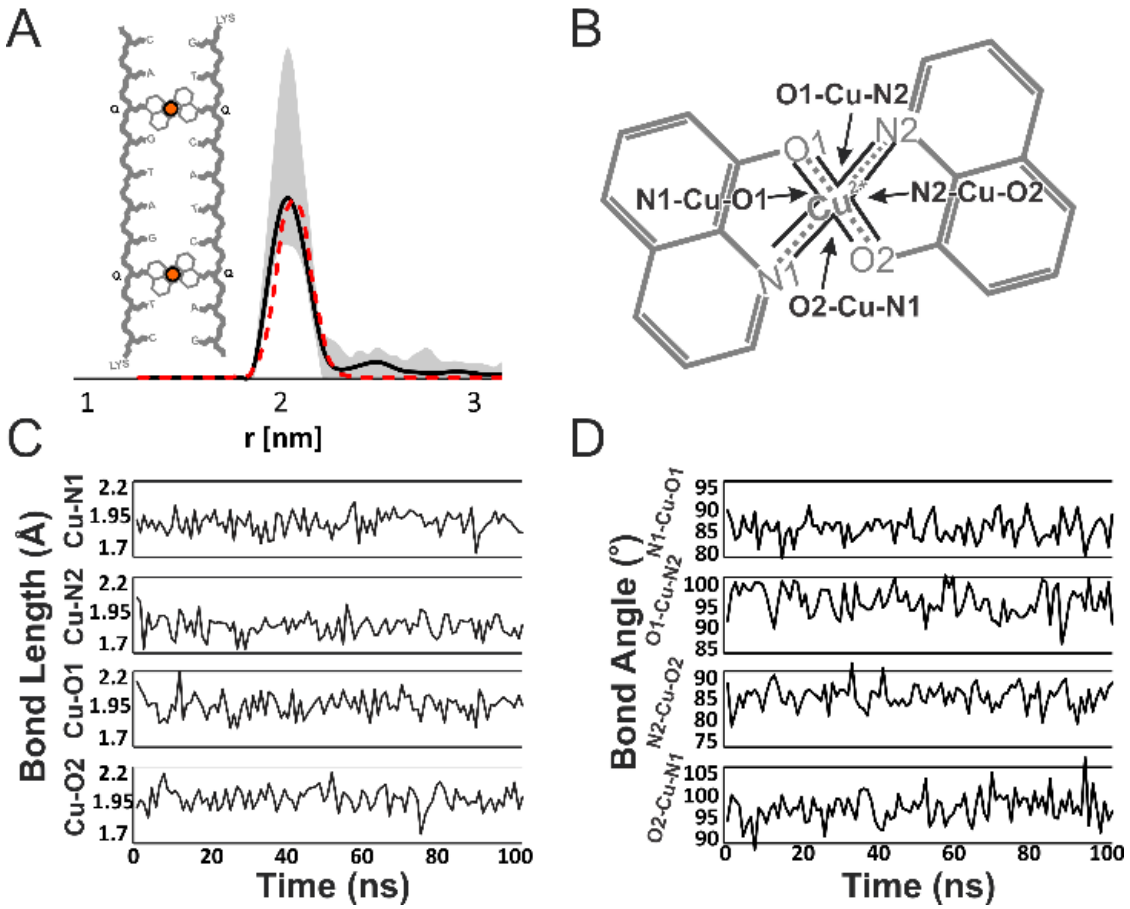

Figure 5-7 A) MD simulation results for U-PNA. Distance distributions showing the Tikhonov regularized DEER distribution is shown in black with uncertainty analysis (gray shading). The MD Cu^{2+}-Cu^{2+} distribution is shown as a red dashed line. B) Chemical structure of the CuQ_2 group. Coordinating atom names and Cu^{2+} bond angles are designated for reference. C) Bond lengths between the Cu^{2+} and each coordinating oxygen and nitrogen sampled every 1 ns from the MD. D) Cu^{2+} bond angles defined in (B) sampled every 1 ns.

5.3.6 Insight into Orientational Selection in DEER from MD Results

We analyzed the Cu^{2+} coordination environment in the CuQ_2 complex, specifically the bond lengths and bond angles of the Cu^{2+} and its four coordinating atoms, obtained by MD simulations, and related it to the EPR results. First, we measured the coordination bond lengths from the central Cu^{2+} to each of the four coordinating atoms as defined in Figure 5-7B. These bond lengths, sampled every 1 ns, are shown in Figure 5-7C. Each bond displayed an average length of approximately 1.9 Å with a standard deviation of 0.1 Å. These bond lengths are in good agreement with those found in typical Cu^{2+}-8-hydroxyquinoline complexes.[266-267] Next, we monitored the Cu^{2+} bond angles identified in Figure 5-7B. These angles are shown in Figure 5-7D. The O1-Cu-N2 and O2-Cu-N1 bond angles that involve coordinating atoms from different HQ ligands were ~85±2.5^o (average±s.d.). The N1-Cu-O1 and N2-Cu-O2 bond angles involving coordinating atoms from the same HQ ligand were ~95±3^o. Each of these angles was found to fluctuate up to ±10^o from their average value. The overall analysis of the CuQ_2 coordination shows variations in bond angles and lengths, a phenomenon that has been reported recently for another Cu^{2+} spin label.[66]

These variations in coordination environment, although subtle from a macromolecular viewpoint, have important implications on the g-tensor of the Cu^{2+}. We used ORCA to calculate the g-tensor values and orientations for CuQ_2 from 100 frames evenly sampled throughout the MD simulation.[67-68] These calculations show that the value of $g_{\parallel}$ changes by 0.5%. To determine the extent of orientational fluctuation, we aligned each ORCA frame along the Cu^{2+} center and its four coordinating atoms by minimizing the RMSDs of the distances between equivalent atoms at each different frame. Based on this alignment of the Cu^{2+} local coordination environment, the orientation of $g_{\parallel}$ displayed a distribution of up to ~22.5^o from its average orientation. This

distribution in the orientations of g-tensors is shown as the black lines in Figure 5-8A. From this analysis, it is clear that the fluctuations in Cu^{2+} coordination environment lead to a large distribution in orientation of the Cu^{2+} g-tensor. We note that in the distribution of $g_{\parallel}$ some individual axes are orientated 'up' and 'down' with respect to the plane defined by the Cu^{2+} and its coordinating atoms in the CuQ_2 complex. Previous analyses of $g_{\parallel}$ have elucidated a 180° symmetry of the $g_{\parallel}$ axis, as it is indistinguishable in the 'upward' and 'downward' orientations, and that the axis in either orientation produces the same DEER results.[54, 65] Therefore, this finding is not unexpected.

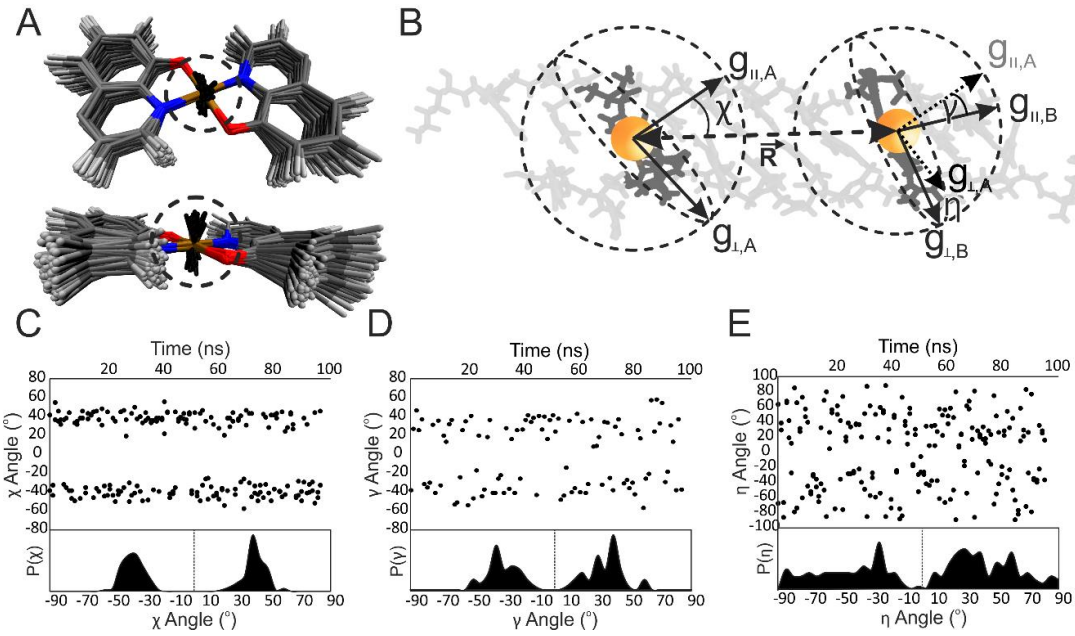

Figure 5-8 An orientational analysis of the CuQ_2 binding motif and its implications on EPR measurements. A) The distribution of $g_{\parallel}$ directions (black lines) over the CuQ_2 structure as sampled every 1 ns of the MD run. g-tensor calculations were performed with ORCA.[67-68] Individual structures were aligned to minimize the RMSD of the distances between the Cu^{2+} center and the four N and O coordinating atoms in each individual frame. B) The definitions of each angle, χ, γ, and η, in the context of the U-PNA structure. These angles define the relative orientations of the CuQ_2 g-tensors. C, D, E) Plots of the χ, γ, and η respectively. The top charts show the angular values sampled every 1 ns. The bottom charts show the probability distribution of each angle.

Additionally, such changes in the orientations of $g_{\parallel}$ can profoundly affect the relative orientations of the g-tensors of each of the two Cu^{2+} spins. This relative orientation is described in terms of the three polar angles, χ, γ, and η shown in Figure 5-8B. χ is the angle between the $g_{\parallel}$ axis of a Cu^{2+} center and the vector that connects the two Cu^{2+} centers, $\vec{R}$. γ is the angle between the $g_{\parallel}$ axes of the two Cu^{2+} centers. η is the angle between the $g_{\perp}$ axis of one Cu^{2+} and the projection of the second $g_{\perp}$ axis onto its perpendicular plane. Figure 5-8C, D, and E show these angles calculated from the 100 selected ORCA frames of the CuQ_2 complexes. Angle χ is bimodal with an average around $\pm 40^{o}$, and a standard deviation of 7^{o}. The angle γ averages $\pm 45^{o}$ with a standard deviation of 20^{o}, whereas η provides an even wider distribution of angles.

Previous work has shown that such a wide distribution of orientational angles is sufficient to ensure that the pulses used in DEER excite a wide range of molecular orientations thereby "washing out" the effect of orientational selectivity,[66, 127, 133] which explains the DEER results shown in Figure 5-6. We can visualize and validate this point by aligning the $g_{\parallel}$ axes of one Cu^{2+} center and overlaying the U-PNA structure from each frame with the second Cu^{2+} displayed as spheres. Figure 5-9 shows the reference Cu^{2+} center as an orange sphere and the second Cu^{2+} center in the PNA duplex as red spheres. This figure reveals that the fluctuations of the Cu^{2+} coordination environment and consequential fluctuations in the direction of $g_{\parallel}$ drastically increase the molecular orientations that are sampled by the pump pulse in DEER at the single selected $g_{\parallel}$. With the finite bandwidth of pulses applied in DEER, the distribution in molecular orientations grows even larger. This analysis provides clear conceptual understanding for the mechanism by which orientational selectivity is washed out in Cu^{2+} DEER at X-band frequencies.

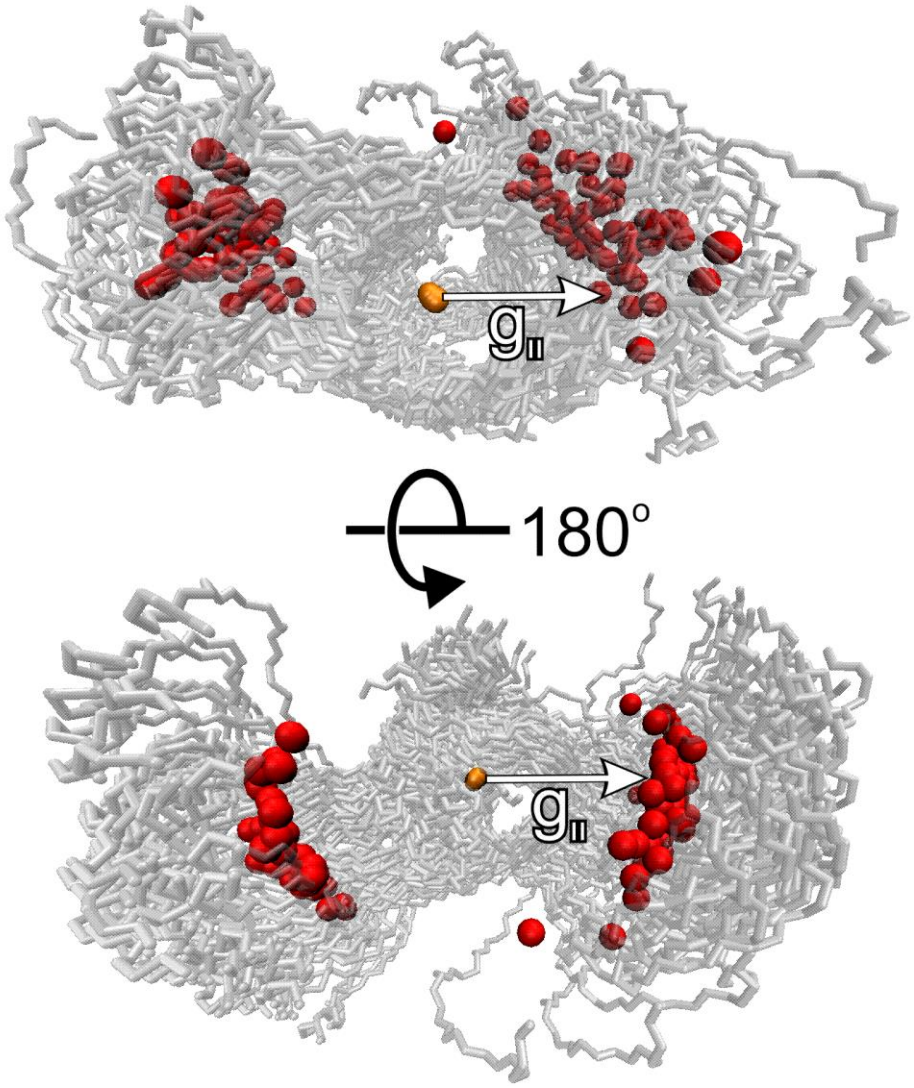

Figure 5-9 100 overlaid MD frames of U-PNA sampled every 1 ns along the MD trajectory, aligned along the $g_{\parallel}$ axis of one CuQ_2 site. The selected Cu^{2+} is shown as a sphere in the center, with the direction of the aligned $g_{\parallel}$ axis marked. Only the backbone atoms of the PNA duplex are displayed for simple viewing. The Cu^{2+} ions of the second CuQ_2 complex are also shown as red spheres. This figure emphasizes the many molecular orientations selected at a single $g_{\parallel}$ orientation

5.3.7 Characterization of γ-Modified PNA by EPR and UV-Vis Spectroscopy

Next, we explored the utility of EPR as a tool for the analysis of the structure of a γ-modified PNA duplex. Such data is important because the addition of substituent groups to the PNA backbone can be used to tailor the properties of the PNA. The PNA contained a hydroxymethyl modification on the γ-carbon of the peptide backbone in the base pairs adjacent to, or 1 base pair away from, the CuQ_2 sites (Figure 5-2).

As with the U-PNA, we performed CW and UV-Vis measurements on the γ-PNA. The CW spectrum for γ-PNA (Figure 5-10) is similar to that of the U-PNA. We determined the concentration of Cu^{2+} from the double-integrated intensity of the CW EPR spectrum, which again agreed with the expected concentration to within 5%. The spectrum of the γ-PNA was simulated using the EPR parameters determined for the U-PNA. From these simulations, we calculated the 74±5% CuQ_2 loading. This loading efficiency is significantly lower than that measured for the U-PNA and may be due to alterations in the environment directly surrounding the Cu^{2+} binding site caused by the γ-modifications to bases directly adjacent to the CuQ_2 sites.[238]

The UV-Vis titrations of γ-PNA in Figure 5-10B show a maximal Cu^{2+} binding at 1.8:1 Cu^{2+}:PNA duplex, or 90±5%, which differs from the CW simulation value of 74±5%. This discrepancy may be due to differences in the duplex preparation, to differences in the concentration of the samples for UV-Vis and EPR experiments, and/or to the presence of glycerol in the EPR samples. More specifically, for the UV-Vis titration, the PNA duplex was first formed by annealing and then $CuCl_2$ was added into the solution containing the duplex, whereas for the EPR sample, the duplex was annealed in the presence of two equivalents of Cu^{2+} (Figure 5-11). For the UV-Vis experiments, the concentration of the samples is 5-10 μM; for the EPR samples the Cu^{2+}

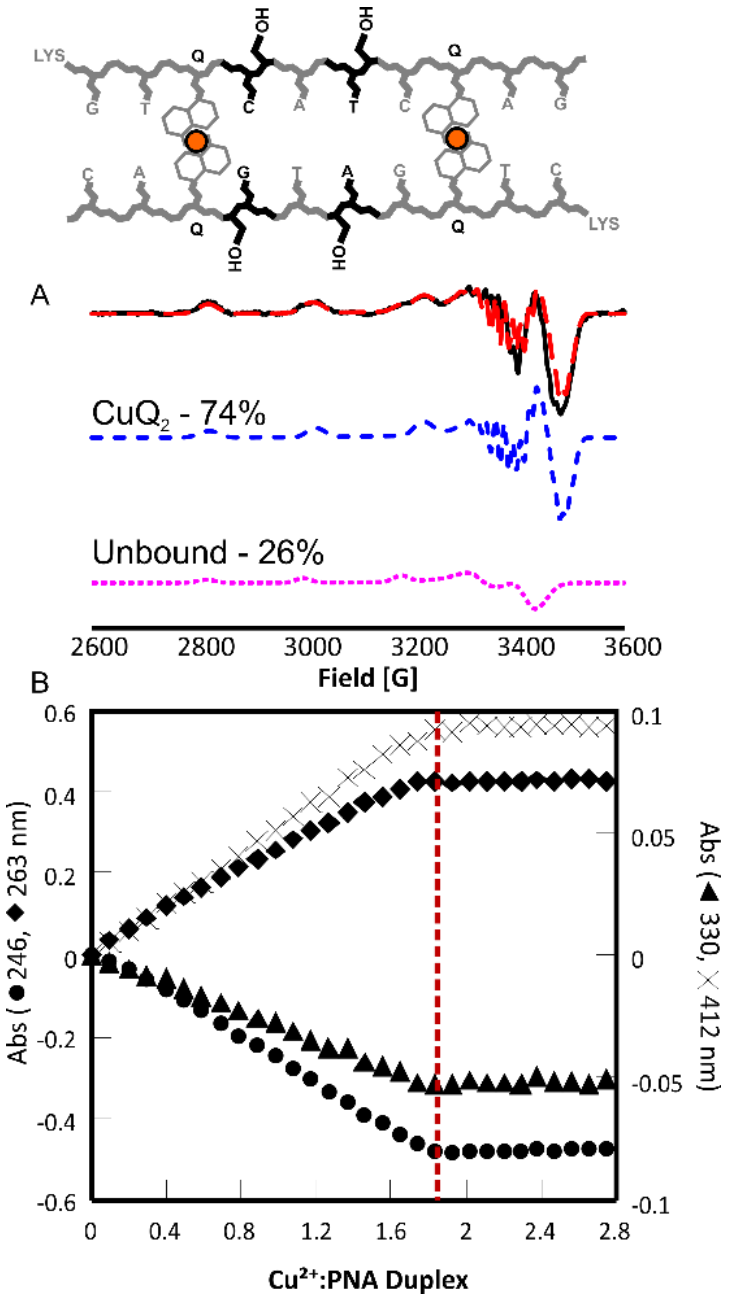

Figure 5-10 A) CW EPR spectra of γ-PNA. The experimental CW spectrum is shown in black. The simulations of spectral components attributed to CuQ_2 sites and to non-specifically bound Cu^{2+} are shown in blue dashed and pink dotted lines, respectively, below the experimental spectrum. The sum of the two components is shown as a red dashed line overlaid with the experimental data B) UV-Vis titrations curves for the γ-PNA duplex with Cu^{2+}.

concentration is 100-200 µM. Additionally, in EPR samples glycerol must be used as a glassing agent and cryoprotectant because the EPR spectra are collected at 80 K while glycerol was not added to the solution used in the UV-Vis titrations.

CD spectra for U-PNA and γ-PNA have been measured in the absence and presence of 2 eq of Cu^{2+} (Figure 5-11). The cause of a preferred handedness in the PNA duplexes is the chiral terminal L-Lys, which is present both PNA duplexes, as well as the γ-PNA monomers in the γ-PNA duplex.[264] The spectra shown in Figure 5-11 reveal that in the absence of Cu^{2+}, U-PNA and γ-PNA adopt a left-handed structure.[71] The handedness of the U-PNA duplex is unaffected by the metal coordination to the Q ligands in the PNA (Figure 5-11A). In contrast, the preferred handedness of the γ-PNA duplex (Figure 5-11B) is changed upon metal coordination to the Q ligands.

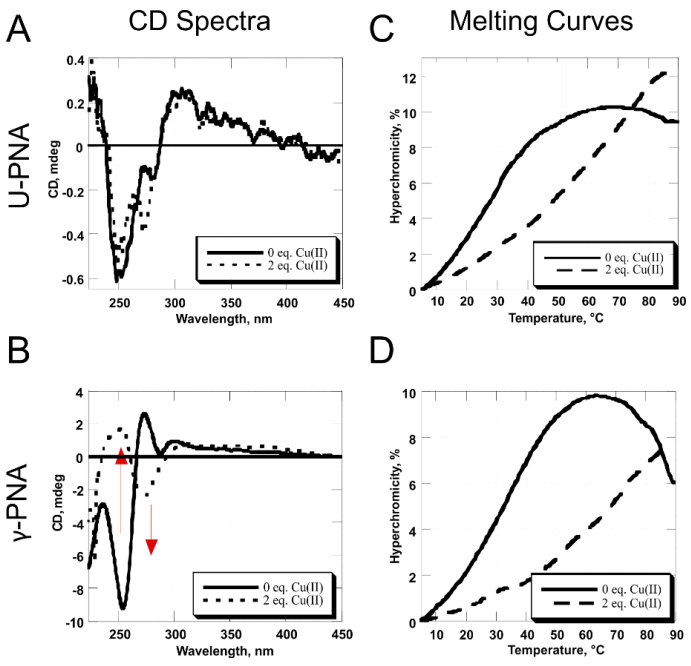

Figure 5-11 Circular Dichroism data for U-PNA (A) and γ-PNA (B). Thermal UV/Vis curves for U-PNA (C) and γ-PNA (D). Each experiment was performed on the PNA in the presence and absence of 2 equivalents of Cu^{2+} as indicated.

As well, the thermal stability of the PNA duplexes was studied by monitoring the absorbance at λ_{max} = 260 nm as a function of temperature, both in the absence and presence of Cu^{2+} ions (Figure 5-11C and D). The melting temperature of the non-modified PNA duplex in 10 mM solutions in pH 7.0 phosphate buffer is 67^{o} C. The U-PNA melting curves without added Cu^{2+}, shown in Figure 5-11C as the solid line. showed an increase of hyperchromicity that allows one to establish ~26°C as an upper limit for the melting temperature of the duplex, a result that is in agreement with the low mismatch tolerance of PNA.[260] Upon addition of two equivalents of Cu^{2+}, shown as the dashed line in Fig. 4-13C, the melting temperature increased to ~65^{o} C. Incorporation of γ-modified monomers in γ-PNA did not cause a significant increase in the thermal stability of the duplex relative to U-PNA, shown in Figure 5-11D as the solid line, with an upper limit of ~31C. Again, with two equivalents of Cu^{2+} added, shown in Figure 5-11D as the dashed line, the melting temperature increased to ~65-70^{o} C. In both PNA duplexes, the Cu^{2+} has a stabilizing effect of around ~30-40^{o} C.

Next, we performed DEER measurements on the γ-PNA (Figure 5-12A). As with the U-PNA, we see clear dipolar modulations in the DEER signal. The distance distribution between the two Cu^{2+} centers in the duplex is similar to that measured for U-PNA, with a most probable distance at 2 nm and a full width at half height of 0.2 nm (Figure 5-12B). This observation suggests that the inclusion of only sparse γ-modifications in the PNA duplex does not cause significant changes in the range of PNA conformations. The analysis of the orientational angles for γ-PNA (Figure 5-13) led to angular distributions with similar averages and standard deviations as the U-PNA, making an experimental probe of orientational effects unnecessary. Therefore, the DEER was performed only at $g_{\perp}$.

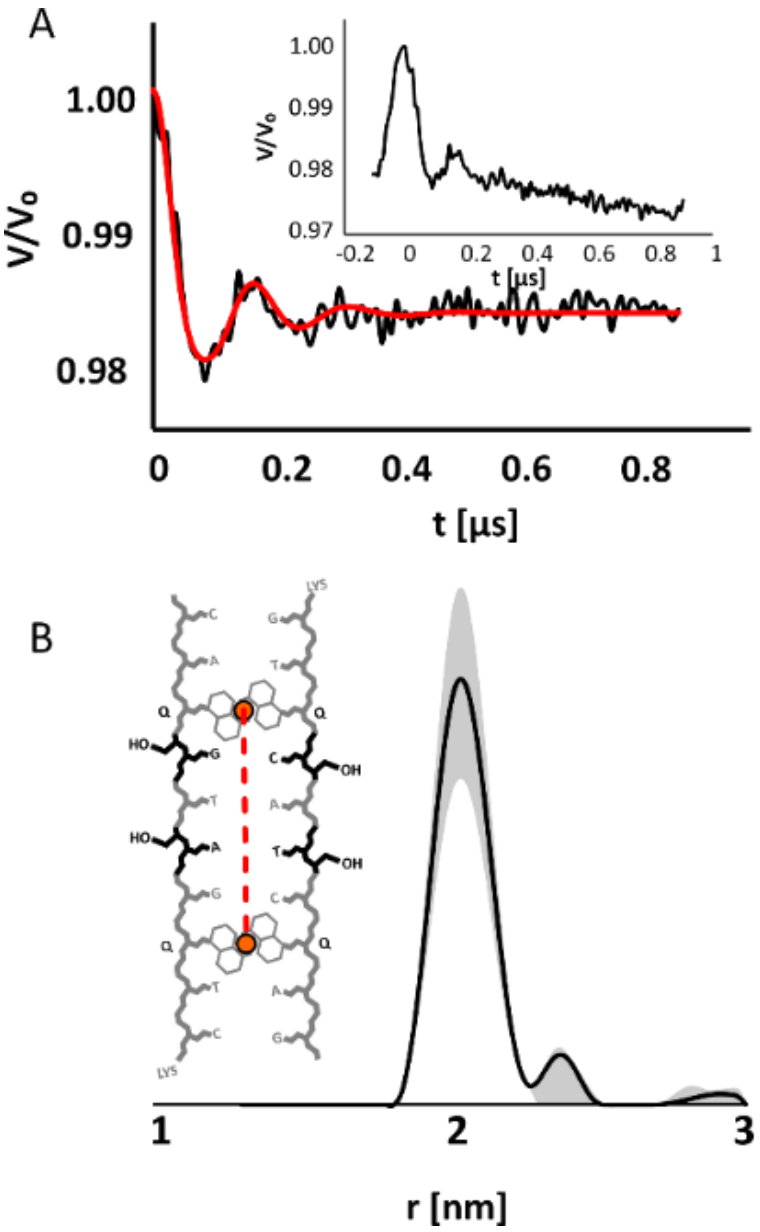

Figure 5-12 A) The background-subtracted DEER signal with Tikhonov regularized fit (red line) and raw time domain (inset) for γ-PNA. B) Tikhonov-regularized DEER distance distribution, with cartoon representation of γ-PNA (inset). The gray shading indicates the uncertainty of the distance measurement.

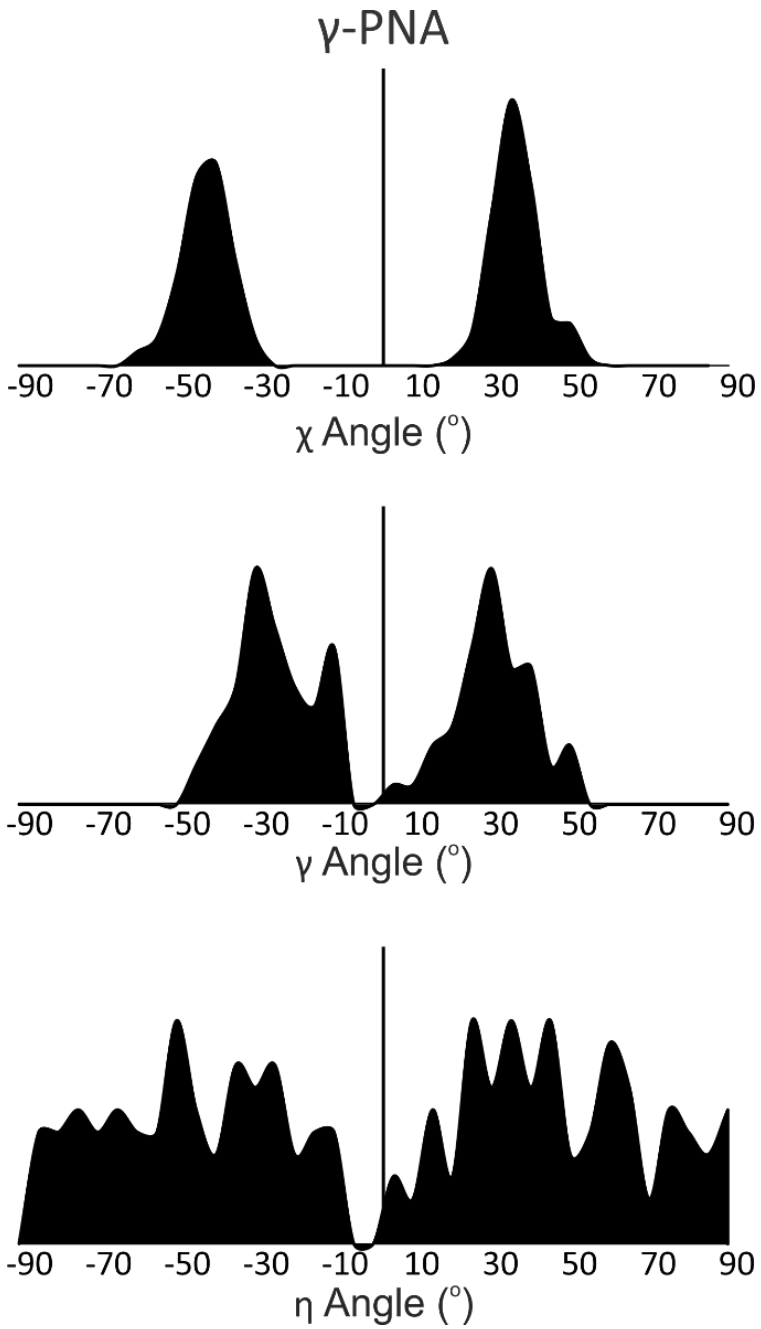

Figure 5-13 Probability distributions for each of the three orientational angles defined in Figure 4-10, calculated for γ-PNA via ORCA.[67-68] Notably, the average angles and standard deviations are similar in magnitude to those determined for U-PNA.

The most notable difference between the DEER performed on γ-PNA and the U-PNA is in the modulation depth. γ-PNA shows a λ = 0.016 modulation depth compared to 0.059 for U-PNA. This result follows from the CW EPR findings that showed a reduced amount of total Cu^{2+} bound in the γ-PNA. We analyzed the modulation depth on the γ-PNA by the method described above for U-PNA, under the same base assumptions. We used the component fractions determined by CW EPR, i.e 74±5% CuQ_2 binding and the values of λ=0.016 and p_b of 0.051 determined from the EPR data.[89] We calculated f_2=0.32±0.02, f_1=0.34±0.07, and f_N=0.34±0.07. Clearly, in the context of the EPR sample preparation conditions, the γ-modifications disrupt the loading efficiency of the CuQ_2 sites and lead to a ~40% reduction in the population of doubly-labeled PNAs. However, even with this decrease in loading efficiency, the EPR distance measurement still provides a clear, narrow distance distribution that is well suited for conformational determination.

5.3.8 MD Simulations and DEER Distance Measurements Provide Atomistic Insight into PNA Structure

Following the DEER measurements, we generated an initial structure for the duplex and force-field parameters for the γ-modified base pairs and performed MD simulations on γ-PNA for 100 ns (Figure 5-14). The Cu^{2+}-Cu^{2+} distance distribution obtained for the MD simulations (red dashed line in Figure 5-14) agrees well with distance distribution obtained from EPR. Again, this agreement applies to both the most probable distance as well as the to the width of the distribution. Based on these results, we believe that EPR distance methods in conjunction with MD simulations are applicable to PNA systems containing γ-modifications.

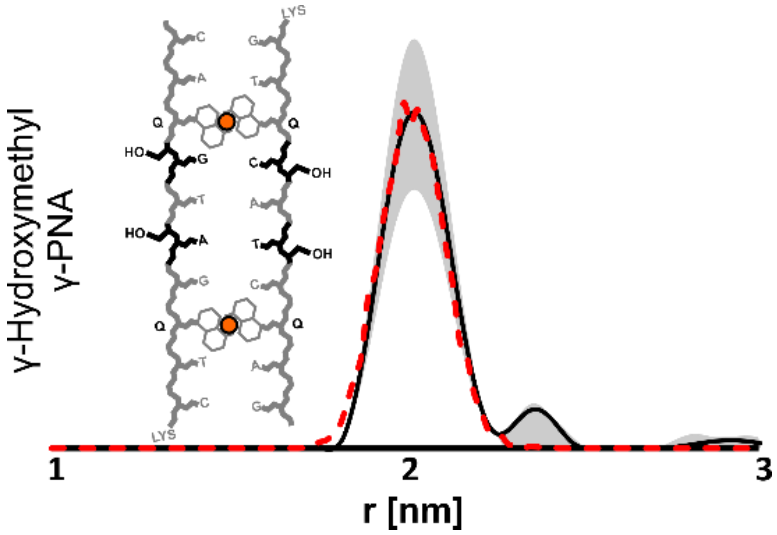

Figure 5-14 MD simulation results for γ-PNA. The distance distributions showing the Tikhonov regularized DEER distribution is shown in black with uncertainty analysis (gray shading). The MD Cu^{2+}-Cu^{2+} distribution is shown as a red dashed line.

Next, we analyzed the trajectories of both the U-PNA and γ-PNA to gain atomistic-level insight into the structures. To this end, we extracted all of the trajectory frames from the MD simulations from U-PNA and γ-PNA that displayed Cu^{2+}-Cu^{2+} distances within the ranges of 1.85-1.95 nm, 1.95-2.05 nm, and 2.05-2.15 nm (Figure 5-15). These distance ranges correspond to the shortest, most probable, and longest accessible CuQ_2-CuQ_2 distances from the DEER distributions, respectively. Each distance range contained 1000-4000 individual frames. Each set of structures was then averaged to produce a representative structure for each distance range. We analyzed and compared various helical parameters of these average structures from the core base pairs found between the CuQ_2 residues using 3DNA.[269] The average rise, or vertical displacement between base pairs, is noted next to each average structure in Figure 5-15. The average twist of each base pair in degrees is noted underneath each structure.

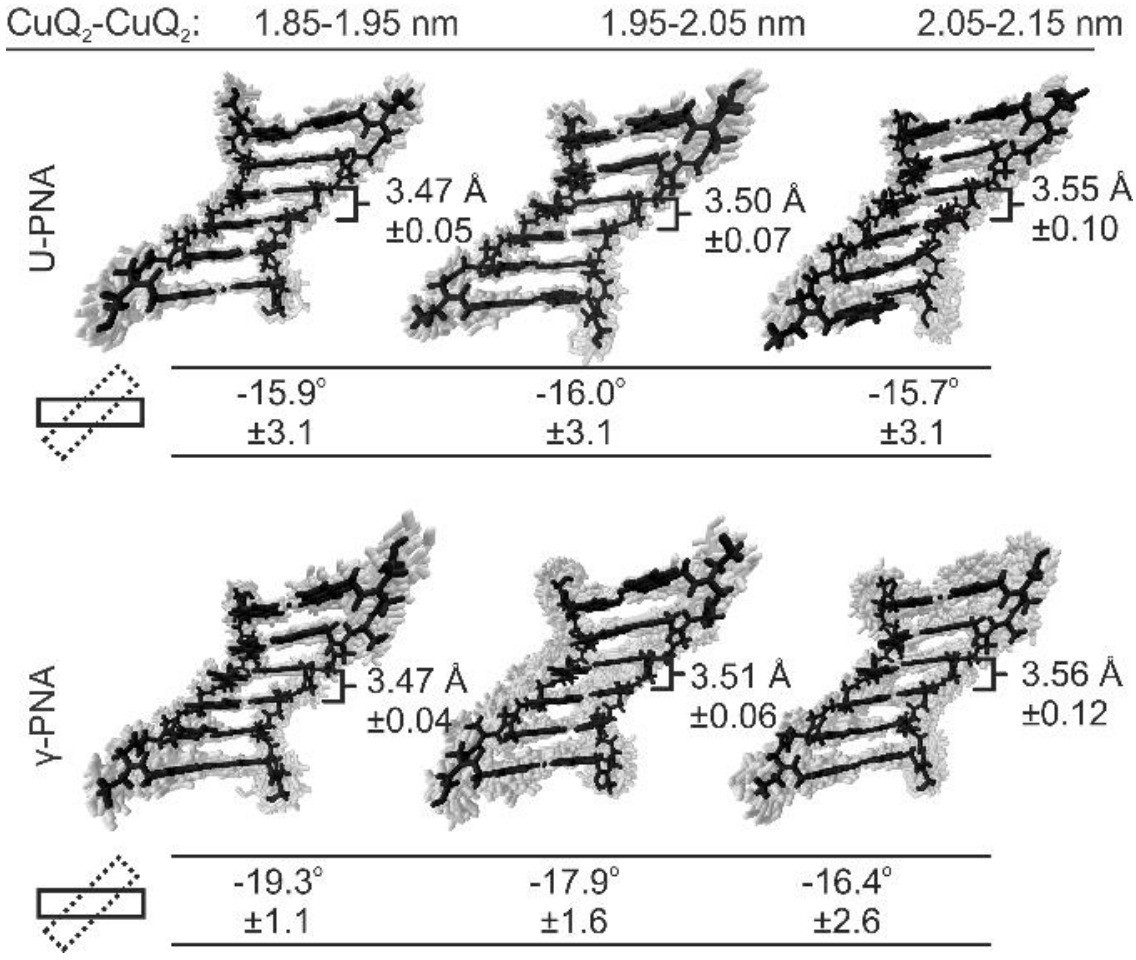

Figure 5-15 The average structure of U-PNA (top) and γ-PNA (bottom) taken from all frames of the MD simulation that had a CuQ_2-CuQ_2 distance in the range indicated above each structure. The average structure (black) is overlaid atop the individual frames comprising it (light gray). Noted alongside the structures are the average rises of the PNA base pairs (avg±s.d.). Underneath the structures are the average twist angles of the PNA duplex (avg±s.d.).[270]

This analysis reveals that there is little backbone fluctuation across all sampled PNA conformations, which is not surprising given the very narrow distance distribution revealed by the DEER signals. The average rise per base pair of both the U-PNA and the γ-PNA, in their most probable conformations, i.e. the one in which the CuQ_2-CuQ_2 distance is between 1.95-2.05 nm, is ~3.5 Å. The average rise per base pair calculated by the MD simulations agrees well with the value of 3.2 Å obtained by X-ray crystallography and NMR spectroscopy.[215] These results show that the overall double helical shape of the PNA is not affected by the addition of CuQ_2 groups. This conclusion is further supported by circular dichroism data, which shows a signal typical of double helical PNA (Figure 5-11).

Analysis of the twist angles revealed subtle differences between the conformations of the U-PNA and the γ-PNA. For the U-PNA, the average twist angle is the same in each distance range (within the standard deviation). For the γ-PNA, the average twist angle decreases and the corresponding standard deviation increases as the Cu^{2+}-Cu^{2+} distance increases. Also notable is that the standard deviations of the twist angles of the γ-PNA are lower than those of the U-PNA. This result indicates a narrower range of accessible conformations for the γ-PNA than for the U-PNA. Furthermore, the RMSD and root mean square fluctuation (RMSF) of the U-PNA compared to the γ-PNA are similar (Figure 5-16 and Figure 5-17, respectively).

These results suggest that the inclusion of sparse γ-modifications in the PNA backbone have subtle effects on the conformations of the PNA duplex, specifically with regard to the twist angles. The conformation of U-PNA vary mainly in the rise per base pair while the twist angles remain constant. The γ-PNA shows variations in both the rise of the base pairs and the twist of the helix.

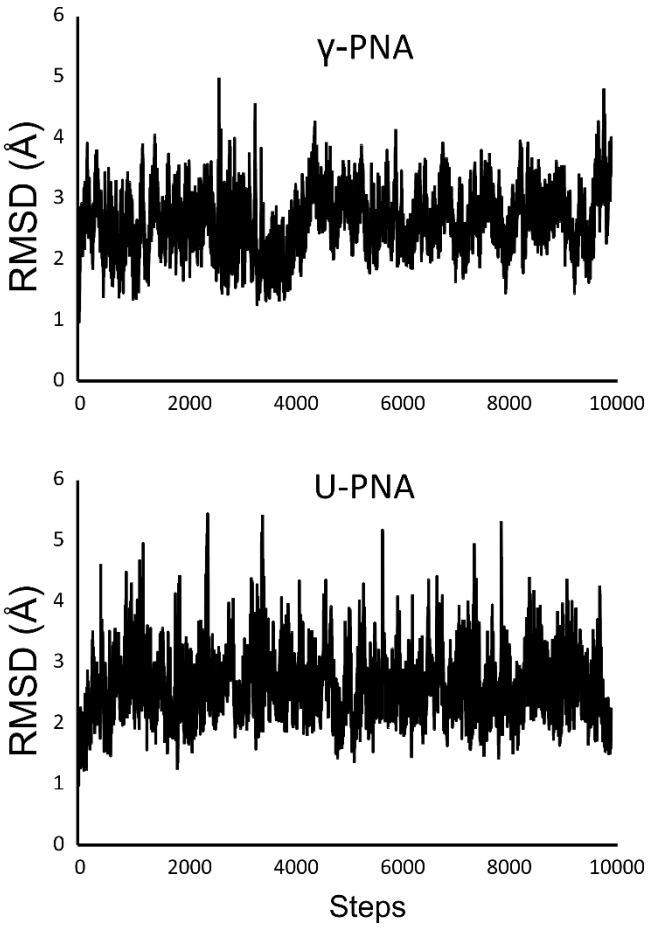

Figure 5-16 RMSD plots for U-PNA (top) and γ-PNA (bottom) for each point in the MD trajectory. RMSDs calculated in VMD.[258]

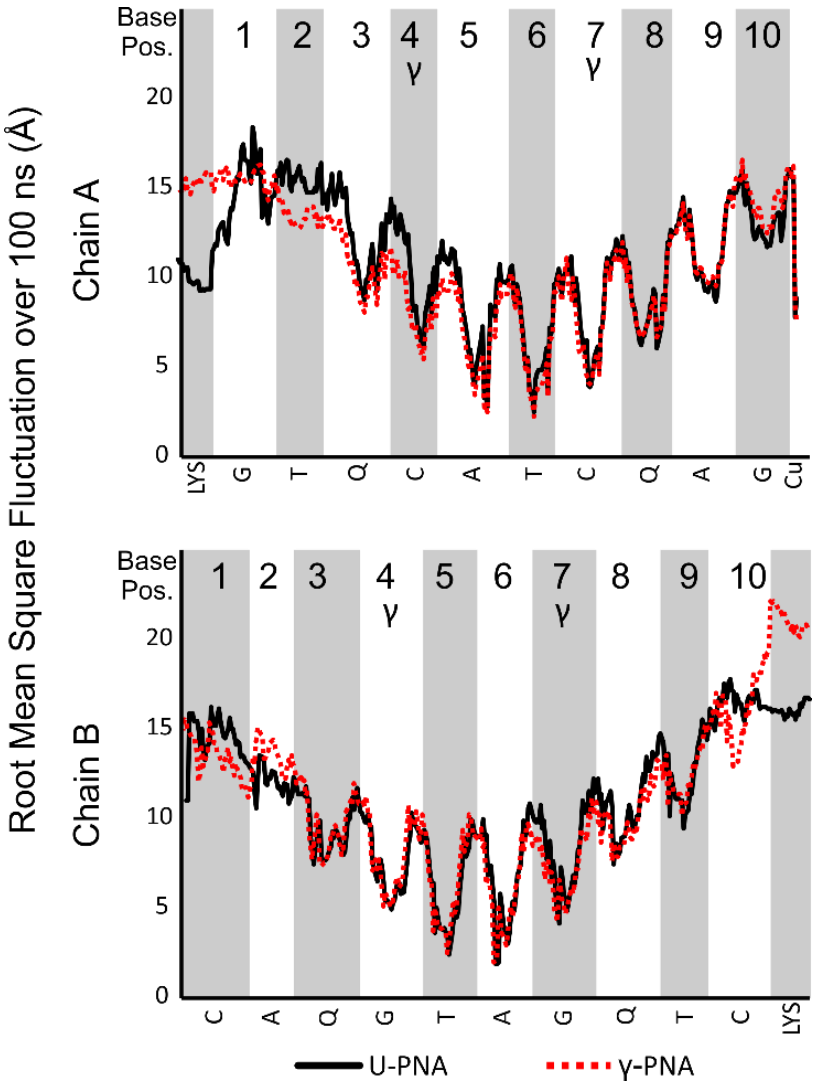

Figure 5-17 RMSF (root mean square fluctuation) of U-PNA (black line) compared with γ-PNA (dashed red line) for each nucleobase on both chains of the PNA duplexes. RMSFs calculated in VMD.[258]

5.4 Conclusion

We have measured for the first time distances between two Cu^{2+}-based spin labels within a PNA duplex by EPR. We found that the CuQ_2 spin labeling motif is efficient and effective for the measurement of distances within standard aeg-based PNA duplexes as well as within PNA duplexes with γ-modifications. We have developed MD force-field parameters which can be used to accurately simulate the PNA canonical nucleobases, a backbone with modifications, and CuQ_2 motif in the PNA. Such methods for the measurement of distances by EPR interpreted with the additional context of MD simulations have enabled us to gain an atomistic understanding of PNA structure. These advancements represent an important avenue for the elucidation of PNA conformational changes. Additionally, the atomistic information provided by MD coupled with the EPR results clearly demonstrates that small fluctuations in the Cu^{2+} coordination environment induced from the elasticity of Cu^{2+} binding leads to large distributions in g-tensor orientation, sufficient enough to "wash out" any orientational selectivity at X-band. Therefore, the Cu^{2+}-Cu^{2+} distance can be measured through a single experiment performed at $g_{\perp}$ at X-band frequencies despite the rigidity of the spin label. Overall, this development of EPR and MD methods expands the toolset available for the analysis and assessment of PNA's structure and conformations.

5.5 Acknowledgements

SS acknowledges NSF MCB-1613007. The EPR spectrometer was supported by NSF MRI-1725678 to S.S. CA acknowledges NSF support (CHE-1310441). JW acknowledges NIH support (R01-GM079383 and P30-DA035778). The Center for Molecular Analysis at Carnegie Mellon University was supported in part by the NSF (CHE-9808188 and DBI-9729351). All MD simulations were performed at the University of Pittsburgh's Center for Research Computing. We thank Dr. Marcela Madrid (Pittsburgh Supercomputing Center) for early discussions relating to the molecular dynamics parameterization. This chapter adapted with permission from reference 37. Copyright 2020 American Chemical Society.

6.0 Summary of Major Achievements

The work presented in this thesis marks a significant advancement in the application of Cu^{2+} labeling methodologies in biomolecules, specifically proteins. I have first shown a dramatic increase in the efficiency of the method through protocol optimization and an exploration of buffer effects on the labeling process, leading to a ~60% improvement compared to prior works. This advancement will aid in the widespread adoption of Cu^{2+} labeling in biophysics, and enable the collection of higher quality data. I have demonstrated the power of Cu^{2+} labeling in proteins through two specific means: the narrow distance distributions enable high precision in structural and conformational assessment, and the orientational information provided at higher frequencies provides an additional dimension of structural insight. Additionally, I have extended Cu^{2+} labeling techniques to synthetic nucleic acids by applying the same design principles that have led to high success in proteins. Through EPR experimentation and the molecular dynamics simulations, we have shown the fine level of structural insight we can gain from this label, and paved the way forward for nucleic acid labeling at large.

My research efforts have led to the following publications:

A. Gamble Jarvi, X. Bogetti, K. Singewald, S. Ghosh, and S. Saxena. “Going the dHis-tance: Site Directed Cu^{2+} Labeling of Proteins and Nucleic Acids for EPR Measurements.” (Under Review).

Z. M. Schulte, Y. H. Kwon, Y. Han, C. Liu, L. Li, Y. Yang, **A. Gamble Jarvi**, S. Saxena, G. Veser, J. K. Johnson, and N. L. Rosi. “H_2/CO_2 separations in multicomponent metal-adeninate

MOFs with multiple chemically distinct pore environments." *Chem. Sci.* **2020**, DOI: 10.1039/D0SC04979D.

A. Gamble Jarvi, J. Casto, and S. Saxena. "Buffer Effects on Site Directed Cu^{2+}-Labeling Using the Double Histidine Motif." *J. Magn. Reson.* **2020,** 320, 106848.

A. Gamble Jarvi, A. Sargun, X. Bogetti, J. Wang, C. Achim, and S. Saxena. "Development of Cu^{2+}-Based Distance Methods and Force Field Parameters for the Determination of PNA Conformations and Dynamics by EPR and MD Simulations." *J. Phys. Chem. B.* **2020,** 124, 7544. (This work highlighted as a supplementary journal cover).

X. Bogetti, S. Ghosh, **A. Gamble Jarvi**, J. Wang, and S. Saxena. "Molecular Dynamics Simulations Based on Newly Developed Force Field Parameters for Cu (II) Spin Labels Provide Insights into Double Histidine Based Double Electron Electron Resonance." *J. Phys. Chem. B.* **2020,** 124, 2788-2797. (This work highlighted as a supplementary journal cover).

M. H. Mohamed, Y. Yang, L. Li, S. Zhang, J. P. Ruffley, **A. Gamble Jarvi**, S. Saxena, G. Veser, K. J. Johnson, N. Rosi. "Designing Open Metal Sites in Metal-Organic Frameworks for Paraffin/Olefin Separations." *J. Am. Chem. Soc.* **2019**, 141, 13003.

A. Gamble Jarvi, T. F. Cunningham, and S. Saxena. "Efficient Localization of a Native Metal Ion within a Protein by Cu^{2+}-based EPR Distance Measurements." *Phys. Chem. Chem. Phys.* **2019**, 21, 10238-10243. (This work highlighted as a supplementary journal cover).

A. Gamble Jarvi, K. Ranguelova, S. Ghosh, R. T. Weber, and S. Saxena. "On the Use of Q-Band Double Electron–Electron Resonance to Resolve the Relative Orientations of Two Double Histidine-Bound Cu^{2+} Ions in a Protein." *J. Phys. Chem. B.* **2018,** 122, 10669–10677. (This work highlighted as a supplementary journal cover).

D. C. Kaseman, **A. Gamble Jarvi**, X. Y. Gan, S. Saxena, and J. E. Millstone. “Evolution of Surface Copper (II) Environments in $Cu_{2-x}Se$ Nanoparticles.” *Chem. Mat.* **2018,** 30, 7313–7321.

P. F. Muldoon, C. Liu, C. C. Miller, S. B. Koby, **A. Gamble Jarvi**, T. Y. Luo, S. Saxena, M. O’Keeffe, and N. Rosi. “Programmable Topology in New Families of Heterobimetallic Metal–Organic Frameworks.” *J. Am. Chem. Soc.* **2018,** 140, 6194-6198.

7.0 Bibliography

(1) Freed, J. H., The Development of High-Field /High Frequency ESR. In *Very High Frequency (Vhf) ESR/EPR*, Grinberg, O. Y.; Berliner, L. J., Eds. Springer US: Boston, MA, 2004; pp 19-43.

(2) Froncisz, W.; Hyde, J. S. The Loop-Gap Resonator: A New Microwave Lumped Circuit ESR Sample Structure. *J. Magn. Reson.* **1982,** *47*, 515-521.

(3) Spindler, P. E.; Schöps, P.; Kallies, W.; Glaser, S. J.; Prisner, T. F. Perspectives of Shaped Pulses for EPR Spectroscopy. *J. Magn. Reson.* **2017,** *280*, 30-45.

(4) Jeschke, G.; Chechik, V.; Ionita, P.; Godt, A.; Zimmermann, H.; Banham, J.; Timmel, C. R.; Hilger, D.; Jung, H. Deeranalysis2006—a Comprehensive Software Package for Analyzing Pulsed Eldor Data. *Appl. Magn. Reson.* **2006,** *30*, 473-498.

(5) Stoll, S.; Schweiger, A. Easyspin, a Comprehensive Software Package for Spectral Simulation and Analysis in EPR. *J. Magn. Reson.* **2006,** *178*, 42-55.

(6) Budil, D. E.; Lee, S.; Saxena, S.; Freed, J. H. Nonlinear-Least-Squares Analysis of Slow-Motion EPR Spectra in One and Two Dimensions Using a Modified Levenberg–Marquardt Algorithm. *J. Magn. Reson.* **1996,** *120*, 155-189.

(7) Carrington, A.; McLachlan, A. D. Introduction to Magnetic Resonance: With Applications to Chemistry and Chemical Physics. **1967**.

(8) Mims, W. B. Electron Echo Methods in Spin Resonance Spectrometry. *Rev. Sci. Instrum.* **1965,** *36*, 1472-1479.

(9) Gorcester, J.; Freed, J. H. Two-Dimensional Fourier Transform ESR Correlation Spectroscopy. *J. Chem. Phys.* **1988,** *88*, 4678-4693.

(10) Höfer, P.; Grupp, A.; Nebenführ, H.; Mehring, M. Hyperfine Sublevel Correlation (Hyscore) Spectroscopy: A 2d ESR Investigation of the Squaric Acid Radical. *Chem. Phys. Lett.* **1986,** *132*, 279-282.

(11) Saxena, S.; Freed, J. H. Double Quantum Two Dimensional Fourier Transform Electron Spin Resonance: Distance Measurements. *Chem. Phys. Lett.* **1996,** *262*, 17.

(12) Pannier, M.; Veit, S.; Godt, A.; Jeschke, G.; Spiees, H. W. Dead-Time Free Measurement of Dipole-Dipole Interactions between Electron Spins. *J. Magn. Reson.* **2000,** *142*, 331-340.

(13) Jeschke, G.; Pannier, M.; Godt, A.; Spiess, H. W. Dipolar Spectroscopy and Spin Alignment in Electron Paramagnetic Resonance. *Chem. Phys. Lett.* **2000,** *331*, 243-252.

(14) Milikisyants, S.; Scarpelli, F.; Finiguerra, M. G.; Ubbink, M.; Huber, M. A Pulsed EPR Method to Determine Distances between Paramagnetic Centers with Strong Spectral Anisotropy and Radicals: The Dead-Time Free Ridme Sequence. *J. Magn. Reson.* **2009,** *201*, 48-56.

(15) Hubbell, W.; Lopez, C.; Altenbach, C.; Yang, Z. Technological Advances in Site-Directed Spin Labeling of Proteins. *Curr. Opin. Struct. Biol.* **2013,** *23*, 725-733.

(16) Hubbell, W. L.; McHaourab, H. S.; Altenbach, C.; Lietzow, M. A. Watching Proteins Move Using Site-Directed Spin Labeling. *Structure* **1996,** *4*, 779-783.

(17) Cuello, L. G.; Cortes, D. M.; Perozo, E. Molecular Architecture of the Kvap Voltage-Dependent K+ Channel in a Lipid Bilayer. *Science* **2004,** *306*, 491-495.

(18) Endeward, B.; Butterwick, J. A.; MacKinnon, R.; Prisner, T. F. Pulsed Electron−Electron Double-Resonance Determination of Spin-Label Distances and Orientations on the Tetrameric Potassium Ion Channel Kcsa. *J. Am. Chem. Soc.* **2009,** *131*, 15246-15250.

(19) Singh, V.; Azarkh, M.; Exner, T. E.; Hartig, J. S.; Drescher, M. Human Telomeric Quadruplex Conformations Studied by Pulsed EPR. *Angew. Chem. Int. Ed.* **2009,** *48*, 9728-9730.

(20) Yang, Z.; Kurpiewski, M. R.; Ji, M.; Townsend, J. E.; Mehta, P.; Jen-Jacobson, L.; Saxena, S. ESR Spectroscopy Identifies Inhibitory Cu2+ Sites in a DNA-Modifying Enzyme to Reveal Determinants of Catalytic Specificity. *Proc. Natl. Acad. Sci.* **2012,** *109*, E993-E1000.

(21) Stone, K. M.; Townsend, J. E.; Sarver, J.; Sapienza, P. J.; Saxena, S.; Jen-Jacobson, L. Electron Spin Resonance Shows Common Structural Features for Different Classes of Ecori–DNA Complexes. *Angew. Chem. Int. Ed.* **2008,** *47*, 10192-10194.

(22) Grohmann, D.; Klose, D.; Klare, J. P.; Kay, C. W. M.; Steinhoff, H.-J.; Werner, F. Rna-Binding to Archaeal Rna Polymerase Subunits F/E: A Deer and Fret Study. *J. Am. Chem. Soc.* **2010,** *132*, 5954-5955.

(23) Wälti, M. A.; Schmidt, T.; Murray, D. T.; Wang, H.; Hinshaw, J. E.; Clore, G. M. Chaperonin Groel Accelerates Protofibril Formation and Decorates Fibrils of the Het-S Prion Protein. *Proc. Natl. Acad. Sci.* **2017,** *114*, 9104-9109.

(24) Dastvan, R.; Mishra, S.; Peskova, Y. B.; Nakamoto, R. K.; Mchaourab, H. S. Mechanism of Allosteric Modulation of P-Glycoprotein by Transport Substrates and Inhibitors. *Science* **2019,** *364*, 689-692.

(25) Galiano, L.; Bonora, M.; Fanucci, G. E. Interflap Distances in Hiv-1 Protease Determined by Pulsed EPR Measurements. *J. Am. Chem. Soc.* **2007,** *129*, 11004-11005.

(26) Samanta, D.; Borbat, P. P.; Dzikovski, B.; Freed, J. H.; Crane, B. R. Bacterial Chemoreceptor Dynamics Correlate with Activity State and Are Coupled over Long Distances. *Proc. Natl. Acad. Sci.* **2015,** *112*, 2455-2460.

(27) Böhm, S.; Licht, A.; Wuttge, S.; Schneider, E.; Bordignon, E. Conformational Plasticity of the Type I Maltose Abc Importer. *Proc. Natl. Acad. Sci.* **2013,** *110*, 5492-5497.

(28) Vileno, B.; Chamoun, J.; Liang, H.; Brewer, P.; Haldeman, B. D.; Facemyer, K. C.; Salzameda, B.; Song, L.; Li, H.-C.; Cremo, C. R., et al. Broad Disorder and the Allosteric Mechanism of Myosin II Regulation by Phosphorylation. *Proc. Natl. Acad. Sci.* **2011,** *108*, 8218-8223.

(29) Altenbach, C.; Kusnetzow, A. K.; Ernst, O. P.; Hofmann, K. P.; Hubbell, W. L. High-Resolution Distance Mapping in Rhodopsin Reveals the Pattern of Helix Movement Due to Activation. *Proc. Natl. Acad. Sci.* **2008,** *105*, 7439-7444.

(30) Sarver, J. L.; Townsend, J. E.; Rajapakse, G.; Jen-Jacobson, L.; Saxena, S. Simulating the Dynamics and Orientations of Spin Labeled Side Chains in a Protein-DNA Complex. *J. Phys. Chem. B.* **2012,** *116*, 4024.

(31) Sale, K.; Song, L.; Liu, Y.-S.; Perozo, E.; Fajer, P. Explicit Treatment of Spin Labels in Modeling of Distance Constraints from Dipolar EPR and Deer. *J. Am. Chem. Soc.* **2005,** *127*, 9334-9335.

(32) Cunningham, T. F.; Putterman, M. R.; Desai, A.; Horne, W. S.; Saxena, S. The Double-Histidine Cu2+-Binding Motif: A Highly Rigid, Site-Specific Spin Probe for Electron Spin Resonance Distance Measurements. *Angew. Chem., Int. Ed.* **2015,** *54*, 6330-6334.

(33) Lawless, M. J.; Ghosh, S.; Cunningham, T. F.; Shimshi, A.; Saxena, S. On the Use of the Cu2+–Iminodiacetic Acid Complex for Double Histidine Based Distance Measurements by Pulsed ESR. *Phys. Chem. Chem. Phys.* **2017,** *19*, 20959-20967.

(34) Ghosh, S.; Lawless, M. J.; Rule, G. S.; Saxena, S. The Cu2+-Nitrilotriacetic Acid Complex Improves Loading of A-Helical Double Histidine Site for Precise Distance Measurements by Pulsed ESR. *J. Magn. Res.* **2018,** *286*, 163-171.

(35) Wort, J. L.; Ackermann, K.; Giannoulis, A.; Stewart, A. J.; Norman, D. G.; Bode, B. E. Sub-Micromolar Pulse Dipolar EPR Spectroscopy Reveals Increasing Cuii-Labelling of Double-Histidine Motifs with Lower Temperature. *Angewandte Chemie International Edition* **2019,** *58*, 11681-11685.

(36) Gamble Jarvi, A.; Casto, J.; Saxena, S. Buffer Effects on Site Directed Cu2+-Labeling Using the Double Histidine Motif. *Journal of Magnetic Resonance* **2020,** *320*, 106848.

(37) Gamble Jarvi, A.; Sargun, A.; Bogetti, X.; Wang, J.; Achim, C.; Saxena, S. Development of Cu2+-Based Distance Methods and Force Field Parameters for the Determination of PNA Conformations and Dynamics by EPR and Md Simulations. *The Journal of Physical Chemistry B* **2020,** *124*, 7544-7556.

(38) Bernarducci, E.; Bharadwaj, P. K.; Krogh-Jespersen, K.; Potenza, J. A.; Schugar, H. J. Electronic Structure of Alkylated Imidazoles and Electronic Spectra of Tetrakis(Imidazole)Copper(II) Complexes. Molecular Structure of Tetrakis(1,4,5-Trimethylimidazole)Copper(II) Diperchlorate. *Journal of the American Chemical Society* **1983,** *105*, 3860-3866.

(39) Dikanov, S. A.; Tsvetkov, Y., *Electron Spin Echo Envelope Modulation (Eseem) Spectroscopy*. CRC press: 1992.

(40) Silva, K. I.; Michael, B. C.; Geib, S. J.; Saxena, S. Eseem Analysis of Multi-Histidine Cu(II)-Coordination in Model Complexes, Peptides, and Amyloid-B. *The Journal of Physical Chemistry B* **2014,** *118*, 8935-8944.

(41) Shin, B.-k.; Saxena, S. Substantial Contribution of the Two Imidazole Rings of the His13−His14 Dyad to Cu(II) Binding in Amyloid-B(1−16) at Physiological Ph and Its Significance. *The Journal of Physical Chemistry A* **2011,** *115*, 9590-9602.

(42) Kevan, L. Modulation of Electron Spin-Echo Decay in Solids. *Time Domain Electron Spin Resonance* **1979**, 279-341.

(43) Budil, D. E.; Lee, S.; Saxena, S.; Freed, J. H. Nonlinear-Least-Squares Analysis of Slow-Motion EPR Spectra in One and Two Dimensions Using a Modified Levenberg–Marquardt Algorithm. *Journal of Magnetic Resonance, Series A* **1996,** *120*, 155-189.

(44) Singewald, K.; Bogetti, X.; Sinha, K.; Rule, G.; Saxena, S. K. Double Histidine Based EPR Measurements at Physiological Temperatures Permit Site-Specific Elucidation of Hidden Dynamics in Enzymes. *Angewandte Chemie International Edition 10.1002/anie.202009982*.

(45) Zhan, Y.; Rule, G. S. Glutathione Induces Helical Formation in the Carboxy Terminus of Human Glutathione Transferase A1-1. *Biochemistry* **2004,** *43*, 7244-7254.

(46) Lawless, M. J.; Pettersson, J. R.; Rule, G. S.; Lanni, F.; Saxena, S. ESR Resolves the C Terminus Structure of the Ligand-Free Human Glutathione S-Transferase A1-1. *Biophys. J.* **2018,** *114*, 592-601.

(47) Jeschke, G. Mmm: A Toolbox for Integrative Structure Modeling. *Protein Science* **2018,** *27*, 76-85.

(48) Milov, A.; Maryasov, A.; Tsvetkov, Y. D. Pulsed Electron Double Resonance (Peldor) and Its Applications in Free-Radicals Research. *Applied Magnetic Resonance* **1998,** *15*, 107-143.

(49) Jeschke, G.; Pannier, M.; Godt, A.; Spiess, H. W. Dipolar Spectroscopy and Spin Alignment in Electron Paramagnetic Resonance. *Chemical Physics Letters* **2000,** *331*, 243-252.

(50) Kulik, L. V.; Grishin, Y. A.; Dzuba, S. A.; Grigoryev, I. A.; Klyatskaya, S. V.; Vasilevsky, S. F.; Tsvetkov, Y. D. Electron Dipole–Dipole Eseem in Field-Step Eldor of Nitroxide Biradicals. *J. Magn. Reson.* **2002,** *157*, 61-68.

(51) Milikisyants, S.; Scarpelli, F.; Finiguerra, M. G.; Ubbink, M.; Huber, M. A Pulsed EPR Method to Determine Distances between Paramagnetic Centers with Strong Spectral Anisotropy and Radicals: The Dead-Time Free Ridme Sequence. *Journal of Magnetic Resonance* **2009,** *201*, 48-56.

(52) van Amsterdam, I. M. C.; Ubbink, M.; Canters, G. W.; Huber, M. Measurement of a Cu□Cu Distance of 26 Å by a Pulsed EPR Method. *Angewandte Chemie International Edition* **2003,** *42*, 62-64.

(53) Yang, Z.; Becker, J.; Saxena, S. On Cu(II)-Cu(II) Distance Measurements Using Pulsed Electron Electron Double Resonance. *J. Magn. Reson.* **2007,** *188*, 337-343.

(54) Bowen, A. M.; Jones, M. W.; Lovett, J. E.; Gaule, T. G.; McPherson, M. J.; Dilworth, J. R.; Timmel, C. R.; Harmer, J. R. Exploiting Orientation-Selective Deer: Determining Molecular Structure in Systems Containing Cu(II) Centres. *Phys. Chem. Chem. Phys.* **2016,** *18*, 5981-5994.

(55) Breitgoff, F. D.; Keller, K.; Qi, M.; Klose, D.; Yulikov, M.; Godt, A.; Jeschke, G. Uwb Deer and Ridme Distance Measurements in Cu(II)–Cu(II) Spin Pairs. *Journal of Magnetic Resonance* **2019,** *308*, 106560.

(56) Becker, J. S.; Saxena, S. Double Quantum Coherence Electron Spin Resonance on Coupled Cu(II)-Cu(II) Electron Spins. *Chem. Phys. Lett.* **2005,** *414*, 248-252.

(57) Ruthstein, S.; Ji, M.; Mehta, P.; Jen-Jacobson, L.; Saxena, S. Sensitive Cu2+-Cu2+ Distance Measurements in a Protein-DNA Complex by Dqc ESR. *J. Phys. Chem. B.* **2013,** *117*, 6227-6230.

(58) Ruthstein, S.; Ji, M.; Shin, B.-k.; Saxena, S. A Simple Double Quantum Coherence ESR Sequence That Minimizes Nuclear Modulations in Cu 2+-Ion Based Distance Measurements. *Journal of Magnetic Resonance* **2015,** *257*, 45-50.

(59) Sameach, H.; Ghosh, S.; Gevorkyan-Airapetov, L.; Saxena, S.; Ruthstein, S. EPR Spectroscopy Detects Various Active State Conformations of the Transcriptional Regulator Cuer. *Angewandte Chemie International Edition* **2019,** *58*, 3053-3056.

(60) Lawless, M. J.; Pettersson, J. R.; Rule, G. S.; Lanni, F.; Saxena, S. ESR Resolves the C Terminus Structure of the Ligand-Free Human Glutathione S-Transferase A1-1. *Biophysical Journal* **2018,** *114*, 592-601.

(61) Finkelstein, J. Metalloproteins. *Nature* **2009,** *460*, 813-813.

(62) Gamble Jarvi, A.; Cunningham, T. F.; Saxena, S. Efficient Localization of a Native Metal Ion within a Protein by Cu2+-Based EPR Distance Measurements. *Physical Chemistry Chemical Physics* **2019,** *21*, 10238-10243.

(63) Abdullin, D.; Florin, N.; Hagelueken, G.; Schiemann, O. EPR-Based Approach for the Localization of Paramagnetic Metal Ions in Biomolecules. *Angew. Chem. Int. Ed.* **2015,** *54*, 1827-1831.

(64) Gaffney, Betty J.; Bradshaw, Miles D.; Frausto, Stephen D.; Wu, F.; Freed, Jack H.; Borbat, P. Locating a Lipid at the Portal to the Lipoxygenase Active Site. *Biophys. J.* **2012,** *103*, 2134-2144.

(65) Gamble Jarvi, A.; Ranguelova, K.; Ghosh, S.; Weber, R. T.; Saxena, S. On the Use of Q-Band Double Electron–Electron Resonance to Resolve the Relative Orientations of Two Double Histidine-Bound Cu2+ Ions in a Protein. *J. Phys. Chem. B* **2018,** *122*, 10669-10677.

(66) Bogetti, X.; Ghosh, S.; Gamble Jarvi, A.; Wang, J.; Saxena, S. Molecular Dynamics Simulations Based on Newly Developed Force Field Parameters for Cu2+ Spin Labels Provide Insights into Double-Histidine-Based Double Electron–Electron Resonance. *J. Phys. Chem. B* **2020,** *124*, 2788-2797.

(67) Neese, F. The Orca Program System. *WIREs Comput. Mol. Sci.* **2012,** *2*, 73-78.

(68) Neese, F. Software Update: The Orca Program System, Version 4.0. *WIREs Comput. Mol. Sci.* **2018,** *8*, e1327.

(69) Ghosh, S.; Saxena, S.; Jeschke, G. Rotamer Modelling of Cu(II) Spin Labels Based on the Double-Histidine Motif. *Applied Magnetic Resonance* **2018,** *49*, 1287-1298.

(70) Atwell, S.; Meggers, E.; Spraggon, G.; Schultz, P. G. Structure of a Copper-Mediated Base Pair in DNA. *Journal of the American Chemical Society* **2001,** *123*, 12364-12367.

(71) Wittung, P.; Nielsen, P. E.; Buchardt, O.; Egholm, M.; Norde´n, B. DNA-Like Double Helix Formed by Peptide Nucleic Acid. *Nature* **1994,** *368*, 561-563.

(72) Jensen, K. K.; Ørum, H.; Nielsen, P. E.; Nordén, B. Kinetics for Hybridization of Peptide Nucleic Acids (PNA) with DNA and Rna Studied with the Biacore Technique. *Biochemistry* **1997,** *36*, 5072-5077.

(73) WILLIAMS, R. J. P. Metal Ions in Biological Systems. *Biological Reviews* **1953,** *28*, 381-412.

(74) Ferreira, C. M. H.; Pinto, I. S. S.; Soares, E. V.; Soares, H. M. V. M. (Un)Suitability of the Use of Ph Buffers in Biological, Biochemical and Environmental Studies and Their Interaction with Metal Ions – a Review. *RSC Advances* **2015,** *5*, 30989-31003.

(75) Mehlenbacher, M. R.; Bou-Abdallah, F.; Liu, X. X.; Melman, A. Calorimetric Studies of Ternary Complexes of Ni(II) and Cu(II) Nitrilotriacetic Acid and N-Acetyloligohistidines. *Inorganica Chimica Acta* **2015,** *437*, 152-158.

(76) Cunningham, T. F.; McGoff, M. S.; Sengupta, I.; Jaroniec, C. P.; Horne, W. S.; Saxena, S. High-Resolution Structure of a Protein Spin-Label in a Solvent-Exposed B-Sheet and Comparison with Deer Spectroscopy. *Biochemistry* **2012,** *51*, 6350-6359.

(77) Cunningham, T. F.; Pornsuwan, S.; Horne, W. S.; Saxena, S. Rotameric Preferences of a Protein Spin Label at Edge-Strand B-Sheet Sites. *Protein Science* **2016,** *25*, 1049-1060.

(78) Stoll, S.; Schweiger, A. Easyspin, a Comprehensive Software Package for Spectral Simulation and Analysis in EPR. *J. Magn. Res.* **2006,** *178*, 42-55.

(79) Mims, W. B. Envelope Modulation in Spin-Echo Experiments. *Physical Review B* **1972,** *5*, 2409-2419.

(80) Fauth, J. M.; Schweiger, A.; Braunschweiler, L.; Forrer, J.; Ernst, R. R. Elimination of Unwanted Echoes and Reduction of Dead Time in Three-Pulse Electron Spin-Echo Spectroscopy. *Journal of Magnetic Resonance (1969)* **1986,** *66*, 74-85.

(81) Harju, L.; Sara, R. Spectrophotometric Titrations of Nitrilotriacetic Acid with Copper(II) as Monoligand and Biligand Chelates. *Analytica Chimica Acta* **1974,** *73*, 129-139.

(82) Sergienko, V. S. Specific Structural Features of Copper(II) Complexonates with Nitrilotriacetate Anions: A Review. *Crystallography Reports* **2006,** *51*, 236-257.

(83) Peisach, J.; Blumberg, W. E. Structural Implications Derived from the Analysis of EPR Spectra of Natural and Artificial Copper Proteins. *Arch. Biochem. Biophys.* **1974,** *195*, 691-708.

(84) Anderegg, G. Critical Survey of Stability Constants of Nta Complexes. **1982,** *54*, 2693.

(85) Sjöberg, S. Critical Evaluation of Stability Constants of Metal-Imidazole and Metal-Histamine Systems (Technical Report). **1997,** *69*, 1549.

(86) Pyreu, D.; Bazanova, M. Thermodynamics of Mixed-Ligand Complex Formation of Metal (II) Complexonates with Imidazole in Aqueous Solution. *Inorganica Chimica Acta* **2016,** *453*, 687-691.

(87) Thordarson, P. Determining Association Constants from Titration Experiments in Supramolecular Chemistry. *Chemical Society Reviews* **2011,** *40*, 1305-1323.

(88) Webb, J. E. A.; Crossley, M. J.; Turner, P.; Thordarson, P. Pyromellitamide Aggregates and Their Response to Anion Stimuli. *Journal of the American Chemical Society* **2007,** *129*, 7155-7162.

(89) Yang, Z.; Ji, M.; Saxena, S. Practical Aspects of Copper Ion-Based Double Electron Electron Resonance Distance Measurements. *Appl. Magn. Reson.* **2010,** *39*, 487-500.

(90) Borbat, P. P.; Freed, J. H., Pulse Dipolar Electron Spin Resonance: Distance Measurements. In *Structural Information from Spin-Labels and Intrinsic Paramagnetic Centers in the Biosciences. Structure and Bonding.*, Timmel, C. R.; Harmer, J. R., Eds. Springer: New York, USA, 2013; pp 1-82.

(91) Bologni, L.; Sabatini, A.; Vacca, A. Complex Formation Equilibria between 2-Amino-2(Hydroxymethyl)-1,3,-Propanediol (Tris, Tham) and Nickel(II), Copper(II), Zinc(II) and Hydrogen Ions in Aqueous Solutions. *Inorganica Chimica Acta* **1983,** *69*, 71-75.

(92) Anwar, Z. M.; Azab, H. A. Ternary Complexes in Solution. Comparison of the Coordination Tendency of Some Biologically Important Zwitterionic Buffers toward the Binary Complexes of Some Transition Metal Ions and Some Amino Acids. *Journal of Chemical & Engineering Data* **1999,** *44*, 1151-1157.

(93) Powell, K. J.; Brown, P. L.; Byrne, R. H.; Gajda, T.; Hefter, G.; Sjöberg, S.; Wanner, H. Chemical Speciation of Environmentally Significant Metals with Inorganic Ligands Part 2: The Cu2+-Oh-, Cl-, Co32-, So42-, and Po43- Systems (Iupac Technical Report). **2007,** *79*, 895.

(94) Ward, R.; Zoltner, M.; Beer, L.; El Mkami, H.; Henderson, I. R.; Palmer, T.; Norman, D. G. The Orientation of a Tandem Potra Domain Pair, of the Beta-Barrel Assembly Protein Bama, Determined by Peldor Spectroscopy. *Structure* **2009,** *17*, 1187-1194.

(95) Georgieva, E. R.; Borbat, P. P.; Ginter, C.; Freed, J. H.; Boudker, O. Conformational Ensemble of the Sodium-Coupled Aspartate Transporter. *Nat. Struct. Mol. Biol.* **2013,** *20*, 215.

(96) Hänelt, I.; Wunnicke, D.; Bordignon, E.; Steinhoff, H.-J.; Slotboom, D. J. Conformational Heterogeneity of the Aspartate Transporter Gltph. *Nat. Struct. Mol. Biol.* **2013,** *20*, 210.

(97) Dalmas, O.; Sompornpisut, P.; Bezanilla, F.; Perozo, E. Molecular Mechanism of Mg2+-Dependent Gating in Cora. *Nat. Commun.* **2014,** *5*, 3590.

(98) Liu, Z.; Casey, T. M.; Blackburn, M. E.; Huang, X.; Pham, L.; de Vera, I. M. S.; Carter, J. D.; Kear-Scott, J. L.; Veloro, A. M.; Galiano, L., et al. Pulsed EPR Characterization of Hiv-1 Protease Conformational Sampling and Inhibitor-Induced Population Shifts. *Physical Chemistry Chemical Physics* **2016,** *18*, 5819-5831.

(99) Grytz, C. M.; Marko, A.; Cekan, P.; Sigurdsson, S. T.; Prisner, T. F. Flexibility and Conformation of the Cocaine Aptamer Studied by Peldor. *Phys. Chem. Chem. Phys.* **2016,** *18*, 2993-3002.

(100) Verhalen, B.; Dastvan, R.; Thangapandian, S.; Peskova, Y.; Koteiche, H. A.; Nakamoto, R. K.; Tajkhorshid, E.; McHaourab, H. S. Energy Transduction and Alternating Access of the Mammalian Abc Transporter P-Glycoprotein. *Nature* **2017,** *543*, 738.

(101) Assafa, T. E.; Anders, K.; Linne, U.; Essen, L.-O.; Bordignon, E. Light-Driven Domain Mechanics of a Minimal Phytochrome Photosensory Module Studied by EPR. *Structure* **2018,** *26*, 1534-1545.e4.

(102) Fajer, P. G. Site Directed Spin Labelling and Pulsed Dipolar Electron Paramagnetic Resonance (Double Electron–Electron Resonance) of Force Activation in Muscle. *Journal of Physics: Condensed Matter* **2005,** *17*, S1459.

(103) López, C. J.; Yang, Z.; Altenbach, C.; Hubbell, W. L. Conformational Selection and Adaptation to Ligand Binding in T4 Lysozyme Cavity Mutants. *Proceedings of the National Academy of Sciences of the United States of America* **2013,** *110*, E4306-E4315.

(104) Park, S.-Y.; Borbat, P. P.; Gonzalez-Bonet, G.; Bhatnagar, J.; Pollard, A. M.; Freed, J. H.; Bilwes, A. M.; Crane, B. R. Reconstruction of the Chemotaxis Receptor-Kinase Assembly. *Nat. Struct. Mol. Biol.* **2006,** *13*, 400-407.

(105) Hanson, S. M.; Dawson, E. S.; Francis, D. J.; Van Eps, N.; Klug, C. S.; Hubbell, W. L.; Meiler, J.; Gurevich, V. V. A Model for the Solution Structure of the Rod Arrestin Tetramer. *Structure* **2008,** *16*, 924-934.

(106) DeBerg, Hannah A.; Bankston, John R.; Rosenbaum, Joel C.; Brzovic, Peter S.; Zagotta, William N.; Stoll, S. Structural Mechanism for the Regulation of Hcn Ion Channels by the Accessory Protein Trip8b. *Structure* **2015,** *23*, 734-744.

(107) Valera, S.; Ackermann, K.; Pliotas, C.; Huang, H.; Naismith, J. H.; Bode, B. E. Accurate Extraction of Nanometer Distances in Multimers by Pulse EPR. *Chemistry – A European Journal* **2016,** *22*, 4700-4703.

(108) Dawidowski, D.; Cafiso, David S. Munc18-1 and the Syntaxin-1 n Terminus Regulate Open-Closed States in a T-Snare Complex. *Structure* **2016,** *24*, 392-400.

(109) Milikisiyants, S.; Wang, S.; Munro, R. A.; Donohue, M.; Ward, M. E.; Bolton, D.; Brown, L. S.; Smirnova, T. I.; Ladizhansky, V.; Smirnov, A. I. Oligomeric Structure of Anabaena Sensory Rhodopsin in a Lipid Bilayer Environment by Combining Solid-State NMR and Long-Range Deer Constraints. *Journal of Molecular Biology* **2017,** *429*, 1903-1920.

(110) Stone, K. M.; Townsend, J. E.; Sarver, J.; Sapienza, P. J.; Saxena, S.; Jen-Jacobson, L. Electron Spin Resonance Shows Common Structural Features for Different Classes of Ecori-DNA Complexes. *Angew. Chem. Int. Ed.* **2008,** *47*, 10192-10194.

(111) Duss, O.; Yulikov, M.; Jeschke, G.; Allain, F. H. EPR-Aided Approach for Solution Structure Determination of Large Rnas or Protein-Rna Complexes. *Nat. Commun.* **2014,** *5*, 3669.

(112) Sameach, H.; Narunsky, A.; Azoulay-Ginsburg, S.; Gevorkyan-Aiapetov, L.; Zehavi, Y.; Moskovitz, Y.; Juven-Gershon, T.; Ben-Tal, N.; Ruthstein, S. Structural and Dynamics Characterization of the Merr Family Metalloregulator Cuer in Its Repression and Activation States. *Structure* **2017,** *25*, 988-996.

(113) Upadhyay, A. K.; Borbat, P. P.; Wang, J.; Freed, J. H.; Edmondson, D. E. Determination of the Oligomeric States of Human and Rat Monoamine Oxidases in the Outer Mitochondrial Membrane and Octyl B-D-Glucopyranoside Micelles Using Pulsed Dipolar Electron Spin Resonance Spectroscopy. *Biochemistry* **2008,** *47*, 1554-1566.

(114) Yin, D. M.; Hannam, J. S.; Schmitz, A.; Schiemann, O.; Hagelueken, G.; Famulok, M. Studying the Conformation of a Receptor Tyrosine Kinase in Solution by Inhibitor-Based Spin Labeling. *Angew. Chem. Int. Ed.* **2017,** *56*, 8417-8421.

(115) Steed, P. R.; Stein, R. A.; Mishra, S.; Goodman, M. C.; McHaourab, H. S. Na+–Substrate Coupling in the Multidrug Antiporter Norm Probed with a Spin-Labeled Substrate. *Biochemistry* **2013,** *52*, 5790-5799.

(116) Yang, Z.; Kurpiewski, M. R.; Ji, M.; Townsend, J. E.; Mehta, P.; Jen-Jacobson, L.; Saxena, S. ESR Spectroscopy Identifies Inhibitory Cu^{2+} Sites in a DNA-Modifying Enzyme to Reveal Determinants of Catalytic Specificity. *Proc. Natl. Acad. Sci. USA* **2012,** *109*, E993-1000.

(117) Evans, Eric G. B.; Pushie, M. J.; Markham, Kate A.; Lee, H.-W.; Millhauser, Glenn L. Interaction between Prion Protein's Copper-Bound Octarepeat Domain and a Charged C-Terminal Pocket Suggests a Mechanism for N-Terminal Regulation. *Structure* **2016,** *24*, 1057-1067.

(118) Borbat, P. P.; Freed, J. H. Multiple Quantum ESR and Distance Measurements. *Chem. Phys. Lett.* **1999,** *313*, 145-154.

(119) Bonora, M.; Becker, J.; Saxena, S. Suppression of Electron Spin-Echo Envelope Modulation Peaks in Double Quantum Coherence Electron Spin Resonance. *Journal of Magnetic Resonance* **2004,** *170*, 278-83.

(120) Kulik, L. V.; Dzuba, S. A.; Grigoryev, I. A.; Tsvetkov, Y. D. Electron Dipole–Dipole Interaction in Eseem of Nitroxide Biradicals. *Chemical Physics Letters* **2001,** *343*, 315-324.

(121) Ghosh, S.; Saxena, S.; Jeschke, G. Rotamer Modelling of Cu(II) Spin Labels Based on the Double-Histidine Motif. *Applied Magnetic Resonance* **2018,** *[Online early access]. DOI: 10.1007/s00723-018-1052-8. Published Online: Aug 16, 2018. https://link.springer.com/article/10.1007%2Fs00723-018-1052-8 (accessed Aug 16, 2018).*

(122) Hagelueken, G.; Abdullin, D.; Ward, R.; Schiemann, O. Mtsslsuite: In Silico Spin Labelling, Trilateration and Distance-Constrained Rigid Body Docking in Pymol. *Mol. Phys.* **2013,** *111*, 2757-2766.

(123) Gronenborn, A. M.; Filpula, D. R.; Essig, N. Z.; Achari, A.; Whitlow, M.; Wingfield, P. T.; Clore, G. M. A Novel, Highly Stable Fold of the Immunoglobulin Binding Domain of Streptococcal Protein G. *Science* **1991,** *253*, 657-661.

(124) Nadaud, P. S.; Sengupta, I.; Helmus, J. J.; Jaroniec, C. P. Evaluation of the Influence of Intermolecular Electron-Nucleus Couplings and Intrinsic Metal Binding Sites on the Measurement of 15 N Longitudinal Paramagnetic Relaxation Enhancements in Proteins by Solid-State NMR. *J. Biol. NMR* **2011,** *51*, 293.

(125) Wylie, B. J.; Sperling, L. J.; Nieuwkoop, A. J.; Franks, W. T.; Oldfield, E.; Rienstra, C. M. Ultrahigh Resolution Protein Structures Using NMR Chemical Shift Tensors. *Proc. Natl. Acad. Sci. USA* **2011,** *108*, 16974-16979.

(126) Syme, C. D.; Nadal, R. C.; Rigby, S. E. J.; Viles, J. H. Copper Binding to the Amyloid-B (Ab) Peptide Associated with Alzheimer's Disease. *J. Biol. Chem.* **2004,** *279*, 18169-18177.

(127) Yang, Z.; Kise, D.; Saxena, S. An Approach Towards the Measurement of Nanometer Range Distance Based on Cu2+ Ions and ESR. *J. Phys. Chem. B* **2010,** *114*, 6165-6174.

(128) Tainer, J. A.; Roberts, V. A.; Getzoff, E. D. Metal-Binding Sites in Proteins. *Curr. Opin. Biotechnol.* **1991,** *2*, 582-591.

(129) McCracken, J.; Vassiliev, I. R.; Yang, E.-C.; Range, K.; Barry, B. A. Eseem Studies of Peptide Nitrogen Hyperfine Coupling in Tyrosyl Radicals and Model Peptides. *J. Phys. Chem. B* **2007,** *111*, 6586-6592.

(130) Cammack, R.; Chapman, A.; McCracken, J.; Cornelius, J. B.; Peisach, J.; Weiner, J. H. Electron Spin-Echo Spectroscopic Studies of Escherichia Coli Fumarate Reductase. *Biochim. Biophys. Acta, Protein Struct. Mol. Enzymol.* **1988,** *956*, 307-312.

(131) Jeschke, G. Deer Distance Measurements on Proteins. *Annual review of physical chemistry* **2012,** *63*, 419-446.

(132) Schmidt, T.; Wälti, M. A.; Baber, J. L.; Hustedt, E. J.; Clore, G. M. Long Distance Measurements up to 160 Å in the Groel Tetradecamer Using Q-Band Deer EPR Spectroscopy. *Angewandte Chemie* **2016,** *128*, 16137-16141.

(133) Ji, M.; Ruthstein, S.; Saxena, S. Paramagnetic Metal Ions in Pulsed ESR Distance Distribution Measurements. *Accounts of Chemical Research* **2014,** *47*, 688-695.

(134) Schiemann, O.; Prisner, T. F. Long-Range Distance Determinations in Biomacromolecules by EPR Spectroscopy. *Quarterly reviews of biophysics* **2007,** *40*, 1-53.

(135) Berliner, L. J.; Eaton, S. S.; Eaton, G. R., *Distance Measurements in Biological Systems by EPR*. Springer Science & Business Media: 2006; Vol. 19.

(136) Reginsson, G. W.; Schiemann, O. Pulsed Electron-Electron Double Resonance: Beyond Nanometre Distance Measurements on Biomacromolecules. *Biochem. J.* **2011,** *434*, 353-363.

(137) Chakrapani, S. EPR Studies of Gating Mechanisms in Ion Channels. *Methods. Enzymol*. **2015,** *557*, 279-306.

(138) Cafiso, D. S. Identifying and Quantitating Conformational Exchange in Membrane Proteins Using Site-Directed Spin Labeling. *Acc. Chem. Res* **2014,** *47*, 3102-3109.

(139) Glaenzer, J.; Peter, M. F.; Hagelueken, G. Studying Structure and Function of Membrane Proteins with Peldor/Deer Spectroscopy – a Crystallographers' Perspective. *Methods* **2018,** *147*, 163-175.

(140) Stone, K. M.; Townsend, J. E.; Sarver, J.; Sapienza, P. J.; Saxena, S.; Jen-Jacobson, L. Electron Spin Resonance Shows Common Structural Features for Different Classes of Ecori–DNA Complexes. *Angewandte Chemie* **2008,** *120*, 10346-10348.

(141) Jeschke, G.; Y, P. Distance Measurements on Spin-Labelled Biomacromolecules by Pulsed Electron Paramagnetic Resonance. *Phys. Chem. Chem. Phys.* **2007,** *9*, 1895-1910.

(142) Haugland, M. M.; Lovett, J. E.; Anderson, E. A. Advances in the Synthesis of Nitroxide Radicals for Use in Biomolecule Spin Labelling. *Chemical Society Reviews* **2018,** *47*, 668-680.

(143) Roser, P.; Schmidt, M. J.; Drescher, M.; Summerer, D. Site-Directed Spin Labeling of Proteins for Distance Measurements in Vitro and in Cells. *Org. Biomol. Chem.* **2016,** *14*, 5468-5476.

(144) Shelke, S. A.; Sigurdsson, S. T., Site-Directed Spin Labeling for EPR Studies of Nucleic Acids. In *Modified Nucleic Acids*, Nakatani, K.; Tor, Y., Eds. Springer International Publishing: Cham, 2016; pp 159-187.

(145) Jeschke, G. Conformational Dynamics and Distribution of Nitroxide Spin Labels. *Prog. Nuc. Magn. Reson. Spec.* **2013,** *72*, 42-60.

(146) Polyhach, Y.; Bordignon, E.; Jeschke, G. Rotamer Libraries of Spin Labeled Cysteines for Protein Studies. *Phys. Chem. Chem. Phys.* **2011,** *13*, 2356-2366.

(147) Columbus, L.; Kalai, T.; Jeko, J.; Hideg, K.; Hubbell, W. Molecular Motion of Spin Labeled Side Chains in Alpha-Helices: Analysis by Variation of Side Chain Structure. *Biochemistry* **2001,** *40*, 3828-3846.

(148) Fawzi, N. L.; Fleissner, M. R.; Anthis, N. J.; Kálai, T.; Hideg, K.; Hubbell, W. L.; Clore, G. M. A Rigid Disulfide-Linked Nitroxide Side Chain Simplifies the Quantitative Analysis of Pre Data. *Journal of biomolecular NMR* **2011,** *51*, 105.

(149) Fleissner, M. R.; Bridges, M. D.; Brooks, E. K.; Cascio, D.; Kálai, T.; Hideg, K.; Hubbell, W. L. Structure and Dynamics of a Conformationally Constrained Nitroxide Side Chain

and Applications in EPR Spectroscopy. *Proceedings of the National Academy of Sciences* **2011,** *108*, 16241-16246.

(150) Warshaviak, D. T.; Khramtsov, V. V.; Cascio, D.; Altenbach, C.; Hubbell, W. L. Structure and Dynamics of an Imidazoline Nitroxide Side Chain with Strongly Hindered Internal Motion in Proteins. *Journal of Magnetic Resonance* **2013,** *232*, 53-61.

(151) Keller, K.; Zalibera, M.; Qi, M.; Koch, V.; Wegner, J.; Hintz, H.; Godt, A.; Jeschke, G.; Savitsky, A.; Yuliko, M. EPR Characterization of Mn(II) Complexes for Distance Determination with Pulsed Dipolar Spectroscopy. *Phys. Chem. Chem. Phys.* **2016,** *18*, 25120-25135.

(152) Akhmetzyanov, D.; Plackmeyer, J.; Endeward, B.; Denysenkov, V.; Prisner, T. F. Pulsed Electron–Electron Double Resonance Spectroscopy between a High-Spin Mn2+ Ion and a Nitroxide Spin Label. *Phys. Chem. Chem. Phys.* **2015,** *17*, 6760-6766.

(153) Yulikov, M.; Lueders, P.; Warsi, M. F.; Chechik, V.; Jeschke, G. Distance Measurements in Au Nanoparticles Functionalized with Nitroxide Radicals and Gd3+–Dtpa Chelate Complexes. *Phys. Chem. Chem. Phys.* **2012,** *14*, 10732-10746.

(154) Mascali, F. C.; Ching, H. Y. V.; Rasia, R. M.; Un, S.; Tabares, L. Using Genetically Encodable Self-Assembling GdIII Spin Labels to Make in-Cell Nanometric Distance Measurements. *Angew. Chem.* **2016,** *128*, 11207-11209.

(155) Doll, A.; Qi, M.; Wili, N.; Pribitzer, S.; Godt, A.; Jeschke, G. Gd(III)–Gd(III) Distance Measurements with Chirp Pump Pulses. *Journal of Magnetic Resonance* **2015,** *259*, 153-162.

(156) Barthelmes, D.; Gränz, M.; Barthelmes, K.; Allen, K. N.; Imperiali, B.; Prisner, T.; Schwalbe, H. Encoded Loop-Lanthanide-Binding Tags for Long-Range Distance Measurements in Proteins by NMR and EPR Spectroscopy. *J. Biomol. NMR* **2015,** *63*, 275-282.

(157) Goldfarb, D. Gd3+ Spin Labeling for Distance Measurements by Pulse EPR Spectroscopy. *Phys. Chem. Chem. Phys.* **2014,** *16*, 9685-9699.

(158) Banerjee, D.; Yagi, H.; Huber, T.; Otting, G.; Goldfarb, D. Nanometer-Range Distance Measurement in a Protein Using Mn2+ Tags. *J. Phys. Chem. Lett.* **2012,** *3*, 157-160.

(159) Yang, Z.; Ji, M.; Cunningham, T. F.; Saxena, S. Cu(II) as an ESR Probe of Protein Structure and Function. *Methods. Enzymol.* **2015,** *563*, 459.

(160) Cunningham, T. F.; Shannon, M. D.; Putterman, M. R.; Arachchige, R. J.; Sengupta, I.; Gao, M.; Jaroniec, C. P.; Saxena, S. Cysteine-Specific Cu2+ Chelating Tags Used as Paramagnetic Probes in Double Electron Electron Resonance. *J. Phys. Chem. B* **2015,** *119*, 2839-2843.

(161) Raitsimring, A. M.; Gunanathan, C.; Potapov, A.; Efremenko, I.; Martin, J. M.; Milstein, D.; Goldfarb, D. Gd3+ Complexes as Potential Spin Labels for High Field Pulsed EPR Distance Measurements. *J. Am. Chem. Soc.* **2007,** *129*, 14138-14139.

(162) Abdelkader, E. H.; Lee, M. D.; Feintuch, A.; Cohen, M. R.; Swarbrick, J. D.; Otting, G.; Graham, B.; Goldfarb, D. A New Gd3+ Spin Label for Gd3+–Gd3+ Distance Measurements in Proteins Produces Narrow Distance Distributions. *J. Phys. Chem. Lett.* **2015,** *6*, 5016-5021.

(163) Martorana, A.; Yang, Y.; Zhao, Y.; Q, L.; Goldfarb, D. Mn(II) Tags for Deer Distance Measurements in Proteins Via C-S Attachment. *Dalton Trans.* **2015,** *44*, 20812-20816.

(164) Lawless, M. J.; Sarver, J. L.; Saxena, S. Nucleotide-Independent Copper (II)-Based Distance Measurements in DNA by Pulsed ESR Spectroscopy. *Angewandte Chemie International Edition* **2017,** *56,* 2115-2117.

(165) Lovett, J. E.; Bowen, A. M.; Timmel, C. R.; Jones, M. W.; Dilworth, J. R.; Caprotti, D.; Bell, S. G.; Wong, L. L.; Harmer, J. Structural Information from Orientationally Selective Deer Spectroscopy. *Phys. Chem. Chem. Phys.* **2009,** *11,* 6840-6848.

(166) Abé, C.; Klose, D.; Dietrich, F.; Ziegler, W. H.; Polyhach, Y.; Jeschke, G.; Steinhoff, H.-J. Orientation Selective Deer Measurements on Vinculin Tail at X-Band Frequencies Reveal Spin Label Orientations. *Journal of Magnetic Resonance* **2012,** *216,* 53-61.

(167) Marko, A.; Prisner, T. F. An Algorithm to Analyze Peldor Data of Rigid Spin Label Pairs. *Physical Chemistry Chemical Physics* **2013,** *15,* 619-627.

(168) Marko, A.; Margraf, D.; Cekan, P.; Sigurdsson, S. T.; Schiemann, O.; Prisner, T. F. Analytical Method to Determine the Orientation of Rigid Spin Labels in DNA. *Physical Review E* **2010,** *81,* 021911.

(169) Schiemann, O.; Cekan, P.; Margraf, D.; Prisner, T. F.; Sigurdsson, S. T. Relative Orientation of Rigid Nitroxides by Peldor: Beyond Distance Measurements in Nucleic Acids. *Angewandte Chemie International Edition* **2009,** *48,* 3292-3295.

(170) Bode, B. E.; Plackmeyer, J.; Prisner, T. F.; Schiemann, O. Peldor Measurements on a Nitroxide-Labeled Cu(II) Porhyrin: Orientation Selection, Spin Density Distribution, and Conformational Flexibility. *J. Phys. Chem. A* **2008,** *112,* 5064-5073.

(171) Bode, B. E.; Plackmeyer, J.; Bolte, M.; Prisner, T. F.; Schiemann, O. Peldor on an Exchange Coupled Nitroxide Copper(II) Spin Pair. *Organo-Transition Metal Complexes* **2009,** *694,* 1172-1179.

(172) Mabbs, F. E.; Collison, D., *Electron Paramagnetic Resonance of D Transition Metal Compounds*. Elsevier: 2013; Vol. 16.

(173) Denysenkov, V. P.; Prisner, T. F.; Stubbe, J.; Bennati, M. High-Frequency 180 Ghz Peldor. *Applied Magnetic Resonance* **2005,** *29*, 375-384.

(174) Denysenkov, V. P.; Biglino, D.; Lubitz, W.; Prisner, T. F.; Bennati, M. Structure of the Tyrosyl Biradical in Mouse R2 Ribonucleotide Reductase from High-Field Peldor. *Angewandte Chemie International Edition* **2008,** *47*, 1224-1227.

(175) Denysenkov, V. P.; Prisner, T. F.; Stubbe, J.; Bennati, M. High-Field Pulsed Electron–Electron Double Resonance Spectroscopy to Determine the Orientation of the Tyrosyl Radicals in Ribonucleotide Reductase. *Proceedings of the National Academy of Sciences* **2006,** *103*, 13386-13390.

(176) Sicoli, G.; Argirević, T.; Stubbe, J.; Tkach, I.; Bennati, M. Effects in 94 ghz Orientation-Selected Peldor on a Rigid Pair of Radicals with Non-Collinear Axes. *Applied Magnetic Resonance* **2009,** *37*, 539.

(177) Kaminker, I.; Tkach, I.; Manukovsky, N.; Huber, T.; Yagi, H.; Otting, G.; Bennati, M.; Goldfarb, D. W-Band Orientation Selective Deer Measurements on a Gd3+/Nitroxide Mixed-Labeled Protein Dimer with a Dual Mode Cavity. *Journal of Magnetic Resonance* **2013,** *227*, 66-71.

(178) Giannoulis, A.; Motion, C. L.; Oranges, M.; Bühl, M.; Smith, G. M.; Bode, B. E. Orientation Selection in High-Field Ridme and Peldor Experiments Involving Low-Spin Coii Ions. *Physical Chemistry Chemical Physics* **2018,** *20*, 2151-2154.

(179) Tkach, I.; Pornsuwan, S.; Höbartner, C.; Wachowius, F.; Sigurdsson, S. T.; Baranova, T. Y.; Diederichsen, U.; Sicoli, G.; Bennati, M. Orientation Selection in Distance

Measurements between Nitroxide Spin Labels at 94 Ghz EPR with Variable Dual Frequency Irradiation. *Physical Chemistry Chemical Physics* **2013,** *15*, 3433-3437.

(180) Engelhard, D. M.; Meyer, A.; Berndhäuser, A.; Schiemann, O.; Clever, G. H. Di-Copper (II) DNA G-Quadruplexes as EPR Distance Rulers. *Chemical Communications* **2018,** *54*, 7455-7458.

(181) Stevens, M. A.; McKay, J. E.; Robinson, J. L. S.; El Mkami, H.; Smith, G. M.; Norman, D. G. The Use of the Rx Spin Label in Orientation Measurement on Proteins, by EPR. *Physical Chemistry Chemical Physics* **2016,** *18*, 5799-5806.

(182) Tait, C. E.; Stoll, S. Coherent Pump Pulses in Double Electron Electron Resonance Spectroscopy. *Physical Chemistry Chemical Physics* **2016,** *18*, 18470-18485.

(183) Larsen, R. G.; Singel, D. J. Double Electron-Electron Resonance Spin-Echo Modulation: Spectroscopic Measurement of Electron Spin Pair Separations in Orientationally Disordered Solids. *J. Chem. Phys.* **1993,** *98*, 5134-5146.

(184) Maryasov, A.; Tsvetkov, Y. D.; Raap, J. Weakly Coupled Radical Pairs in Solids: Eldor in Ese Structure Studies. *Applied Magnetic Resonance* **1998,** *14*, 101-113.

(185) Merz, G. E.; Borbat, P. P.; Pratt, A. J.; Getzoff, E. D.; Freed, J. H.; Crane, B. R. Copper-Based Pulsed Dipolar ESR Spectroscopy as a Probe of Protein Conformation Linked to Disease States. *Biophys. J.* **2014,** *107*, 1669-1674.

(186) Alexander, P.; Fahnestock, S.; Lee, T.; Orban, J.; Bryan, P. Thermodynamic Analysis of the Folding of the Streptococcal Protein G Igg-Binding Domains B1 and B2: Why Small Proteins Tend to Have High Denaturation Temperatures. *Biochemistry* **1992,** *31*, 3597-603.

(187) Dockter, C.; Volkov, A.; Bauer, C.; Polyhach, Y.; Joly-Lopez, Z.; Jeschke, G.; Paulsen, H. Refolding of the Integral Membrane Protein Light-Harvesting Complex II Monitored

by Pulse EPR. *Proceedings of the National Academy of Sciences of the United States of America* **2009,** *106*, 18485-18490.

(188) Walsh, J. D.; Meier, K.; Ishima, R.; Gronenborn, A. M. NMR Studies on Domain Diffusion and Alignment in Modular Gb1 Repeats. *Biophysical journal* **2010,** *99*, 2636-2646.

(189) Sengupta, I.; Nadaud, P. S.; Helmus, J. J.; Schwieters, C. D.; Jaroniec, C. P. Protein Fold Determined by Paramagnetic Magic-Angle Spinning Solid-State NMR Spectroscopy. *Nature chemistry* **2012,** *4*, 410.

(190) Nadaud, P. S.; Helmus, J. J.; Kall, S. L.; Jaroniec, C. P. Paramagnetic Ions Enable Tuning of Nuclear Relaxation Rates and Provide Long-Range Structural Restraints in Solid-State NMR of Proteins. *Journal of the American Chemical Society* **2009,** *131*, 8108-8120.

(191) Thoms, S.; Max, K. E. A.; Wunderlich, M.; Jacso, T.; Lilie, H.; Reif, B.; Heinemann, U.; Schmid, F. X. Dimer Formation of a Stabilized Gβ1 Variant: A Structural and Energetic Analysis. *Journal of molecular biology* **2009,** *391*, 918-932.

(192) Morrone, A.; Giri, R.; Toofanny, R. D.; Travaglini-Allocatelli, C.; Brunori, M.; Daggett, V.; Gianni, S. Gb1 Is Not a Two-State Folder: Identification and Characterization of an on-Pathway Intermediate. *Biophysical journal* **2011,** *101*, 2053-2060.

(193) Lindman, S.; Xue, W.-F.; Szczepankiewicz, O.; Bauer, M. C.; Nilsson, H.; Linse, S. Salting the Charged Surface: Ph and Salt Dependence of Protein G B1 Stability. *Biophysical journal* **2006,** *90*, 2911-2921.

(194) Munoz, V.; Thompson, P. A.; Hofrichter, J.; Eaton, W. A. Folding Dynamics and Mechanism of B-Hairpin Formation. *Nature* **1997,** *390*, 196.

(195) Bauer, M. C.; Xue, W.-F.; Linse, S. Protein Gb1 Folding and Assembly from Structural Elements. *International journal of molecular sciences* **2009,** *10*, 1552-1566.

(196) Chiang, Y.-W.; Borbat, P. P.; Freed, J. H. The Determination of Pair Distance Distributions by Pulsed ESR Using Tikhonov Regularization. *J. Magn. Reson.* **2005,** *172,* 279-295.

(197) Brandi-Blanco, M. P.; Dumet-Fernandes, B.; González-Pérez, J. M.; Choquesillo-Lazarte, D. A Redetermination of (N9-Adenine-Kn)-Aqua[Glycylglycinato(2-)-K3n,N',O]-Copper(II). *Acta. Cryst.* **2007,** *63*, m1598.

(198) Seeman, N. C. Nucleic Acid Nanostructures and Topology. *Angew. Chem., Int. Ed.* **1998,** *37*, 3220-3238.

(199) Goodman, R. P.; Heilemann, M.; Doose, S.; Erben, C. M.; Kapanidis, A. N.; Turberfield, A. J. Reconfigurable, Braced, Three-Dimensional DNA Nanostructures. *Nat. Nanotechnol.* **2008,** *3*, 93-96.

(200) Wilner, O. I.; Willner, I. Functionalized DNA Nanostructures. *Chem. Rev.* **2012,** *112*, 2528-2556.

(201) Seeman, N. C. From Genes to Machines: DNA Nanomechanical Devices. *Trends Biochem. Sci.* **2005,** *30*, 119-125.

(202) Bath, J.; Turberfield, A. J. DNA Nanomachines. *Nat. Nanotechnol.* **2007,** *2*, 275-284.

(203) Ramezani, H.; Dietz, H. Building Machines with DNA Molecules. *Nat. Rev. Genet.* **2020,** *21*, 5-26.

(204) Saidur, M. R.; Aziz, A. R. A.; Basirun, W. J. Recent Advances in DNA-Based Electrochemical Biosensors for Heavy Metal Ion Detection: A Review. *Biosens. Bioelectron.* **2017,** *90*, 125-139.

(205) Chao, J.; Zhu, D.; Zhang, Y.; Wang, L.; Fan, C. DNA Nanotechnology-Enabled Biosensors. *Biosens. Bioelectron.* **2016,** *76*, 68-79.

(206) Huang, R.; He, N.; Li, Z. Recent Progresses in DNA Nanostructure-Based Biosensors for Detection of Tumor Markers. *Biosens. Bioelectron.* **2018,** *109*, 27-34.

(207) de Vries, J. W.; Zhang, F.; Herrmann, A. Drug Delivery Systems Based on Nucleic Acid Nanostructures. *J. Control. Release* **2013,** *172*, 467-483.

(208) Linko, V.; Ora, A.; Kostiainen, M. A. DNA Nanostructures as Smart Drug-Delivery Vehicles and Molecular Devices. *Trends Biotechnol.* **2015,** *33*, 586-594.

(209) Hu, Q.; Li, H.; Wang, L.; Gu, H.; Fan, C. DNA Nanotechnology-Enabled Drug Delivery Systems. *Chem. Rev.* **2019,** *119*, 6459-6506.

(210) Lächelt, U.; Wagner, E. Nucleic Acid Therapeutics Using Polyplexes: A Journey of 50 Years (and Beyond). *Chem. Rev.* **2015,** *115*, 11043-11078.

(211) Sridharan, K.; Gogtay, N. J. Therapeutic Nucleic Acids: Current Clinical Status. *Br. J. Clin. Pharmacol.* **2016,** *82*, 659-672.

(212) Takemoto, K.; Inaki, Y. In *Synthetic Nucleic Acid Analogs Preparation and Interaction*, Berlin, Heidelberg, Springer Berlin Heidelberg: Berlin, Heidelberg, 1981; pp 1-51.

(213) Benner, S. A.; Karalkar, N. B.; Hoshika, S.; Laos, R.; Shaw, R. W.; Matsuura, M.; Fajardo, D.; Moussatche, P. Alternative Watson–Crick Synthetic Genetic Systems. *CSH. Perspect. Biol.* **2016,** *8*, a023770.

(214) Egholm, M.; Buchardt, O.; Nielsen, P. E.; Berg, R. H. Peptide Nucleic Acids (PNA). Oligonucleotide Analogs with an Achiral Peptide Backbone. *J. Am. Chem. Soc.* **1992,** *114*, 1895-1897.

(215) Nielsen, P. E.; Egholm, M. An Introduction to Peptide Nucleic Acid. *Curr. Issues. Mol. Biol.* **1999,** *1*, 89-104.

(216) Egholm, M.; Buchardt, O.; Christensen, L.; Behrens, C.; Freier, S. M.; Driver, D. A.; Berg, R. H.; Kim, S. K.; Norden, B.; Nielsen, P. E. PNA Hybridizes to Complementary Oligonucleotides Obeying the Watson–Crick Hydrogen-Bonding Rules. *Nature* **1993,** *365*, 566-568.

(217) Demidov, V. V.; Potaman, V. N.; Frank-Kamenetskil, M. D.; Egholm, M.; Buchard, O.; Sönnichsen, S. H.; Nlelsen, P. E. Stability of Peptide Nucleic Acids in Human Serum and Cellular Extracts. *Biochem. Pharmacol.* **1994,** *48*, 1310-1313.

(218) De Mesmaeker, A.; Altmann, K.-H.; Waldner, A.; Wendeborn, S. Backbone Modifications in Oligonucleotides and Peptide Nucleic Acid Systems. *Curr. Opin. Struct. Biol.* **1995,** *5*, 343-355.

(219) Nielsen, P. E. Applications of Peptide Nucleic Acids. *Curr. Opin. Biotechnol.* **1999,** *10*, 71-75.

(220) Saarbach, J.; Sabale, P. M.; Winssinger, N. Peptide Nucleic Acid (PNA) and Its Applications in Chemical Biology, Diagnostics, and Therapeutics. *Curr. Opin. Chem. Biol.* **2019,** *52*, 112-124.

(221) Gourishankar, A.; Shukla, S.; Pasricha, R.; Sastry, M.; Ganesh, K. N. DNA and PNA as Templates for Building Nanoassemblies Via Electrostatic Complexation with Gold Nanoparticles. *Curr. Appl. Phys.* **2005,** *5*, 102-107.

(222) Beall, E.; Ulku, S.; Liu, C.; Wierzbinski, E.; Zhang, Y.; Bae, Y.; Zhang, P.; Achim, C.; Beratan, D. N.; Waldeck, D. H. Effects of the Backbone and Chemical Linker on the Molecular Conductance of Nucleic Acid Duplexes. *J. Am. Chem. Soc.* **2017,** *139*, 6726-6735.

(223) Feldkamp, U.; Niemeyer, C. M. Rational Design of DNA Nanoarchitectures. *Angew. Chem., Int. Ed.* **2006,** *45*, 1856-1876.

(224) Paul, A.; Bezer, S.; Venkatramani, R.; Kocsis, L.; Wierzbinski, E.; Balaeff, A.; Keinan, S.; Beratan, D. N.; Achim, C.; Waldeck, D. H. Role of Nucleobase Energetics and Nucleobase Interactions in Single-Stranded Peptide Nucleic Acid Charge Transfer. *J. Am. Chem. Soc.* **2009,** *131*, 6498-6507.

(225) Paul, A.; Watson, R. M.; Wierzbinski, E.; Davis, K. L.; Sha, A.; Achim, C.; Waldeck, D. H. Distance Dependence of the Charge Transfer Rate for Peptide Nucleic Acid Monolayers. *J. Phys. Chem. B* **2010,** *114*, 14140-14148.

(226) Wierzbinski, E.; de Leon, A.; Yin, X.; Balaeff, A.; Davis, K. L.; Reppireddy, S.; Venkatramani, R.; Keinan, S.; Ly, D. H.; Madrid, M., et al. Effect of Backbone Flexibility on Charge Transfer Rates in Peptide Nucleic Acid Duplexes. *J. Am. Chem. Soc.* **2012,** *134*, 9335-9342.

(227) Eriksson, M.; Nielsen, P. E. Solution Structure of a Peptide Nucleic Acid–DNA Duplex. *Nat. Struct. Biol.* **1996,** *3*, 410-413.

(228) Yeh, J. I.; Pohl, E.; Truan, D.; He, W.; Sheldrick, G. M.; Du, S.; Achim, C. The Crystal Structure of Non-Modified and Bipyridine-Modified PNA Duplexes. *Chem.--Eur. J.* **2010,** *16*, 11867-11875.

(229) He, W.; Hatcher, E.; Balaeff, A.; Beratan, D. N.; Gil, R. R.; Madrid, M.; Achim, C. Solution Structure of a Peptide Nucleic Acid Duplex from NMR Data: Features and Limitations. *J. Am. Chem. Soc.* **2008,** *130*, 13264-13273.

(230) Roessler, M. M.; Salvadori, E. Principles and Applications of EPR Spectroscopy in the Chemical Sciences. *Chem. Soc. Rev.* **2018,** *47*, 2534-2553.

(231) Jeschke, G. The Contribution of Modern EPR to Structural Biology. *Emerg. Top. Life Sci.* **2018,** *2*, 9-18.

(232) Hubbell, W. L.; Altenbach, C. Investigation of Structure and Dynamics in Membrane Proteins Using Site-Directed Spin Labeling. *Cur. Opin. Struct. Biol.* **1994,** *4*, 566-573.

(233) Fanucci, G. E.; Cafiso, D. S. Recent Advances and Applications of Site-Directed Spin Labeling. *Curr. Opin. Struct. Biol.* **2006,** *16*, 644-653.

(234) Merz, G. E.; Borbat, P. P.; Muok, A. R.; Srivastava, M.; Bunck, D. N.; Freed, J. H.; Crane, B. R. Site-Specific Incorporation of a Cu2+ Spin Label into Proteins for Measuring Distances by Pulsed Dipolar Electron Spin Resonance Spectroscopy. *J. Phys. Chem. B* **2018,** *122*, 9443-9451.

(235) Sarver, J.; Silva, K. I.; Saxena, S. Measuring Cu2+-Nitroxide Distances Using Double Electron–Electron Resonance and Saturation Recovery. *Appl. Magn. Reson.* **2013,** *44*, 583-594.

(236) Prokopiou, G.; Lee, M. D.; Collauto, A.; Abdelkader, E. H.; Bahrenberg, T.; Feintuch, A.; Ramirez-Cohen, M.; Clayton, J.; Swarbrick, J. D.; Graham, B., et al. Small Gd(III) Tags for Gd(III)–Gd(III) Distance Measurements in Proteins by EPR Spectroscopy. *Inorg. Chem.* **2018,** *57*, 5048-5059.

(237) Abdullin, D.; Schiemann, O. Pulsed Dipolar EPR Spectroscopy and Metal Ions: Methodology and Biological Applications. *ChemPlusChem* **2020,** *85*, 353-372.

(238) Ghosh, S.; Lawless, M. J.; Brubaker, H. J.; Singewald, K.; Kurpiewski, M. R.; Jen-Jacobson, L.; Saxena, S. Cu2+-Based Distance Measurements by Pulsed EPR Provide Distance Constraints for DNA Backbone Conformations in Solution. *Nucleic Acids Res.* **2020**.

(239) Li, X.; Cheng, Y.; Zhang, L.; Zhang, L. Synthesis of Spin Labeled Conjugate of Peptide and Peptide Nucleic Acid. *Synth. Commun.* **1999,** *29*, 1519-1525.

(240) Cerasi, A.; Millo, E.; Ottaviani, M. F.; Damonte, G.; Cangiotti, M.; Benatti, U.; Chiarantini, L. New Synthesis of a Spin-Labeled Peptide Nucleic Acid and Its Interactions with Nucleic Acids. *Tetrahedron Lett.* **2003,** *44*, 8701-8704.

(241) Li, X.; Huang, C.; Wang, Y.; Chen, Y.; Zhang, L.; Lu, J.; Zhang, L. Studies on Spin-Labelled Peptide Nucleic Acid. *Curr. Sci.* **1998,** *74*, 624-626.

(242) Marinelli, F.; Faraldo-Gómez, José D. Ensemble-Biased Metadynamics: A Molecular Simulation Method to Sample Experimental Distributions. *Biophys. J.* **2015,** *108*, 2779-2782.

(243) Marinelli, F.; Fiorin, G. Structural Characterization of Biomolecules through Atomistic Simulations Guided by Deer Measurements. *Structure* **2019,** *27*, 359-370.e12.

(244) Shen, R.; Han, W.; Fiorin, G.; Islam, S. M.; Schulten, K.; Roux, B. Structural Refinement of Proteins by Restrained Molecular Dynamics Simulations with Non-Interacting Molecular Fragments. *PLoS Comput. Biol.* **2015,** *11*, e1004368.

(245) Ding, F.; Layten, M.; Simmerling, C. Solution Structure of Hiv-1 Protease Flaps Probed by Comparison of Molecular Dynamics Simulation Ensembles and EPR Experiments. *J. Am. Chem. Soc.* **2008,** *130*, 7184-7185.

(246) Sen, S.; Nilsson, L. Molecular Dynamics of Duplex Systems Involving PNA: Structural and Dynamical Consequences of the Nucleic Acid Backbone. *J. Am. Chem. Soc.* **1998,** *120*, 619-631.

(247) Weroński, P.; Jiang, Y.; Rasmussen, S. Molecular Dynamics Study of Small PNA Molecules in Lipid-Water System. *Biophys. J.* **2007,** *92*, 3081-3091.

(248) Autiero, I.; Saviano, M.; Langella, E. Molecular Dynamics Simulations of PNA–PNA and PNA–DNA Duplexes by the Use of New Parameters Implemented in the Gromacs Package: A Conformational and Dynamics Study. *Phys. Chem. Chem. Phys.* **2014,** *16*, 1868-1874.

(249) Soliva, R.; Sherer, E.; Luque, F. J.; Laughton, C. A.; Orozco, M. Molecular Dynamics Simulations of PNA·DNA and PNA·Rna Duplexes in Aqueous Solution. *J. Am. Chem. Soc.* **2000,** *122*, 5997-6008.

(250) Jasiński, M.; Feig, M.; Trylska, J. Improved Force Fields for Peptide Nucleic Acids with Optimized Backbone Torsion Parameters. *J. Chem. Theory Comput.* **2018,** *14*, 3603-3620.

(251) Frisch, M. J.; Trucks, G. W.; Schlegel, H. B.; Scuseria, G. E.; Robb, M. A.; Cheeseman, J. R.; Scalmani, G.; Barone, V.; Petersson, G. A.; Nakatsuji, H., et al. Gaussian 16, Revision C.01. *Gaussian, Inc., Wallingford CT* **2016**.

(252) Bayly, C. I.; Cieplak, P.; Cornell, W. D.; Kollman, P. A. A Well-Behaved Electrostatic Potential Based Method Using Charge Restraints for Deriving Atomic Charges- the Resp Model. *J. Phys. Chem.* **1993,** *97*, 10269-10280.

(253) Wang, J.; Wang, W.; Kollman, P. A.; Case, D. A. Automatic Atom Type and Bond Type Perception in Molecular Mechanical Calculations. *J. Mol. Graph. Model.* **2006,** *25*, 247-260.

(254) Case, D. A.; Ben-Shalom, I. Y.; Brozell, S. R.; Cerutti, D. S.; Cheatham, I., T.E. ; Cruzeiro, V. W. D.; Darden, T. A.; Duke, R. E.; Ghoreishi, D.; Gilson, M. K., et al. Amber 2018. *University of California, San Francisco* **2018**.

(255) Wang, J.; Wolf, R. M.; Caldwell, J. W.; Kollman, P. A.; Case, D. A. Development and Testing of a General Amber Force Field. *J. Comput. Chem.* **2004,** *25*, 1157-1174.

(256) Case, D.; Betz, R.; Botello-Smith, W.; Cerutti, D.; Darden, T. Amber 2016. 2016. *University of California, San Fransico* **2016**.

(257) Jorgensen, W. L.; Chandrasekhar, J.; Madura, J. D.; Impey, R. W.; Klein, M. L. Comparison of Simple Potential Functions for Simulating Liquid Water. *J. Chem. Phys.* **1983,** *79*, 926-935.

(258) Humphrey, W.; Dalke, A.; Schulten, K. Vmd: Visual Molecular Dynamics. *J. Mol. Graph.* **1996,** *14*, 33-38.

(259) Christensen, L.; Fitzpatrick, R.; Gildea, B.; Petersen, K. H.; Hansen, H. F.; Koch, T.; Egholm, M.; Buchardt, O.; Nielsen, P. E.; Coull, J., et al. Solid-Phase Synthesis of Peptide Nucleic Acids. *J. Pept. Sci.* **1995,** *1*, 175-183.

(260) Watson, R. M.; Skorik, Y. A.; Patra, G. K.; Achim, C. Influence of Metal Coordination on the Mismatch Tolerance of Ligand-Modified PNA Duplexes. *J. Am. Chem. Soc.* **2005,** *127*, 14628-14639.

(261) Nielsen, P. E.; Egholm, M., *Peptide Nucleic Acids*. Springer: 1999.

(262) He, W.; Crawford, M. J.; Rapireddy, S.; Madrid, M.; Gil, R. R.; Ly, D. H.; Achim, C. The Structure of a Γ-Modified Peptide Nucleic Acid Duplex. *Mol. Biosyst.* **2010,** *6*, 1619-1629.

(263) Dragulescu-Andrasi, A.; Rapireddy, S.; Frezza, B. M.; Gayathri, C.; Gil, R. R.; Ly, D. H. A Simple Γ-Backbone Modification Preorganizes Peptide Nucleic Acid into a Helical Structure. *J. Am. Chem. Soc.* **2006,** *128*, 10258-10267.

(264) Wittung, P.; Eriksson, M.; Lyng, R.; Nielsen, P. E.; Norden, B. Induced Chirality in PNA-PNA Duplexes. *J. Am. Chem. Soc.* **1995,** *117*, 10167-10173.

(265) Franzini, R. M.; Watson, R. M.; Patra, G. K.; Breece, R. M.; Tierney, D. L.; Hendrich, M. P.; Achim, C. Metal Binding to Bipyridine-Modified PNA. *Inorg. Chem.* **2006,** *45*, 9798-9811.

(266) Fumikazu, K.; Kazuhide, O.; Isamu, N. The Crystal Structures of Metal 8-Hydroxyquinolinate. I. Copper 8-Hydroxyquinolinate. *Bull. Chem. Soc. Jpn.* **1963,** *36*, 422-427.

(267) Etaiw, S. E.-d. H.; El-bendary, M. M. Crystal Structure, Characterization and Catalytic Activities of Cu(II) Coordination Complexes with 8-Hydroxyquinoline and Pyrazine-2-Carboxylic Acid. *Appl. Organomet. Chem.* **2018,** *32*, e4213.

(268) Marko, A.; Denysenkov, V.; Margraf, D.; Cekan, P.; Schiemann, O.; Sigurdsson, S. T.; Prisner, T. F. Conformational Flexibility of DNA. *J. Am. Chem. Soc.* **2011,** *133*, 13375-13379.

(269) Li, S.; Olson, W. K.; Lu, X.-J. Web 3dna 2.0 for the Analysis, Visualization, and Modeling of 3D Nucleic Acid Structures. *Nucleic Acids Res.* **2019,** *47*, W26-W34.

(270) Dickerson, R. E. Definitions and Nomenclature of Nucleic Acid Structure Parameters. *J. Biomol. Struct. Dyn.* **1989,** *6*, 627-634.